High-Energy Sub-Cycle Optical Waveform Synthesizer

by

Shu-Wei Huang

B.S., Electrical Engineering, National Taiwan University, 2004
M.S., Electrical Engineering, Massachusetts Institute of Technology, 2007
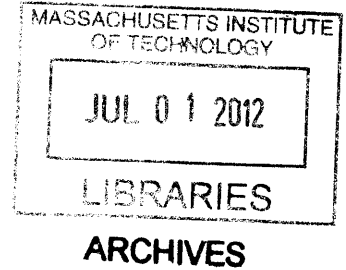
Submitted to the Department of Electrical Engineering and Computer Science
in partial fulfillment of the requirements for the degree of

Doctor of Philosophy in Electrical Engineering

at the

MASSACHUSETTS INSTITUTE OF TECHNOLOGY

June 2012

Author...
Department of Electrical Engineering and Computer Science
June 1st, 2012

Certified by...
Franz X. Kärtner
Professor of Electrical Engineering
Thesis Supervisor

Accepted by...
Leslie A. Kolodziejski
Professor of Electrical Engineering
Chairman, Department Committee on Graduate Theses

THIS PAGE IS INTENTIONALLY LEFT BLANK

High-Energy Sub-Cycle Optical Waveform Synthesizer

by

Shu-Wei Huang

Submitted to the Department of Electrical Engineering and Computer Science
on June 1st, 2012,
in partial fulfillment of the requirements for the degree of
Doctor of Philosophy in Electrical Engineering and Computer Science

Abstract

Over the last decade, the control of atomic-scale electronic motion by optical fields strong enough to mitigate the atomic Coulomb potential, has broken tremendous new ground with the advent of phase controlled high-energy few-cycle pulse sources. In particular, broadband optical parametric chirped pulse amplifier (OPCPA) has been investigated intensively in recent years to enable studies of novel strong-field physics phenomena such as high-harmonic generation (HHG) and strong-field ionization. Further investigation and control of these physical processes ask for the capability of waveform shaping on sub-cycle time scales, which requires a fully phase-controlled multiple-octave-spanning spectrum.

To date, no single laser source can support a bandwidth of more than an octave. Coherent synthesis of pulses with different spectra, or wavelength multiplexing, presents a route towards obtaining a multi-octave spanning laser spectrum. The benefit of this approach lies in its modular design and scalability in both bandwidth and pulse energy. However, it was only recently laser scientists were able to successfully demonstrate coherent synthesis of two lasers albeit at low energy and high repetition rate. Achieving high pulse energy requires synthesis of low repetition rate pulses, which is a challenge because of the environmental perturbations typifying high-energy amplifiers.

The technological advancements towards the ideal source for study and control of such strong-field physics are the focus of this thesis. The background reviews on femtosecond Ti:sapphire oscillators, carrier-envelope phase stabilization, chirped pulse amplifier, broadband OPCPAs, and HHG are given in Chapter 1. Chapter 2 starts with a discussion on the various properties of OPCPA which lends itself to the ideal building module for high-energy pulse synthesis. Then it is followed by a comprehensive optimization study and experimental results of broadband OPCPAs at different spectral ranges. In chapter 3, the first high-energy sub-cycle waveform synthesizer is presented. It is the prototype of a class of novel optical tools for atto-second control of strong-field physics experiments. Novel technologies that enable such a waveform synthesizer are described in details. At the end of the chapter, work towards the construction of a large-scale waveform synthesizer is included. Finally, the thesis is concluded by introducing some possible future directions.

Thesis Supervisor: Franz X. Kärtner

Title: Professor of Electrical Engineering and Computer Science

Acknowledgements

要感謝的人太多了，那就謝天吧

TABLE OF CONTENTS

Chapter 1

Introduction

Since the invention of mode-locked lasers, the ultrafast laser science community has seen tremendous progress towards broader optical bandwidths, shorter pulse durations and better phase control. Broader bandwidth in coherent and phase-controlled sources has also led to breakthroughs in biomedical imaging [1] and astrophysical spectrography [2]. Shorter pulse durations then have enabled ultrafast pump-probe experiments to reveal the electronic and molecular dynamics critical to the understanding of condensed matter [3], chemical [4] and biological [5] processes. Better phase control and frequency comb techniques have revolutionized optical frequency metrology, optical atomic clocks, and high-precision spectroscopy [6], [7]. Meanwhile, the study of high-field physics such as laser plasma interaction has demanded optical pulses of ever higher pulse energies and peak powers [8]. Chirped pulse amplifiers (CPAs) have been developed and intensively employed nowadays as the basic enabling technology for the study of high-field physics [9].

In recent years, the investigation of phenomena at the intersection of ultrafast and high-field laser physics, such as high-harmonic generation (HHG) [10] and strong-field ionization [11], has demanded that laser sources combine each of the improvements mentioned above. The development of close-to-single-cycle, carrier-envelope phase (CEP) controlled high-energy optical pulses has already led to the generation of isolated attosecond pulses in the EUV range [12], expanding

ultrafast spectroscopy to attosecond resolution [13], [14]. However, further investigation and control of these strong-field physical processes demand even more from laser technology, simultaneously requiring multi-octave-spanning bandwidth, peak-intensities above 10^{14} W/cm^2, sub-cycle pulse duration, and full phase control. Such features would allow arbitrary shaping of the strong electric-field waveforms for steering ionized electron wavepackets [15] and precise control of tunneling and multiphoton ionization events.

The technological advancements towards an ideal source for study of such strong-field physics are the focus of this thesis. The thesis is organized as follows: In the remaining chapter, the essential background reviews on Femto-second Ti:sapphire oscillators, CEP stabilization, chirped pulse amplifier, broadband optical parametric chirped pulse amplifiers (OPCPAs), and HHG will be given. In chapter 2, theory, optimization, and experimental results of broadband OPCPAs at different spectral ranges are presented. In chapter 3, waveform synthesis based on coherent wavelength multiplexing is presented. Work which might benefit the construction of a large-scale waveform synthesis is also described. Finally, the thesis is concluded by discussing some possible future directions.

1.1   Femtosecond Ti:sapphire oscillator

Today, the Ti:sapphire crystal is undoubtedly the most important laser gain medium for the ultrafast laser science community. It has a gain bandwidth, if fully utilized, that supports sub-two-cycle (5fs) pulses. Its excellent mechanical and optical stability make routine operation possible. To exploit its potential, Kerr-lens
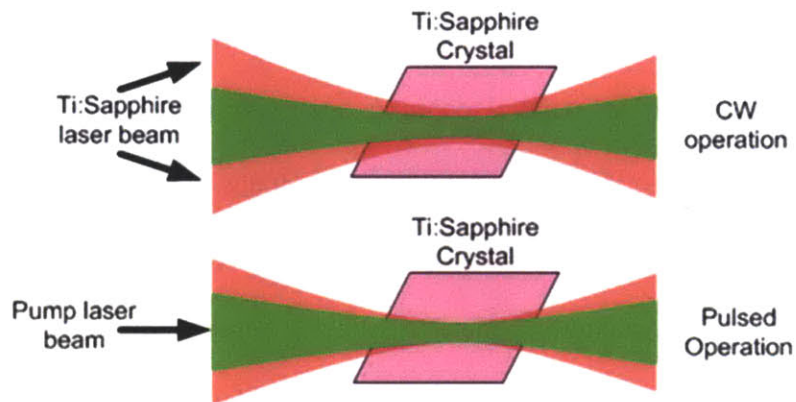
Figure 1.1 Principle of KLM. Courtesy of Li-Jin Chen.

mode-locking (KLM) [16], [17] and double chirped mirror (DCM) [18] technologies have been developed.

Mode-locking refers to phase stable multi-mode operation of a laser rather than one mode continuous-wave (CW) lasing. In the frequency domain, mode-locking helps overcome the mode competition due to non-uniform gain and establish the phase coherence between different longitudinal modes. Figure 1.1 depicts the principle of KLM. Due to the optical Kerr effect, a pulse that builds up in a laser cavity experiences an intensity-dependent self-focusing. If the pump is matched to the mode size of the peak of the pulse, the CW laser beam will have a bad pump overlap, *i.e.* low gain, and thus the laser cavity is in favor of pulsed operation. The pulse will keep shortening itself until other pulse lengthening effects such as gain-filtering and dispersion come into play and balance the pulse duration. KLM is a unique mode-locking technique because its response is almost instantaneous and hence it sets no lower bound to the achievable pulse duration.

Precise control of intracavity dispersion is another key to short pulse generation. DCM, a dielectric mirror technology, offers precise dispersion engineering over an octave-spanning spectrum with negligible loss. A chirped mirror, ancestor of DCM, is composed of Bragg stacks (alternating high and low index quarter wavelength thick layers) with the Bragg wavelength being chirped so that different wavelengths penetrate different depths into the mirror upon reflection giving rise to a wavelength dependent group delay. DCM mitigates the impedance mismatch problem encountered in a chirped mirror by adding a broadband AR-coating and adiabatically switching on the Bragg stacks. The performance degradation due to the imperfect AR-coating and Bragg stacks can be further minimized by using DCMs in pairs with one of the them having an additional quarter wavelength thick layer between the AR-coating and the Bragg stacks. Figure 1.2 shows the typical performance of a DCM pair that can support octave-spanning operation of the Ti:sapphire lasers.
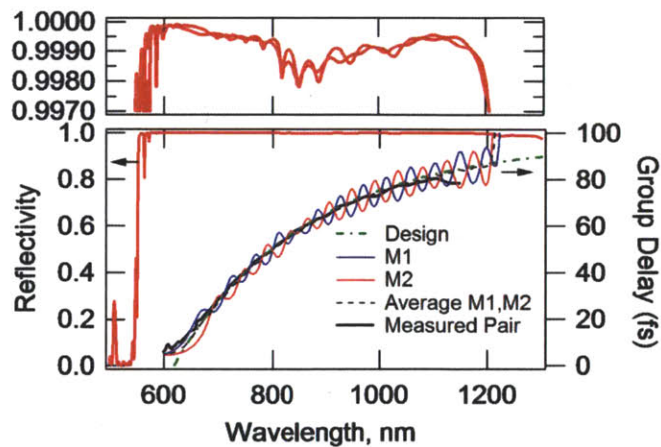
Figure 1.2 Reflectivity and group delay for a typical DCM pair used in the octave-spanning Ti:Sapphire laser.

4

1.2 Carrier-envelope phase stabilization

For field-sensitive applications such as strong-field physics, CEP control becomes mandatory so as to make sure not only the pulse shape but also the electric field repeats itself from pulse to pulse. Intuitively one would build a linear interferometer that interfere a pulse with its adjacent pulse to measure the CEP slip. Using the output from this interferometer as the error signal of a feedback loop, one can then stabilize the CEP. Alternatively, one can build a nonlinear interferometer, so called *1f-2f* interferometer, to directly detect the CEP (plus some constant) of the pulse. Figure 1.3 depicts the principle of a *1f-2f* interferometer. One first creates two replicas of each pulse by a beamsplitter. One of the replicas undergoes second-harmonic generation and the output carries the phase information of twice the originial CEP. Due to the octave-spanning spectrum, one can interfere this output with the other replica, which carries the phase information of the original CEP, and the interferometer output is a measurement of the CEP (plus some constant). Similarly, one can stabilize the CEP by feeding the output from this nonlinear interferometer as the error signal to a feedback loop. Apparently, a nonlinear interferometer has the advantage that one can avoid the meter-level long delay line, which introduces excess noise to the measurement. Furthermore, a nonlinear interferometer directly measures the CEP (plus some constant), rather than the CEP slip, and thus a feedback steady-state error will only result in a CEP offset, but the CEP will remain stabilized. In contrast, the feedback steady-state error will result in CEP oscillation if a linear interferometer is employed.
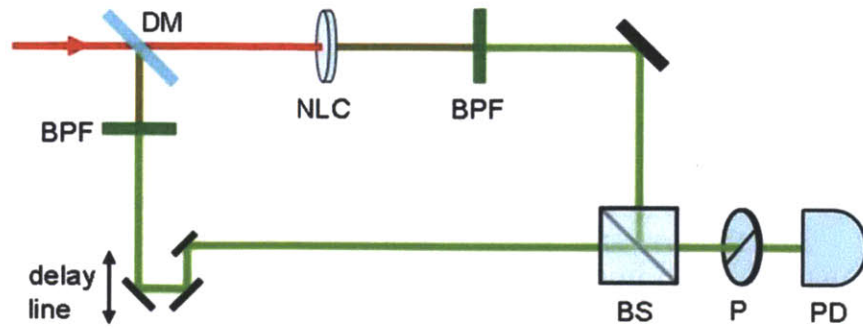
Figure 1.3 The optical setup of a standard Mach-Zehnder type *f-2f* self-referencing nonlinear interferometer. DM: dichroic mirror; BPF: bandpass filter; NLC: nonlinear crystal; BS: beamsplitter; P: polarizer; PD: photodetector.

1.3   Chirped pulse amplifier

As mentioned previously, CPAs have been developed and are intensively employed nowadays as the basic enabling technology for the study of high-field physics. In a CPA, the pulse is stretched by many orders of magnitude before being amplified in the gain medium. After the amplification, the pulse can be compressed back to its transform-limited duration. Due to the lower peak intensity, self-phase modulation (SPM) and self-focusing (SF) effects that the pulse experiences in the gain medium are reduced. SPM can broaden the pulse bandwidth, but too much SPM will limit the pulse compressibility and creates satellite pulses which are detrimental for most of the high-field physics experiments. While whole-beam SF can be estimated *a priori* and compensated by additional lenses, the small-scale SF is detrimental because it creates hot spots which can damage the gain medium and the optics. Artificial defects and aberration are hard to avoid in a high-power optical amplifier and they distort the beam. The optical Kerr effect amplifies the

6

distortion and leads to small-scale SF. Due to the space-time duality, one may think that the small scale effect will also happen in the time domain. However, there are at least two reasons that make the small scale effect in the time domain less problematic. First, the dispersion counteracts the SPM for most of the material in the spectral range from visible to near-IR and thus the distortion gets smoothed instead of amplified. Second, nothing in a typical CPA can modulate the light so fast (<1ps) that it leads to a severe small scale effect.

Figure 1.4 shows the schematics of a stretcher and a compressor typically employed in a CPA. A compressor is nothing more than a grating pair which introduces negative group-delay dispersion (GDD). A stretcher is composed of a grating pair and a telescope with two identical lenses separated by $2f$. When the distance between the lens and the grating, i.e. d, is also set to f, the telescope images the first grating to the second grating and thus the setup introduces no net dispersion. Similarly, when d is smaller than f, the effective grating separation is negative and thus a sign flipping of the dispersion (to all orders) in a grating pair is accomplished. In theory, these setups are the ideal stretching and compression system for a CPA [19].

(a) d f f d (b)
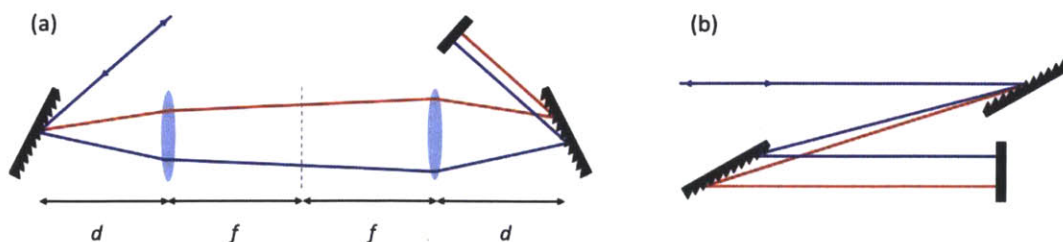
Figure 1.4 The optical setup of a typical stretcher (a) and compressor (b) in a CPA.

1.4   Broadband Optical parametric chirped pulse amplifier

Optical parametric chirped pulse amplification (OPCPA) is nowadays the most promising technology for producing the world's highest peak power, few-cycle light pulse sources in the visible and near-to-mid infrared range. In an OPCPA, a quasi-monochromatic high-energy pump field (such as, for example, a picosecond or nanosecond pulse) is coupled to a chirped, low-energy broadband seed field in a nonlinear crystal. If the seed pulse is sufficiently stretched, good energy extraction from the pump field can be achieved, and subsequent recompression makes it possible to reach very high peak powers. The OPCPA concept has some very important advantages with respect to the standard CPA: (i) the center wavelength is tunable as long as the conservations of photon energy and momentum are satisfied; (ii) the parametric amplification process can support gain bandwidths well in excess of those achievable with conventional linear amplifiers, allowing the generation of few-optical-cycle light pulses; (iii) the OPCPA has the capability of providing a high gain in a relatively short path length, minimizing the B-integral and allowing a compact, tabletop amplifier setup; (iv) amplification occurs only when there is a pump pulse, so that the amplified spontaneous emission and the consequent pre-pulse pedestal are greatly reduced; (v) thermal loading effects, apart from parasitic absorption, are completely absent, greatly reducing spatial aberration of the beams. These attributes allow OPCPA to push the limits of high peak power pulse generation at wavelengths at which broadband laser amplification has not been developed, a capability with increasing importance since the advent of Yb and Nd- based picosecond pump lasers that can deliver hundred-

8
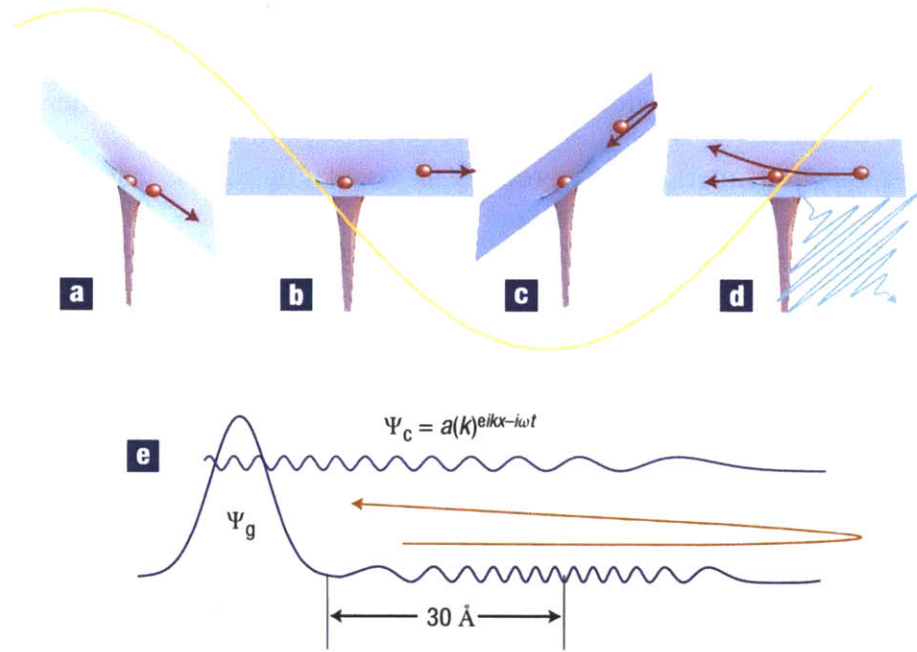
Figure 1.5 Semi-classical three-step model of HHG (picture taken from [21]).

watt average powers, thus promising simultaneous high peak power and high average power from OPCPA. As a result, today there is much interest in the development of OPCPA as a light source for few-cycle, high-intensity, near-to-mid-infrared pulse-driven applications such as high harmonic generation (HHG).

1.5   High harmonic generation

HHG is a technique for producing coherent EUV light and so far the only experimentally proven method for generating atto-second pulses. The process can be described by a semi-classical three-step model (Figure 1.5) **[20], [21]**. HHG occurs when an intense femto-second laser pulse is tightly focused into a gas or solid such that the peak electric-field amplitude is comparable to the atomic potential. Under this condition, an electron can be detached from its parent atom by

tunnel ionization. Then the free electron is accelerated in the electric field and gains kinetic energy from the electric field. Finally when the free electron is driven back to the vicinity of its parent atom, the free and the bound components of the total wave-function interfere and produce an oscillating dipole that emits EUV light. During this recombination process, the kinetic energy, amplitude and phase of the free electron wave-packet is transferred to the EUV light. Therefore, it is of great importance to control the electric-field waveform of the driving pulse because it directly influences the kinetic energy, amplitude and phase of the returning free electron wave-packet.

Using the three-step model, one can estimate the maximum possible photon energy by [20]:

$$E_{cutoff} = I_p + 3.2U_p, where\ U_p = E^2/4\omega_L^2 \sim I_L\lambda_L^2$$

U_p is the ponderomotive energy of the electron in an electric field of amplitude E and frequency ω_L , expressed in atomic units. The ponderomotive energy contribution to the EUV-photon energy increases proportionally to the laser intensity, I_L, and to the square of the drive laser wavelength, λ_L. The laser intensity cannot be increased arbitrarily; when too high the gas becomes fully ionized, causing HHG efficiency to vanish. In addition, increased plasma density causes a phase mismatch, also reducing HHG efficiency. At a drive wavelength of 800 nm the contribution to the emitted EUV photon energy due to the kinetic energy picked up in the laser field, $3.2U_p$, is at maximum 18 eV for Xe and 25 eV for Ar. At the intensities necessary to obtain higher photon energies, the electric field becomes so strong that it leads to complete ionization of these atoms, leading to an exponential

drop in HHG efficiency. For this reason it is necessary to use longer wavelength lasers to drive the HHG process. However, it is important to make the drive wavelength λ_L not much longer than necessary, because the efficiency per harmonic drops with $\lambda_L{}^5$ due to the quantum diffusion. Thus, beside the electric-field waveform, the wavelength of the driving laser is also an important parameter to be optimized.

THIS PAGE IS INTENTIONALLY LEFT BLANK

Chapter 2

Broadband Optical Parametric Chirped Pulse Amplifier

Optical parametric chirped pulse amplification (OPCPA) has become valuable not only as a means to push the limits of high peak power pulse generation at wavelengths at which laser amplification has not been developed, but as the only demonstrated technology for producing few-cycle pulses beyond the terawatt peak-power level. Since OPCPA is a nonlinear parametric process, its performance is highly flexible and dependent on the design parameters. Compared to chirped pulse laser amplification, OPCPA in general has the advantages of wavelength tunability, broadband gain bandwidth, high single-pass gain, less accumulation of nonlinear effects, high pulse contrast, and negligible thermal load.

The chapter starts with a general mathematical description of broadband OPCPA, followed by a study on temporal optimization of an OPCPA [22]. The study on temporal optimization is a collaborative work between MIT and Politecnico di Milano. The analytic analysis and the experiment are performed at MIT, led by Dr. Jeffrey Moses, while the numerical simulation is done at Politecnico di Milano, led by Cristian Manzoni. Then a detailed description of two μJ OPCPAs, which are the building blocks of our current high-energy waveform synthesizer, are given in Section 2.3 [23], [24]. Work on upgrading the SWIR-OPCPA by a cryogenically cooled Yb:YAG CPA, led by Dr. Kyung-Han Hong,

and demonstration of long-wavelength driven HHG with it are summarized in Sections 2.4 and 2.5 [25]. At the end, the analytic analysis on OPCPA is expanded and the investigation on how the performance can be improved by pump shaping is provided [26].

2.1 Mathematical description of broadband OPCPA

Under the slowly varying envelope approximation, the broadband OPA process can be well described by the following three coupled equations, where the second and third terms on the right hand side are the self-phase modulation (SPM) and the cross-phase modulation (XPM), respectively [27]:

$$\frac{\partial A_p}{\partial z} + \frac{1}{V_{gp}}\frac{\partial A_p}{\partial t} + jD_pA_p = -j\frac{\omega_p d_{eff}}{n_p c_0}A_sA_ie^{j\Delta kz} - j\frac{\omega_p \varepsilon_0 n_p n_2}{2}\left|A_p\right|^2 A_p$$

$$-j\gamma\frac{\omega_p \varepsilon_0 n_p n_2}{2}(|A_s|^2 + |A_i|^2)A_p \qquad Eq.\,2.1(A)$$

$$\frac{\partial A_s}{\partial z} + \frac{1}{V_{gs}}\frac{\partial A_s}{\partial t} + jD_sA_s = -j\frac{\omega_s d_{eff}}{n_s c_0}A_pA_i^*e^{-j\Delta kz} - j\frac{\omega_s \varepsilon_0 n_s n_2}{2}|A_s|^2 A_s$$

$$-j\gamma\frac{\omega_s \varepsilon_0 n_s n_2}{2}\left(\left|A_p\right|^2 + |A_i|^2\right) A_s \qquad Eq.\,2.1(B)$$

$$\frac{\partial A_i}{\partial z} + \frac{1}{V_{gi}}\frac{\partial A_i}{\partial t} + jD_iA_i = -j\frac{\omega_i d_{eff}}{n_i c_0}A_pA_s^*e^{-j\Delta kz} - j\frac{\omega_i \varepsilon_0 n_i n_2}{2}|A_i|^2 A_i$$

$$-j\gamma\frac{\omega_i \varepsilon_0 n_i n_2}{2}\left(\left|A_p\right|^2 + |A_s|^2\right) A_i \qquad Eq.\,2.1(C)$$

$$\Delta k = k_p - k_s - k_i\,, D = \frac{\beta_2}{2}\frac{\partial^2}{\partial t^2} + j\frac{\beta_3}{6}\frac{\partial^3}{\partial t^3} + \cdots\,, \gamma = 2\ or\ \frac{2}{3}$$

The optical parametric amplification (OPA) process is in essense difference frequency generation (DFG) in which a pump photon with frequency ω_p splits into two lower energy photons of frequencies ω_s and ω_i. The suffixes p, s and i refer

14

pump, signal and idler waves. Since it is a parametric process, the energy conservation enforces $\omega_p = \omega_s + \omega_i$. In addition, the conversion efficiency from pump to signal and idler depends on the wavevector mismatch (Δk). For non-vanishing wavevector mismatch, $\Delta k \neq 0$, the conversion efficiency is always less than unity. When the laser intensities are high, third order nonlinear effects such as SPM and XPM should also be considered. They add additional wavevectors just like periodic poling structures in quasi-phase matching (QPM) crystals do. As a result, the phase matched wavelength is slightly changed as shown in Figure 2.1. In an OPCPA, the time-dependent SPM and XPM can also lead to a change in its phase matching bandwidth. However, it is hard to observe such time-dependent effects in reality.

Group-velocity mismatch (GVM) between interacting pulses is the first order parameter defining the performance of a broadband OPA. In particular, GVM between the pump and the signal, $\delta_{ps} \equiv \frac{1}{V_{gp}} - \frac{1}{V_{gs}}$, and idler, $\delta_{pi} \equiv \frac{1}{V_{gp}} - \frac{1}{V_{gi}}$, limits the effective interaction length and GVM between the signal and the idler, $\delta_{si} \equiv \frac{1}{V_{gs}} - \frac{1}{V_{gi}}$, determines the phase matching bandwidth. Interestingly, there is a fundamental difference between the cases in which δ_{ps} and δ_{pi} have the same or different signs [28]. When $\delta_{ps}\delta_{pi} > 0$, both the signal and the idler pulses walk away from the pump in the same direction so that the gain ceases to increase with the crystal length once it is longer than the pulse splitting length (Figure 2.2a). On the other hand, when $\delta_{ps}\delta_{pi} < 0$, the signal and idler pulses will stay trapped under the pump pulse and the gain still grows with the crystal length even if it is already much longer than the pulse splitting length (Figure 2.2b). Without loss of
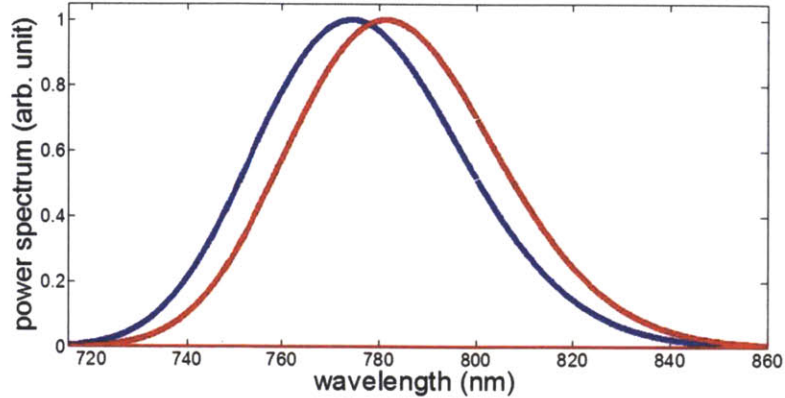
Figure 2.1 SPM and XPM add additional wave-vectors just like periodic poling structures in QPM crystals do and thus the phase matched wavelength is slightly changed.

generality, let us assume the signal moves slower and the idler moves faster than the pump pulse. After propagating for some distance, the idler overlaps with the leading edge of the pump and thus the newly generated signal is at the front of the pump. On the other hand, the signal overlaps with the trailing edge of the pump and thus the newly generated idler is at the back of the pump. Since $V_{gp} > V_{gs}$ and $V_{gp} < V_{gi}$, both the newly generated signal and idler will move towards back to the peak of the pump and continue the parametric process. Similarly, the picture explains why the signal-idler GVM increases the signal pulse duration and narrows the phase matching bandwidth.

While a numerical simulation solving Eqs. 2.1 is necessary to check how the OPCPA design works, it helps, at the initial stage of the design, to simplify Eqs. 2.1 with reasonable approximations so that back of the envelope calculations are possible. First of all, let us only consider cases where the third order nonlinear effects are negligible. Secondly, we assume that the pump bandwidth is much

narrower than the signal bandwidth. Thirdly, let us assume that the local approximation [22], [26], [29], which states that the signal is highly chirped such that the GVMs result in negligible temporal walk-off and the group-delay dispersion (GDD) encountered in the nonlinear crystal has little effect on the signal and idler pulse durations, holds valid and thus the three-wave mixing interaction at each temporal coordinate of the co-propagating pulses is effectively monochromatic in each of the signal, idler and pump waves. To examine the validity of the local approximation, let us consider a signal, with a transform-limited 1/e half-width duration τ_s, is stretched through linear chirp to $\tau'_s = \tau_s\sqrt{1 + C^2}$. We may define a characteristic GVM length $L_{GVM} = min\{\tau'_{s;i}/\delta_{si}\,;\,\tau'_{p;s}/\delta_{ps}\,;\,\tau'_{p;i}/\delta_{pi}\}$, where $\tau'_{m;n}$ is the smaller of τ'_m and τ'_n, and a GDD mismatch length $L_{GDDM} = \tau_s^2\sqrt{1 + C^2}/\left(\left.\frac{\partial^2 k_s}{\partial\omega^2}\right|_{\omega_s} + \left.\frac{\partial^2 k_i}{\partial\omega^2}\right|_{\omega_i}\right)$. The crystal length must be significantly shorter than any of these characteristic lengths and most of the broadband OPCPA is well within the constraints imposed by the local approximation.

Each temporal coordinate can thus be treated as an independent monochromatic amplifier for which the exact Jacobian elliptic function solutions for amplifier gain apply [30]. The pump, signal, and idler intensities as a function of propagation distance, z, are

$$I_p(z) = I_{p0} - I'_{p0}cn^2\left[\sqrt{\frac{I'_{p0}}{I_{p0}}}\frac{\Gamma}{\gamma}z + K(\gamma), \gamma\right] \qquad Eq.\,2.2(A)$$

$$I_s(z) = I_{s0} + \frac{\omega_s}{\omega_p}I'_{p0}cn^2\left[\sqrt{\frac{I'_{p0}}{I_{p0}}}\frac{\Gamma}{\gamma}z + K(\gamma), \gamma\right] \qquad Eq.\,2.2(B)$$

$$I_i(z) = \frac{\omega_i}{\omega_p}I'_{p0}cn^2\left[\sqrt{\frac{I'_{p0}}{I_{p0}}}\frac{\Gamma}{\gamma}z + K(\gamma), \gamma\right] \qquad Eq.\,2.2(C)$$

with parameter definitions

$$I'_{p0} = I_{p0} - (\alpha - \beta)/2$$

$$\alpha = \frac{\omega_p}{\omega_s}I_{s0} + \left(1 + \frac{\Delta k^2}{4\Gamma^2}\right)I_{p0}$$

$$\beta = \sqrt{\alpha^2 - \frac{\Delta k^2}{\Gamma^2}I_{p0}^2}$$

$$\gamma = \sqrt{\frac{I'_{p0}}{\beta}}$$

$$\Gamma = \sqrt{\frac{2\omega_s\omega_i I_{p0}d_{eff}^2}{n_s n_i n_p c^3 \epsilon_0}} \qquad Eq.\,2.2(D)$$

The parameter Γ has units 1/m and is a function of material properties and the initial pump intensity (I_{p0}). As it measures the strength of the nonlinear coupling, it is typically referred to as the "nonlinear drive". Γ can be decomposed into three parts: a constant, $\sqrt{2/c^3\epsilon_0}$, a function that depends on the experiment design, $\sqrt{\omega_s\omega_i I_{p0}}$, and a function that depends on the properties of the nonlinear crystal, $\sqrt{d_{eff}^2/n_s n_i n_p}$.

The parameter I'_{p0} has units of intensity and measures the maximum possible conversion of pump to signal and idler: $I'_{p0} \leq I_{p0}$, and they become equal

when $\Delta k = 0$. Closer inspection reveals that the maximum possible conversion efficiency, $\epsilon_{max} \equiv \frac{I'_{po}}{I_{po}}$, is a function of the normalized wavevector mismatch, $\Delta\kappa = \frac{\Delta k}{2\Gamma}$, and the initial pump to signal intensity ratio, $G' \equiv \frac{I_{po}}{I_{so}}$. Its dependence on nonlinear drive is implicit, through the wavevector mismatch normalization, and $\boldsymbol{G'}$ is a measure of the OPCPA gain. Figure 2.3 plots the maximum conversion efficiency as a function of $\Delta\kappa$ at decent $G' = 1000$. As expected, the conversion efficiency monotonically decrease as $\Delta\kappa$ gets larger, showing the intrinsic efficiency-bandwidth trade-off. On the other hand, Figure 2.4 plots the dependence of ε_{max} on G' with three different $\Delta\kappa$. When $\Delta\kappa = 0$, full conversion is always possible regardless of the initial pump to signal intensity ratio. However, when $\Delta\kappa \neq 0$, ε_{max} decreases with G' and asymptotically approaches $(1 - \Delta\kappa^2)$.

The parameter γ, with bounds $0 < \gamma < 1$, affects both the shape and period of the gain equations. Figure 2.5 plots $cn^2[u + K(\gamma), \gamma]$ with $\gamma = 0.001$ (red line) and $\gamma = 0.999$ (blue line). As γ approaches zero, the function becomes closer to a circular sinusoid. On the other hand, as γ approaches one, the peak becomes sharper and it resembles a hyperbolic secant. Of note, γ can never be equal to one because of the imbalanced signal and idler photon number and thus the energy flow in an OPA is always periodic even when the phase matching condition is perfectly met. Furthermore, the function reaches its first maximum when the normalized propagation distance, u, equals the complete elliptic integral of the first kind, $K(\gamma)$. Transforming it into the lab unit, we can express the crystal length required to reach the maximum possible conversion as

$$L_{max} = \gamma K(\gamma) \frac{1}{\epsilon_{max}} \frac{1}{\Gamma} \equiv F(\Delta\kappa, G') \frac{1}{\Gamma} \qquad Eq.\,2.3$$

L_{max} can be decomposed into two parts, one is the inverse of the nonlinear

drive and one is again a function of $\Delta\kappa$ and G'. Figure 2.6 plots $F(\Delta\kappa, G')$ as a

function of G' with three different $\Delta\kappa$. The dependence is quite intuitive: the higher

the G' the longer the required crystal length. On the other hand, the dependence of

$F(\Delta\kappa, G')$ on $\Delta\kappa$ is interesting and plotted in Figure 2.7. As $\Delta\kappa$ increases from zero,

the crystal length required to reach the maximum possible conversion also increases
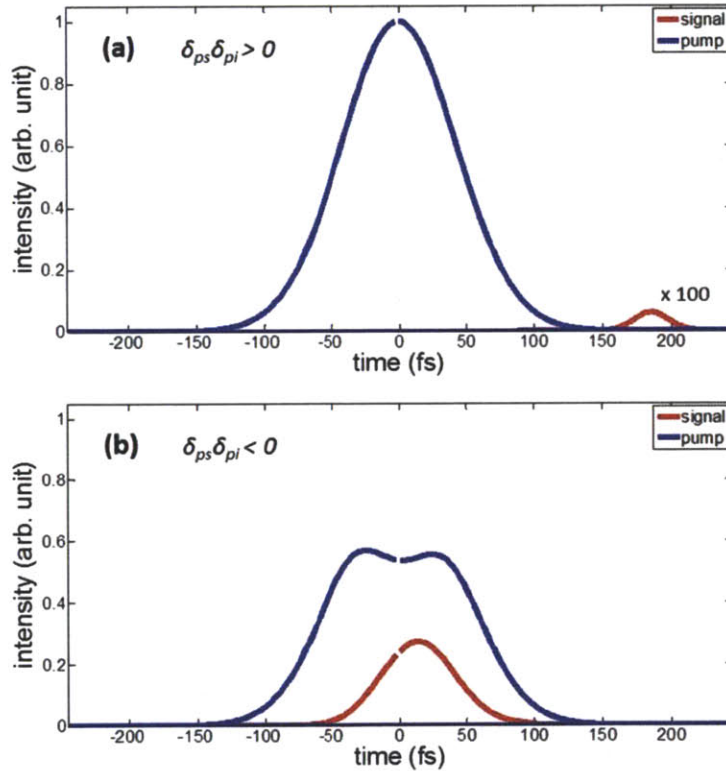
Figure 2.2 When $\delta_{ps}\delta_{pi} > 0$, both the signal and the idler pulses walk away from the pump and the gain no longer increases for propagation distances longer than the pulse splitting length. On the other hand, when $\delta_{ps}\delta_{pi} < 0$, signal and idler pulses move in opposite direction with respect to the pump and tend to stay localized under the pump pulse and the gain grows exponentially even for crystal lengths well in excess of the pulse splitting length.
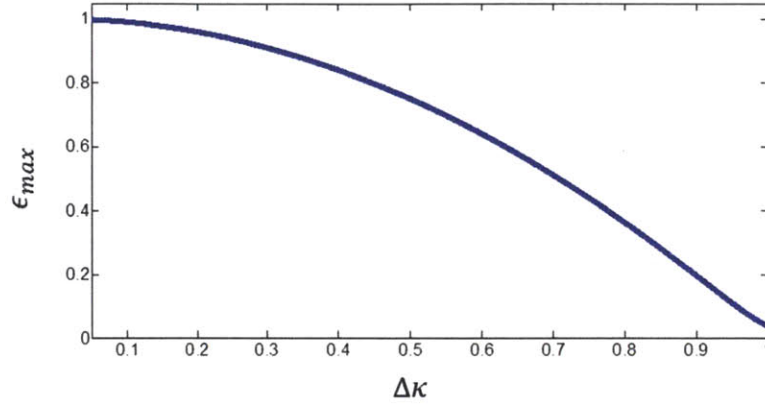
Figure 2.3 The maximum conversion efficiency as a function of $\Delta\kappa$ at decent $G' = 1000$. As expected, the conversion efficiency monotonically decrease as $\Delta\kappa$ gets larger, showing the intrinsic efficiency-bandwidth trade-off.
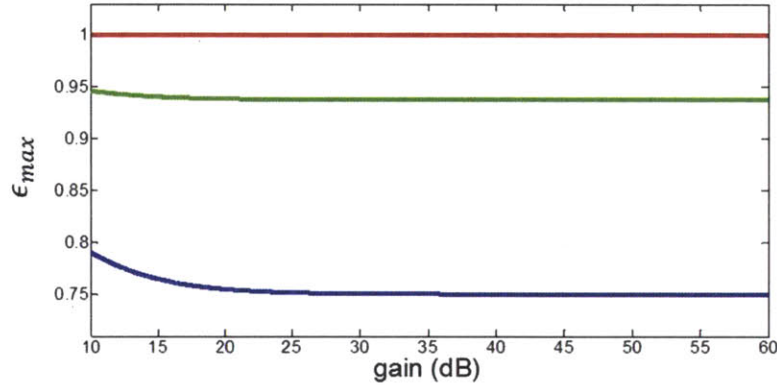
Figure 2.4 The maximum conversion efficiency as a function of G' with three different $\Delta\kappa$. When $\Delta\kappa = 0$, full conversion is always possible regardless of the initial pump to signal intensity ratio (red line). However, when $\Delta\kappa \neq 0$ (green line: $\Delta\kappa = 0.25$; blue line: $\Delta\kappa = 0.5$), ε_{max} decreases with G' and asymptotically approaches $(1-\Delta\kappa^2)$.

and the rate of change gets stronger as $\Delta\kappa$ approaches one. This behavior is very different from other nonlinear processes and is the analytical basis for the conformal profile theory introduced in Section 6.

We can further simplify Eqs. 2.2. Under the non-depleted pump approximation and the large gain limit, the evolution of the signal intensity can be simplified to an exponential function **[28], [31]**:

21

$$I_s(z) \cong \frac{I_{s0}}{4} exp(2gz) \qquad Eq.\,2.4$$

where $g = \Gamma \cdot \sqrt{1 - \Delta\kappa^2}$. Despite the many approximations, Eq. 2.4 captures the main characteristics of an OPA and its simplicity renders itself a very useful equation for back of the envelope calculations. For example, one can easily estimate the full width at half maximum (FWHM) phase matching bandwidth of a modern group-velocity matched broadband OPA by plugging the second order
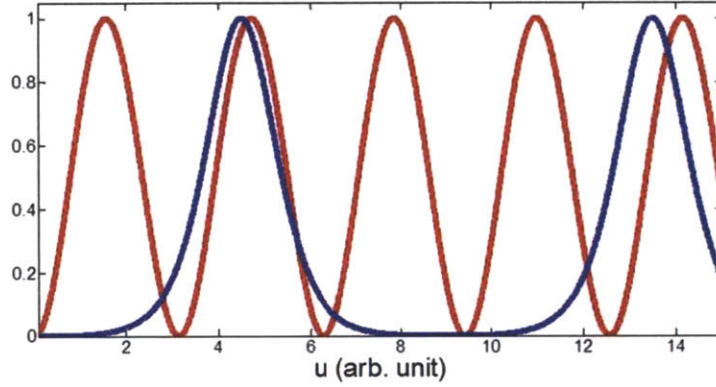
Figure 2.5 Plots of $cn^2[u + K(\gamma), \gamma]$ with $\gamma = 0.001$ (red line) and $\gamma = 0.999$ (blue line). As γ approaches zero, the function becomes closer to a circular sinusoid. On the other hand, as γ approaches one, the peak becomes sharper and it resembles a hyperbolic secant.
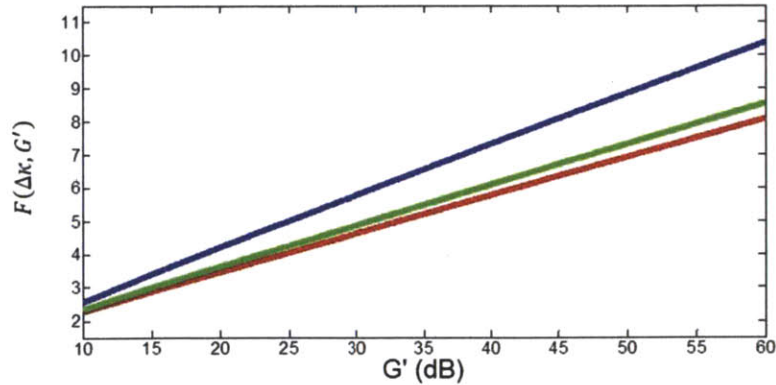
Figure 2.6 Plots $F(\Delta\kappa, G')$ as a function of G' with $\Delta\kappa = 0$ (red line), $\Delta\kappa = 0.25$ (green line), and $\Delta\kappa = 0.5$ (blue line). The dependence is quite intuitive: the higher the G' the longer the required crystal length.

Taylor expansion of $\Delta\kappa$ into Eq. 2.4 [28], [31]:

$$\Delta\omega \cong 4(ln2)^{\frac{1}{4}}\left(\frac{\Gamma}{L}\right)^{\frac{1}{4}}\frac{1}{\sqrt{GDD_s + GDD_i}} \qquad Eq.\,2.5$$

Discussion on how to achieve group-velocity matching is deferred to the next Chapter.

In the next section, we consider the problem of simultaneously maximizing the efficiency and gain bandwidth of OPCPA while avoiding super-fluorescence amplification and consequent signal-to-noise ratio degradation [22]. We employ Eq. 2.4 to gain physical insights before performing numerical analyses to investigate the temporal optimization problem. Where possible, we provide experimental data from a state-of-the-art short-wavelength infrared (SWIR) OPCPA system to support the analysis. We find that not only the efficiency and bandwidth but also the signal-to-noise ratio are each strongly tied to the temporal profiles of the interacting waves and the local phase-mismatch across the interacting pulses and we explain, through a model of simultaneous signal and noise amplification, how the overall sacrifice in these qualities can be minimized. Furthermore, we demonstrate a sensitivity of the parameters that optimize these qualities to the total gain of the amplifier. As a result, we conclude that careful optimization of seed chirp is necessary at each stage of a multi-stage amplifier in order to prevent significant noise buildup while maintaining the needs in gain and bandwidth of a high-energy, broadband OPCPA. We present guidelines for the stage-by-stage optimization, including an empirical formula for optimal signal and pump pulse duration ratio based on numerical simulations and semi-analytical investigation.
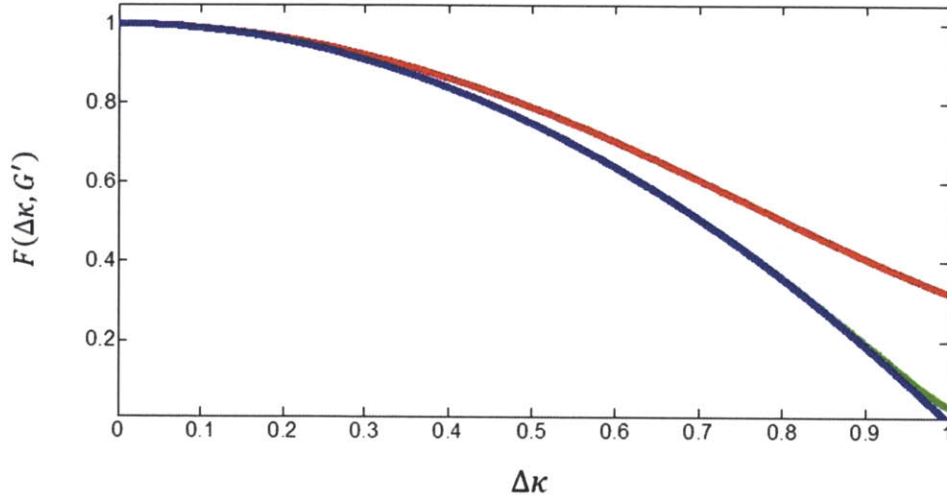
Figure 2.7 Plots $F(\Delta\kappa, G')$ as a function of $\Delta\kappa$ with $G' = 10$ (red line), $G' = 10^3$ (green line), and $G' = 10^5$ (blue line). The dependence of $F(\Delta\kappa, G')$ on $\Delta\kappa$ is interesting: as $\Delta\kappa$ increases from zero, the crystal length required to reach the maximum possible conversion also increases and the rate of change gets stronger as $\Delta\kappa$ approaches one.

2.2   Temporal optimization of an OPCPA

The predominant issue in the optimization of efficiency in parametric amplification, whether the signal pulse is chirped or unchirped, is the spatio-temporal variation of the small-signal gain due to its dependence on the pump intensity, $g\left(I_p(t; x; y)\right)$. This variation prevents all transverse components of the pump wave from becoming fully depleted (by conversion to signal and idler) simultaneously (Figure 2.8a); beginning with its peak, during propagation the most intense coordinates of the pump wave are depleted first. The weaker components are depleted later, only after a reversal of the transfer of energy from pump to signal (i.e., "back-conversion") has already set in at the peak. Begishev *et al.*

24

identified the existence in theory of a "conformal" signal profile, for every possible pump profile, that would allow simultaneous depletion of all transverse coordinates of the pump by providing the appropriate requirement for gain at each transverse coordinate [32], [33]. However, in practice, such conformal pump/signal profile pairs are difficult to obtain, even in the simplest case of flat-top profiles. Several works have shown that a flattened pump profile (without also a flattened seed profile) can already significantly improve conversion efficiency [34–37]. Still, except in rare cases where the design of the pump light source allows implementation of temporal and spatial beam shaping without reduction of the available pulse energy, losses due to shaping techniques can outweigh the resulting improvement in conversion efficiency.

In OPCPA the problem of temporal variation of small-signal gain is further complicated by the signal chirp. In this case, the mapping of signal frequency to
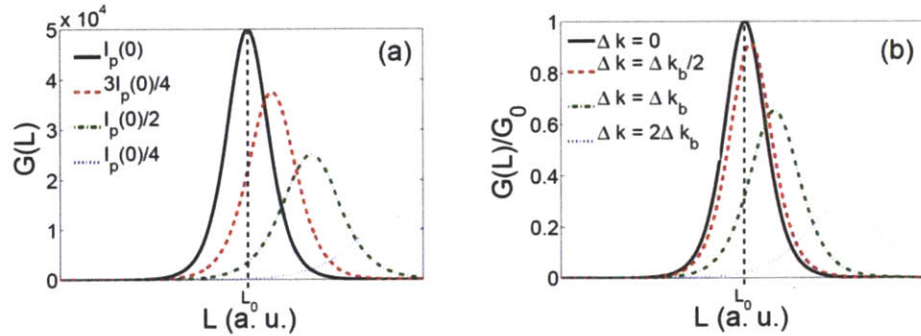
Figure 2.8 Signal gain versus propagation length for a phase-matched parametric amplifier that has a peak gain $G_0 = 5 \times 10^4$. In (a), gain curves corresponding to lower pump intensity are also shown (representing, for example, the amplification that occurs along the wings of a pump pulse relative to its peak). In (b), the effect of increasing Δk is shown, with an initial pump intensity $I_p(0)$ for all curves. Δk_b is the wave-vector mismatch that reduces the gain at L_0 by e^{-1}.

temporal coordinate adds a time dependence of small-signal gain $g\left(I_p(t); \Delta k(t)\right)$ through the local wave-vector mismatch, $\Delta k(t) = k_p - k_s(t) - k_i(t)$; this also prevents simultaneous depletion of all temporal coordinates of the pump wave in the same way as the temporal variation of the pump intensity (Figure 2.8b). Even when only a small well-phase-matched portion of the full phase matching bandwidth of the amplifier (i.e., $g\left(\Delta k(\omega)\right) \cong g(\Delta k = 0)$) for all ω) is employed, the temporal mapping of signal frequency creates preferential amplification of those frequency components that overlap temporally with the most intense part of the pump pulse. In other words, gain narrowing results in spectral narrowing. The full phase matching bandwidth of the amplifier may be preserved by keeping the seed pulse short enough, relative to the pump pulse, that the pump intensity remains more-or-less constant across the duration of the seed. However, the increased amplifier bandwidth comes with a decrease in conversion efficiency: only a small fraction of the pump pulse is depleted.

To gauge the maximum possible conversion efficiency of the amplifier, the concept of the temporal region of significant gain of the pump pulse is useful. This is particularly simple to define in the case of a parametric amplifier with unchirped signal (Figure 2.9a). Consider parametric amplification of a seed pulse with spectrum centered at signal frequency ω_s by a pump pulse with center frequency ω_p such that $\omega_p = \omega_s + \omega_i$. From Eq. 2.4, the gain is

$$G = \frac{I_s(L)}{I_{s0}} \cong \frac{1}{4} exp(2gL) \qquad Eq.\, 2.6$$

which, in the case of perfect phase matching, can be recast in the form

$$G \cong \frac{1}{4}exp(2\Gamma L) \qquad Eq.\,2.7$$

In this case, since $\Gamma \sim \sqrt{I_p}$, the gain is time dependent and follows the pump pulse

intensity profile: $G(t) \sim exp\left(\sqrt{I_p(t)}\right)$. $G(t)$ is plotted in Figure 2.9a alongside $I_p(t)$

for a Gaussian pump pulse. The peak gain is 100 and the plotted gain profile is

normalized to one. It is clear from Figure 2.9a that significant gain will only be

possible for a seed pulse overlapped with the pump pulse within a central region
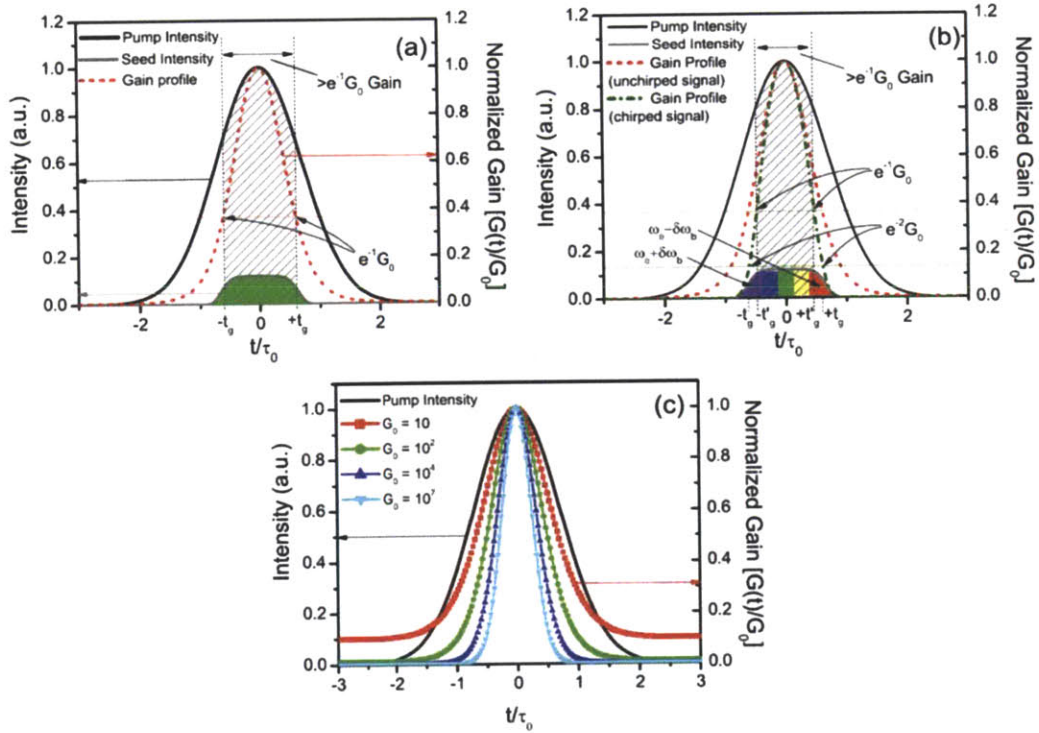
Figure 2.9 (a) Normalized Gaussian pump pulse profile (black, solid) and corresponding temporal gain profile (red, dashed) of an unchirped phase-matched parametric amplifier with a peak gain $G_0 = 100$. The shaded region indicates the region of the pump pulse where gain is $\geq e^{-1}G_0$. A suitable seed pulse is also indicated. (b) The equivalent of (a) but assuming a seed spectrum extending from $\omega_s - \delta\omega_b$ to $\omega_s + \delta\omega_b$ and chirped such that frequencies $\omega_s \pm \delta\omega_b$ just fit within the region of significant gain corresponding to (a). (c) Normalized pump intensity profile and corresponding gain profiles for various values of the peak gain for an unchirped phase-matched amplifier.

about $t = 0$. Defining gain to be significant when $G(t) \geq e^{-1}G_0$, where $G_0 = G(t = 0)$ is the peak gain, we may identify a region of significant gain $t < |t_g|$ corresponding to the shaded region of Figure 2.9a. Let us calculate the centroid bounds, $\pm t_g$, corresponding to a gain $G(t_g) = e^{-1}G_0$ in the case of perfect phase matching. If we define the small-signal gain $g(t) = 2\gamma(t)L$ and $g_0 = g(t = 0)$, we obtain

$$\frac{g(t_g)}{g_0} = \sqrt{\frac{I_p(t_g)}{I_p(0)}} = \frac{g_0 - 1}{g_0} \qquad Eq.\,2.8$$

For a Gaussian pump pulse, described by $I_p(t) = I_0 \cdot exp(-(t/\tau_0)^2)$ with FWHM duration $\Delta t_p = 2\tau_0 \cdot \sqrt{ln2}$, we may rearrange Eq. 2.8 to find

$$t_g = \frac{\Delta t_p}{2\sqrt{ln2}}\sqrt{-2ln[1 - 1/ln(4G_0)]} \qquad Eq.\,2.9$$

The parameter t_g measures the region of significant gain for the amplification of an unchirped, phase-matched signal. Since significant pump depletion will typically occur only where there is significant signal gain, t_g thus gives a measure of the maximum possible energy extraction from the pump. Note that t_g is a function of the peak gain G_0, and that a power amplification stage, which employs a low value of G_0, will have a significantly larger gain centroid width than a pre-amplification stage with high G_0. Thus, the power amplier can extract more energy from the pump pulse, resulting in a significantly higher maximum conversion efficiency. Figure 2.9c plots the temporal gain profile of an amplifier with unchirped signal pulse for several values of G_0, each curve normalized to one, and Table 1 tabulates the results. The discrepancy in t_g for pre-

and power amplifiers implies that a different seed pulse chirp (given a fixed pump pulse duration) will optimize amplification for each stage. For example, a power amplifier stage with $G_0 = 10^2$ has 1.5 times wider a region of significant gain than a preamplifier stage with $G_0 = 10^5$.

Table 1. Width of temporal region of significant gain versus peak gain

G_0	10	10^2	10^3	10^4	10^5	10^6	10^7
$2t_g/\Delta t_p$	0.955	0.725	0.609	0.534	0.483	0.443	0.412
$2t_g'/\Delta t_p$	0.726	0.571	0.483	0.425	0.385	0.353	0.335

For an OPCPA, we need to include also the temporally varying wave-vector mismatch $\Delta k(t)$ of the interacting pulses. According to Eq. 2.6, alignment of the signal and pump pulses such that $\Delta k(t = 0) = 0$ leads to a reduction in the gain at the wings of the signal pulse from wave-vector mismatch. In Figure 2.9b, the red (dashed) curve represents the gain profile of the unchirped signal pulse of Figure 2.9a, while the green (dot-dashed) curve includes the effects of the temporally-varying wave-vector mismatch and the resulting decrease in the small-signal gain. The signal pulse is linearly chirped such that the edges of the phase matching bandwidth, $\omega - \omega_s = \pm\delta\omega_b$, are mapped to coordinates $t = \pm t_g$. If we define the gain bandwidth, $2\delta\omega_b$, so that $G(\omega_s \pm \delta\omega_b) = e^{-1}G(\omega_s)$, the temporal region $-t_g' < t < t_g'$ where $G(t_g') = e^{-1}G_0$, is narrower for chirped pulses than that for unchirped ones due to reduction of the small-signal gain due to $\Delta k(t)$.

In principle, as the signal chirp is increased, the region $-t_g < t < t_g$ will on average contain signal frequencies that are closer to the phase-matched frequency; Δk remains small across the bounds and t_g' tends to t_g, increasing the

maximum possible conversion efficiency. However, the larger the chirp, the smaller the portion of the signal bandwidth that will fit within the region $-t'_g < t < t'_g$, and thus the smaller the effective amplifier bandwidth. In the other limiting case of vanishingly small chirp, all the seed colors see approximately the peak pump intensity; in this case, t'_g is determined solely by phase matching, and $t'_g \ll t_g$. The bandwidth approaches the full phase matching bandwidth, but on the other hand the energy extraction is limited since only a small temporal window of the pump can be depleted.

The trade-off between amplifier conversion efficiency and bandwidth makes the optimization of the seed chirp subject to the user's desired characteristics of the pulse source. The maximization of peak power is a typical goal and will inform our optimization analysis. In this case, maximization of the gain-bandwidth product is desired, and the optimal seed chirp can be estimated by analysis of Eq. 2.6. Figure 2.10 plots the efficiency-bandwidth product calculated from Eq. 2.6 for given values of the peak gain G_0, varying the seed chirp and thus influencing the corresponding mismatch function $\Delta k(t)$. Since significant energy extraction from the pump occurs only where there is signal gain, *efficiency* was calculated as the fraction of pump energy included in the bounds $-t'_g < t < t'_g$; the *bandwidth* corresponds to $2\delta\omega_b/2\pi$, where $\omega_s \pm \delta\omega_b$ are the frequencies mapped at $t = \pm t'_g$. Figure 2.10 demonstrates a clear optimum GDD for each value of G_0, as expected, since efficiency increases and bandwidth decreases with increasing chirp. The parameters t'_g corresponding to the optimum GDD at each G_0 are tabulated in the second line of Table 1. The parameters $2t_g/\Delta t_p$ and $2t'_g/\Delta t_p$ exhibit the same

behavior: larger peak gains require narrower regions of significant gain. Consistently, $t'_g < t_g$.

Note that for this analysis and in all theoretical examples in this section we consider the case of an OPCPA with a broad phase matching bandwidth achieved through matched signal and idler group velocities, with first-order approximation $\Delta k(\omega) \sim (\omega - \omega_s)^2$. The analysis, however, can also be applied to the group-velocity mismatched case, where $\Delta k(\omega) \sim (\omega - \omega_s)$. In this case there will be different quantitative results, but similar trends.

We now turn to the matter of degradation of signal-to-noise ratio during amplification, where the amplifier is seeded by both signal and super-fluorescence noise. An important difference between signal gain and noise gain can be understood by means of the same conceptual picture used above (Figure 2.9a and 2.9b). Noise photons generated by spontaneous parametric generation are equally distributed in time and frequency; whether the noise pulse starts at the single-photon level or from amplification of super-fluorescence generated in a previous stage, there is high statistical certainty that a noise photon well phase-matched for parametric amplification exists at each point in time. The noise gain profile, therefore, is like the signal gain profile of an unchirped, phase-matched parametric amplifier, with $\Delta k = 0$ at all t. Thus, in OPCPA, at each temporal coordinate of the interacting pulses the local gain of signal and noise photons is different: the noise temporal gain profile is determined solely by the local pump intensity, while the signal temporal gain profile is further reduced by the instantaneous wave-vector mismatch. Simultaneous amplification of signal and noise is thus depicted by

31

Figure 2.9b, where the unchirped-pulse amplifier gain profile (red, dashed) represents the noise, and the chirped-pulse amplifier gain profile (green, dot-dashed) represents the signal. Apart from $t = 0$, where both signal and noise photons experience $\Delta k = 0$, there is higher gain for noise than for signal. In the example of Figure 2.9b, at $t = \pm t_g$, the signal photons experience a gain $< e^{-1}$ lower than that of coincident noise photons that are perfectly phase-matched.

The degradation in signal-to-noise ratio to be expected during amplification, arising from the difference between the total noise gain and total signal gain, can be estimated, therefore, by the area between the two gain curves of Figure 2.9b, and depends on the signal pulse chirp. Figure 2.10 (dashed line) plots the difference between noise and signal gain as a function of seed chirp for the case $G_0 = 10^6$. The gain discrepancy approaches zero at a chirp slightly higher than that which maximizes the gain-bandwidth product. Optimum peak power, therefore, may be obtained with reasonably low degradation of signal-to-noise ratio.
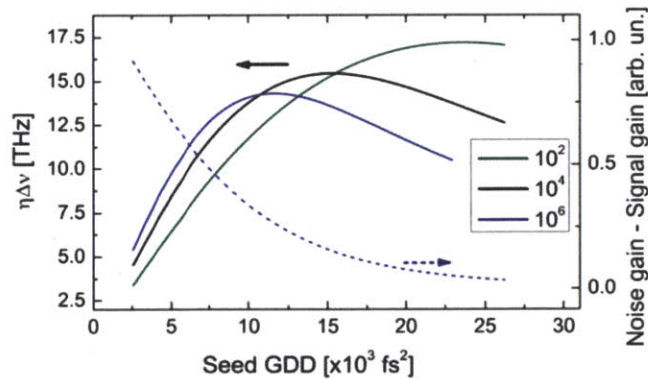
Figure 2.10 (solid lines) Efficiency-bandwidth products obtainable from the OPCPA for different values of the seed chirp (GDD) and peak gains of 10^2, 10^4 and 10^6. (dashed curve) Total noise gain subtracted by total signal gain for $G_0 = 10^6$.
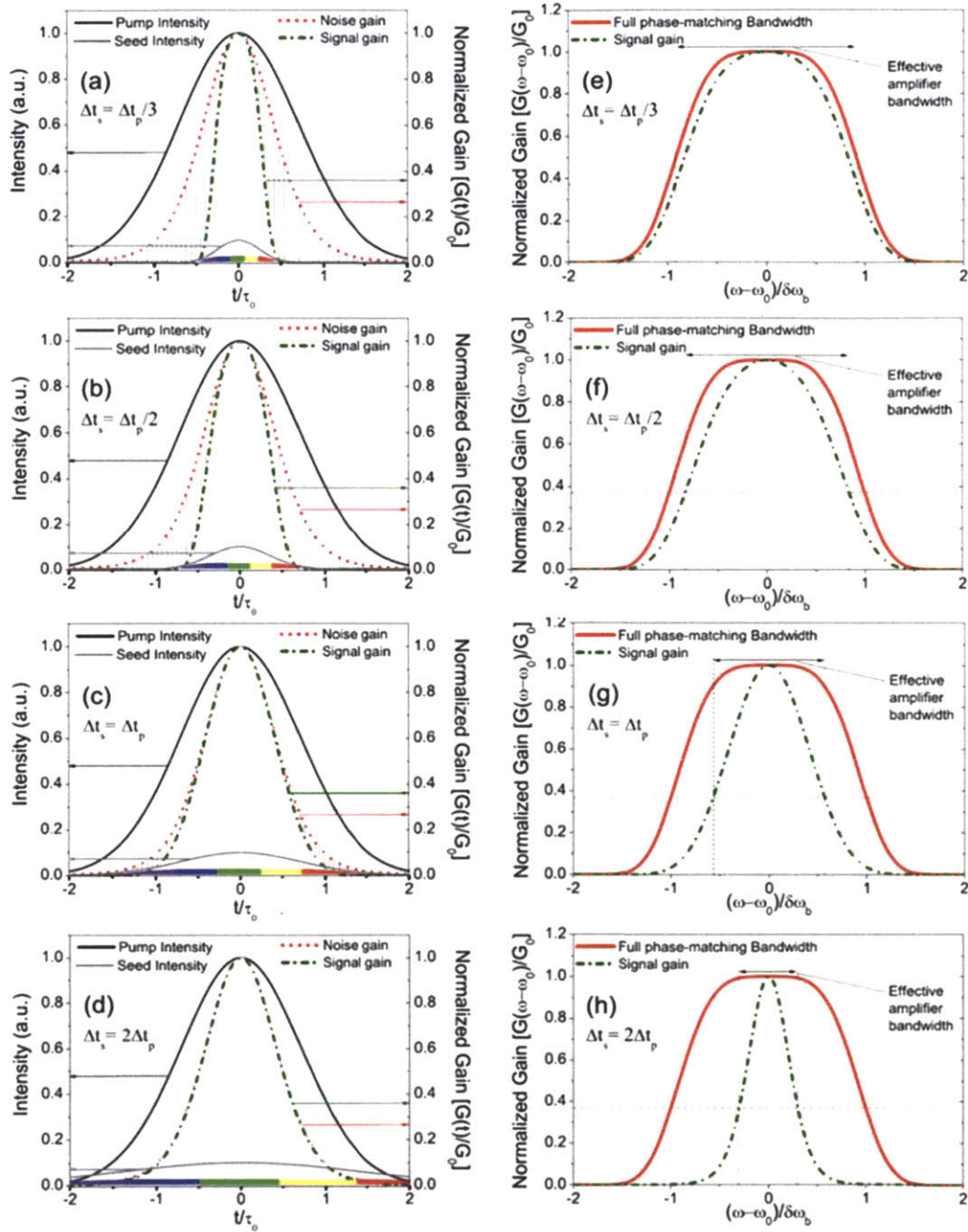
Figure 2.11 (a-d) Gaussian pump (black, solid) and seed (gray, solid) intensity profiles with corresponding signal gain (green, dot-dashed) and noise gain (red, dotted) profiles for several ratios of seed and pump pulse durations ($\Delta t_s/\Delta t_p$). The shaded region represents the difference between noise and signal gain. The chirp of the signal pulse is represented by colored bars. (e-h) Corresponding signal gain profiles (green, dot-dashed) in the frequency domain, plotted alongside the full phase-matching bandwidth of the amplifier (red, solid).

A full summary of the effects induced by the signal pulse chirp is presented in Figure 2.11. Here we consider Gaussian pump and seed profiles measured by their FWHM, Δt_p, Δt_s, respectively. With $\Delta t_s = \Delta t_p/3$ the signal pulse fits within a largely unvarying portion of the pump intensity profile (Figure 2.11a). As a result, there is little clipping of the signal pulse at the wings due to gain narrowing, and the effective amplifier bandwidth is nearly the full phase matching bandwidth (Figure 2.11e). However, since the signal carrier frequency sweeps quickly in time, so does $\Delta k(t)$, and as a result the gain profile of the signal is much narrower than that of the noise. The narrow signal gain profile means the conversion efficiency will be small, as only a fraction of the pump pulse will be depleted, and the large area between signal and noise gain profiles means the signal-to-noise ratio will strongly degrade after amplification. As the signal chirp increases (Figure 2.11b-d), the signal gain profile widens relative to the noise gain profile, resulting in larger conversion efficiency and higher signal-to-noise ratio. On the other hand, since there is more clipping of the signal pulse during amplification, there is a narrower effective amplifier bandwidth (Figure 2.11f-h). The extreme is shown in Figure 2.11d, where $\Delta t_s = 2\Delta t_p$. Here, the very slow variation in signal frequency, resulting in a slow variation in $\Delta k(t)$, makes the noise and signal gain profiles nearly identical. However, since only a small portion of the signal bandwidth fits within the central part of the pump pulse, there is severe spectral clipping, and the effective amplifier bandwidth is much smaller than the phase matching bandwidth (Figure 2.11h). The nearly equal signal and noise gain seen in Figure 2.11d can be understood from another point of view. Since the effective amplifier bandwidth

covers only the flat, phase-matched central region of the phase matching bandwidth, Δk is essentially zero over the full significant gain region of the pump pulse. Therefore, there is little preferential amplification of the noise.

The analytical and conceptual models introduced so far allowed us to establish trade-offs between conversion efficiency, gain bandwidth and signal-to-noise ratio optimization in OPCPA. In order to test these predictions in the saturation regime of amplification, where significant pump depletion occurs, we numerically integrated the nonlinear coupled equations describing the parametric amplification process. Our simulations exclude the spatial transverse dimensions, allowing isolation of the temporal behavior. We consider a broadband OPCPA system that is known to be sensitive to super-fluorescence. The amplifier is pumped by a 9-ps FWHM Gaussian pulse at 1.047 μm and seeded by a broadband pulse at 2.094 μm, for operation around degeneracy. The interaction was calculated in a 3-mm long periodically-poled stoichiometric lithium tantalate (PPSLT) crystal. The seed had a super-Gaussian spectrum with FWHM bandwidth of 69 THz, which well matches the 15-fs (~2-optical-cycle) phase matching bandwidth of the amplifier. These input parameters are close to the experimental conditions of Ref. [38], chosen for ease of comparison between simulations and experiments. We will describe the second-order nonlinear interaction occurring in the parametric amplifier among three fields labeled $j = s, i, p$, corresponding respectively to the seed, the idler and the pump beams. These fields propagate with carrier angular frequency ω_j and wave-vector k_j, and experience the phase mismatch $\Delta k = k_p -$

$k_s - k_i$. We consider the plane-wave limit and represent the total electric field as [39], [40]:

$$E(z,t) = \frac{1}{2}\Big\{ \; A_S(z,t) \cdot e^{j(\omega_s t - k_s z)} \; + $$

$$A_i(z,t) \cdot e^{j(\omega_i t - k_i z)} \; + $$

$$A_p(z,t) \cdot e^{j(\omega_p t - k_p z)} + c.c. \; \Big\} \qquad Eq.\,2.10$$

where $A_j(z,t)$ denotes the field complex amplitude. The coupled equations describing the second-order interaction of the fields are derived from the nonlinear propagation equation [41]:

$$\frac{\partial^2}{\partial z^2} E(z,t) - \mu_0 \frac{\partial^2}{\partial t^2} D(z,t) = \mu_0 \frac{\partial^2}{\partial t^2} P_{NL}(z,t) \qquad Eq.\,2.11$$

applied on the total field $E(z,t)$. Here, $D(z,t) = \varepsilon_0 \int \varepsilon_r(\tau) E(z, t - \tau) d\tau$ is the linear electric induction field accounting for the dispersion of the medium [42], and $P_{NL} = 2\varepsilon_0 d_{eff} E^2(z,t)$ is the nonlinear polarization, where d_{eff} is the effective second-order nonlinear coefficient. Eq. 2.11 was solved by the split-step method [43] in the frequency domain. The use of picosecond pump pulses and strongly-chirped seed pulses required a large number of sampling points (2^{14}) in the time and frequency domains. Periodic poling was accounted for by changing the sign of d_{eff} along the propagation coordinate z, mimicking the effective process taking place in the nonlinear crystal; the drawback of this approach is that Δk is large for all signal wavelengths, and thus the split-step method requires slicing the crystal into very short steps, Δz, in order to suitably integrate the fields over their entire bandwidth. In our case, numerical errors could be reduced suitably by setting $\Delta z = 0.1 \mu m$, much smaller than the used poling period, $\Lambda = 31.2 \mu m$.

It is important to point out that the general representation of fields given in Eq. 2.10 assumes that pump, signal and idler are three separate fields. This is not true when signal and idler bandwidths overlap and also propagate with the same direction and polarization. In practice, degenerate OPCPA ($\omega_s = \omega_i$) rarely employs a collinear geometry: a small non-collinear angle between signal and idler is used both to allow their separation after amplification (since they have opposite temporal chirp), and to avoid signal-idler interference for preservation of carrier-envelope phase of the signal. We model such a system here.

In order to test the dependence of the optimization problem on the desired peak gain, the simulations were run for 3 configurations: $E_p/E_s = 10^2$, $E_p/E_s = 10^4$ and $E_p/E_s = 10^6$, where E_p/E_s is the initial pump to signal energy ratio. The parameter E_p/E_s is closely related to the maximum gain, G_{max}, i.e., the gain that in principle could be obtained from the OPCPA if all the pump energy could be transferred to the signal and idler, by the approximate equivalence $G_{max} \cong E_p/E_s/2$. For each of the configurations we performed the following analysis:

- We changed the duration of the chirped seed pulse from 1 to 12.5 *ps* by introducing a group delay dispersion variable from 2500 to 30000 *fs²*, in steps of 2500 *fs²*;

- For each given seed duration, the amplification process was evaluated for a range of pump peak intensities, experimentally corresponding to changing equally the pump and seed beam diameters at the input surface of the crystal. This action, increasing the pump intensity at a fixed propagation length,

corresponds to increasing the gain, and increases the degree of amplifier saturation;

- We deduced the pump intensity giving the highest conversion efficiency η_{max}, calculated as the sum of amplified signal and idler energies divided by the initial pump energy, and we evaluated the corresponding efficiency-bandwidth product ($\eta_{max} \cdot \Delta v$).

We note, since η_{max} and $(\eta \cdot \Delta v)_{max}$ occur at approximately the same value of gain [13], $\eta_{max} \cdot \Delta v$ is a close approximation to $(\eta \cdot \Delta v)_{max}$, and this approach to evaluating the maximum efficiency-bandwidth product at each seed duration is well justified. A typical set of simulations is reported in Figure 2.12, which shows the efficiency and bandwidth of the amplifier for various seed durations and pump peak intensities, calculated in the case $E_p/E_s = 10^4$. Looking at Figure 2.12, one can make the following observations, confirming the behavior predicted previously and adding new observations pertaining to the pump-depletion regime: (i) the amplified bandwidth decreases with increasing seed pulse duration, due to the progressively lower gain experienced by the wings of the spectrum; (ii) for each seed pulse duration there is an optimum peak intensity that guarantees the highest efficiency η_{max} [squares in Figure 2.12a] (higher intensities induce back-conversion at the peak of the pump pulse that exceeds additional conversion at the wings); (iii) as seed duration is increased, the maximum possible conversion efficiency increases; (iv) for a given seed duration, as the amplifier reaches maximum conversion the bandwidth increases with intensity due to saturation of gain at the center of the pulse and preferential amplification at the wings.
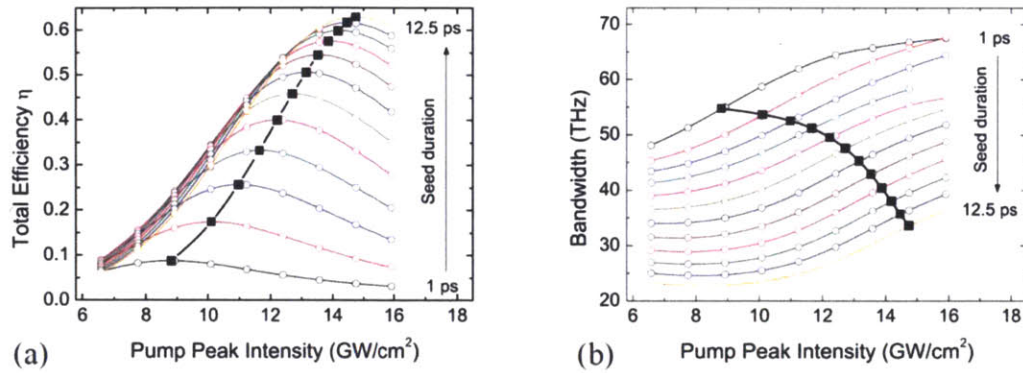
Figure 2.12 Study of efficiency (a) and bandwidth (b) of the OPCPA process for various seed durations and pump peak intensities, for the case $E_p/E_s = 104$. Squares of panel (a) highlight the highest efficiency obtainable for a given seed duration; the corresponding bandwidths are indicated as filled squares in panel (b).
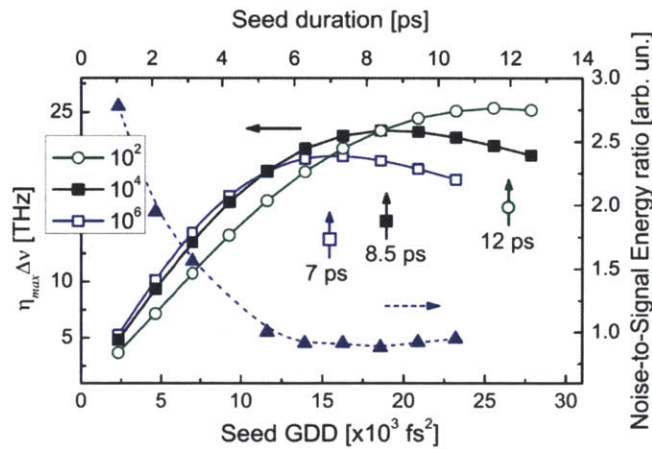

Figure 2.13 Best gain-bandwidth products obtainable from the OPCPA for various seed durations and pump-to-signal energy ratios of $E_p/E_s = 10^2$ (circles), $E_p/E_s = 10^4$ (filled squares) and $E_p/E_s = 10^6$ (open squares). The seed durations corresponding to the best performances at the three operating regimes are shown. The increase in noise relative to signal during amplification is shown for the data points of the $E_p/E_s = 10^6$ curve (triangles).

The behavior of $\eta_{max} \cdot \Delta v$ deduced from this analysis is demonstrated in

Figure 2.13. For example, the optimal seed duration when $E_p/E_s = 10^4$ (filled

squares) is 8.5 *ps*, corresponding to $0.94 \cdot \Delta\tau_p$. This value contrasts that of the

cases $E_p/E_s = 10^2$ (open circles) and $E_p/E_s = 10^6$ (open squares), also calculated.

This behavior in the depleted-pump regime of amplification matches the behavior predicted previously for the non-depleted-pump regime; each amplification regime requires a particular seed chirp in order to obtain the best performance in gain-bandwidth product. In particular, higher initial pump-to-seed energy ratios call for shorter seed pulses.

The trend with increasing E_p/E_s is in very good agreement with Table 1 for increasing G_0. Fitting the results of Figure 2.13 with the analytical formula for the scaling of $2t_g/\Delta t_p$ with peak gain, Eq. 2.9, using a variable correction coefficient, we find excellent agreement. The results are plotted in Figure 2.14. We find

$$\left(\Delta t_s/\Delta t_p\right)_{opt} \approx \alpha\sqrt{-2ln[1 - 1/ln(4G_0)]} \qquad Eq. 2.12$$

where $\alpha = 2.1$, or $(\Delta t_s)_{opt} \cong 1.7 \cdot \left(2t_g\right)$. Here, the extra factor of 1.7 can be attributed mostly to the increase in temporal gain profile width due to amplifier saturation: gain at the peak of the pump pulse saturates before gain at the wings does, which pushes out the wings of the gain profile. Even with the effects of saturation, however, the simple non-pump-depletion-regime analysis still recovers the scaling of $\left(\Delta t_s/\Delta t_p\right)_{opt}$ with G_0. Note, the factor α also accounts implicitly for the particular spectral intensity profile of the signal, $I_s(\omega)$, a characteristic of the amplifier not included in the analytical model.

To confirm also the behavior of signal-to-noise ratio as a function of the seed chirp as predicted previously, we redid the simulations corresponding to the data points of Figure 2.13 for the $E_p/E_s = 10^6$ case (open squares), adding initial noise distributions. To capture the features of super-fluorescence noise, to the signal and idler fields we add initial noise fields modeled as complex stochastic
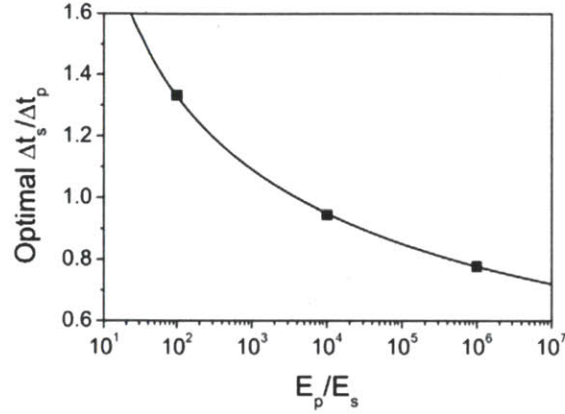
Figure 2.14 Fit of $(\Delta t_s/\Delta t_p)_{opt}$ values from Figure 2.13 versus E_p/E_s (squares) using the gain centroid width formula, Eq. 2.12 (solid line).
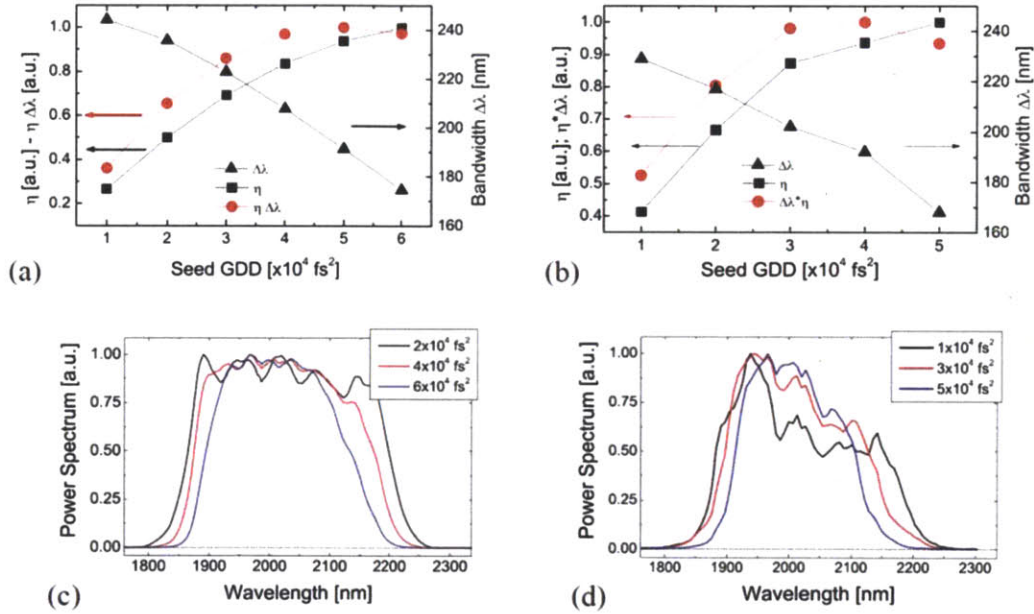
Figure 2.15 Comparison between numerical simulations [(a),(c)] and experiments [(b),(d)] for a 3-mm long, 9-ps pumped, PPSLT-based amplifier. (a)-(b) Best efficiencies and bandwidths as a function of seed chirps. (c)-(d) Amplified spectra corresponding to the maximum efficiencies for the three given seed chirps.

random variables for each frequency component. These noise fields model, in a semi-classical picture, the incoming vacuum fluctuations that are transformed into super-fluorescence by the amplifier. The frequency-domain real and imaginary

41

parts of these complex stochastic variables are independent and Gaussian-distributed with zero-mean and variance that scales with the quantum energy, $\sigma^2 = \hbar\omega$ [44]. In this example, the amount of initial noise energy (signal plus idler) in frequencies falling within the signal and idler phase matching bandwidth amounts to 3.8% of the initial signal pulse energy. Figure 2.13 plots the calculated degradation of signal-to-noise ratio as a function of seed chirp (triangles). As predicted, the signal-to-noise ratio performance improves significantly as the seed chirp increases, leveling off at close to the same value that maximizes the efficiency-bandwidth product. This completes the confirmation of a general conclusion regarding OPCPA optimization: a small sacrifice in amplifier bandwidth relative to the full phase-matching bandwidth of the amplifier simultaneously allows optimal efficiency-bandwidth product and good robustness of signal-to-noise ratio.

As a proof that the numerical model we used for the optimization process is consistent with a real OPCPA system, we compared simulations with the measured spectra and efficiencies from an amplifier with the same parameters and seeded by pulses with bandwidths corresponding to 32 fs [45]. Figure 2.15 illustrates the very good qualitative and quantitative agreement between numerical (a) and experimental (b) gain and bandwidth trends. In the same figure, we compare calculated (c) and measured (d) amplified spectra corresponding to the best total efficiency at the given seed chirp. This match provides confidence in the use of the trends and scaling rules found above to inform the design of an OPCPA system.

We have investigated the optimization of OPCPA when broad bandwidth, high gain, and suppression of super-fluorescence noise are each important. Noteworthy conclusions of the analysis are listed below.

1. In OPCPA, the simultaneous amplification of signal and background super-fluorescence noise can be treated as simultaneous chirped-pulse and non-chirped-pulse amplification (*i.e.*, simultaneous OPA and OPCPA), respectively. Instantaneous signal amplification is sensitive both to the local pump intensity and instantaneous wave-vector mismatch, whereas the instantaneous noise amplification is sensitive to only the local pump intensity.

2. Like the conversion efficiency and bandwidth of the amplifier, the robustness of signal-to-noise ratio is tied to the ratio of initial signal and pump pulse durations, $\Delta t_s / \Delta t_p$. Considering all three qualities simultaneously, as seed chirp is increased, the maximum conversion efficiency increases, the amplifier bandwidth decreases, and the signal-to-noise ratio increases. A small sacrifice in effective amplifier bandwidth relative to the full phase-matching bandwidth of the amplifier can significantly improve the signal-to-noise ratio.

3. The optimal ratio of pump and seed durations also depends on the gain. The scaling of the optimum $\Delta t_s / \Delta t_p$ with the peak gain of the amplifier is well captured by an analytic formula, Eq. 2.12. For example, the difference in optimum $\Delta t_s / \Delta t_p$ between G_0 values of 10^2 and 10^5 is 1.5.

These features of OPCPA have a number of practical consequences for the design of an amplifier. A high-gain OPCPA is often split into two or more stages, including pre-amplification, with high gain, and power amplification, with relatively low gain (for example, see Figure 2.16.) The benefit of this practice can be understood by means of Figures 2.9a, 2.10, and 2.13: as peak gain decreases, both the maximum achievable conversion efficiency and maximum achievable efficiency-bandwidth product increase. Therefore, by placing most of the gain in a pre-amplifier stage, and only 10^2 gain or less in the final stage, the final peak power of the amplifier can be maximized.

Several realistic scenarios in multi-stage OPCPA are subject to problems in design if separate optimization of the seed chirp in each amplification stage is disregarded, and super-fluorescence noise suppression is a concern. For example:

1. In the schematic of Figure 2.16a, if the signal stretcher is designed to optimize chirp for maximum efficiency-bandwidth product in the power amplification stage, $\Delta t_s / \Delta t_p$ will be larger than optimal in the pre-amplifcation stage, causing unwanted spectral clipping that would result in a signal bandwidth too narrow to properly seed the power amplifier. To recover the lost bandwidth, the operator of this system has no choice but to drive the pre-amplification stage into heavy saturation. The resulting loss in efficiency in the pre-amplifier may not be problematic, but the heavy saturation would result in strong degradation of signal-to-noise ratio, since high gain would take place at the wings of the pulse, where there would be a large discrepancy between noise and signal gain.
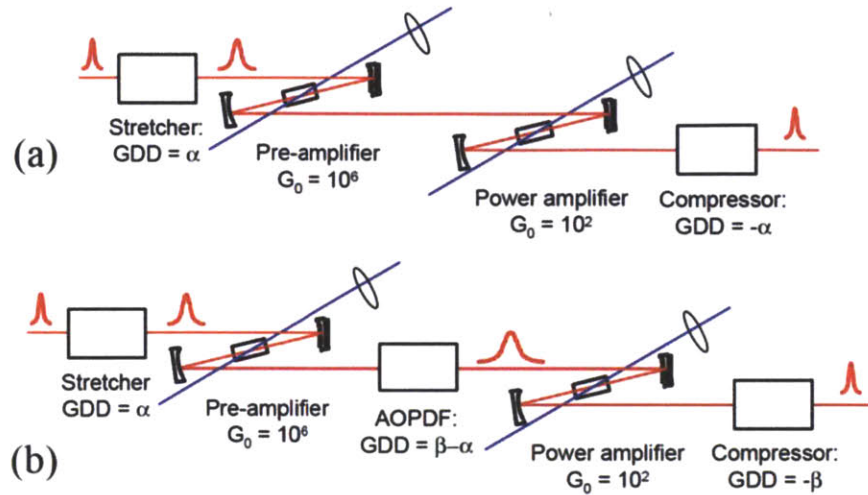
Figure 2.16 Schematics of two-stage OPCPA system designs. In (a), the signal chirp in pre- and power amplifiers must be the same. In (b), a third dispersive element allows independent optimization of $\Delta t_s/\Delta t_p$ at each stage.

2. If, alternatively, the system is designed to maximize amplifier bandwidth, then optimization of the pre-amplifier stage is crucial. Since the gain centroid of the pre-amplifier is considerably narrower than the that of the power amplifier, the pre-amplifier will set a maximum seed chirp. Once the pre-amplifier is optimized for suitably-large bandwidth, $\Delta t_s/\Delta t_p$ will be too small in the power amplification stage, resulting in both a low efficiency and a poor signal-to-noise ratio.

These problems can be avoided by placement of a third dispersive element between pre- and power amplification stages, to allow independent optimization of each stage. A good design strategy is illustrated by Figure 2.16b. First, the stretcher dispersion is chosen to optimize the signal chirp in the pre-amplification stage, $GDD = \alpha$. Second, the compressor dispersion is chosen to optimize the signal chirp in the power amplification stage, $GDD = \beta$. Last, a third dispersive element, placed

between amplification stages, is chosen to compensate for the dispersion mismatch between stretcher and compressor, $GDD = \alpha - \beta$. An acousto-optic programmable dispersive filter (AOPDF) or other variable dispersive device is particularly suitable for this element, since it allows both experimental testing of the optimal chirp for the power amplifier and the ability to adjust for modifications of the dispersion in either the stretcher or compressor.

We note, the empirical formula for the scaling of $\Delta t_s / \Delta t_p$ with G_0 (Eq. 2.12, with $\alpha = 2.1$) depended on the particular characteristics of the amplifier, including the initial pump intensity profile, the initial seed spectrum, and $\Delta k(\omega)$. While it is possible to reproduce the simulations and determination of α for any system, alternatively, one may experimentally determine the appropriate seed chirp for either stage of a multi-stage amplifier and then use Eq. 2.12 to determine the optimum chirp at the other stages.

Finally, for when robustness of signal-to-noise ratio is crucial, we mention the importance of at least a small sacrifice in effective amplifier bandwidth relative to the full phase matching bandwidth of the amplifier by keeping the ratio $\Delta t_s / \Delta t_p$ suitably large. This both allows the elimination of a significant discrepancy between signal and noise gain profiles and ensures that all temporal coordinates of the region of significant gain are seeded (an important consideration when the amplifier is driven into saturation). Since the final signal-to-noise ratio of a multistage amplifier depends on the suppression of noise amplification at each stage, it is important to correctly optimize the signal chirp at each stage.

2.3   NIR and SWIR OPCPAs

In this section, we will introduce two OPCPAs realized in our lab. We follow the guidelines developed in the previous sections to design and build these two OPCPAs. The NIR-OPCPA produces 25-μJ, 9-fs pulses centered at 870 nm and the SWIR-OPCPA produces 25-μJ, 24-fs pulses centered at 2.15 μm.

Figure 2.17 is the block diagram of the two OPCPAs. The Ti:sapphire oscillator (IdestaQE Octavius-85M) is similar to the one described in reference [46]. Pumped with 6W of 532 nm light (Coherent Verdi V6), the oscillator outputs an average power of 200mW with a repetition rate of 85MHz. The optical cavity is set up in an astigmatism-compensated x-folded geometry employing two concave double-chirped mirrors (DCMs) with 75mm radius of curvature. The dispersion of
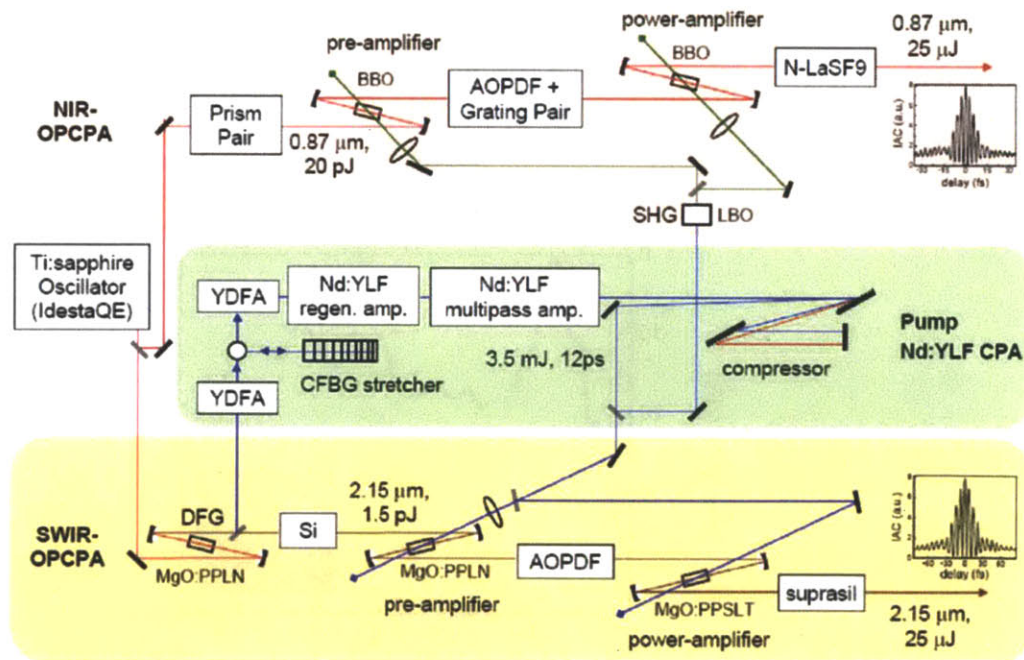

Figure 2.17 Schematics of the Nd:YLF CPA pump, the NIR-OPCPA, and the SWIR-OPCPA. YDFA: Ytterbium-doped fiber amplifier; CFBG: chirped fiber Bragg grating; AOPDF: acousto-optic programmable dispersive filter.

the Ti:sapphire gain crystal and the air within the cavity is precisely compensated by DCM pairs, a BaF_2 plate, and a BaF_2 wedge pair. BaF_2's low ratio of the group-delay dispersion and the third-order dispersion allows the design of octave-spanning DCMs with 99.9% reflectivity from 580nm to 1200nm. Finally, a broadband quarter-wave $ZnSe/MgF_2$ output coupler (OC) that transmits more on the spectral edges than the center helps reshape the output spectrum to achieve a bandwidth of an octave. Figure 2.18 reports the output spectrum of the oscillator, showing the octave is reached at the spectral density of -25dB.

Figure 2.19 shows the all-optical synchronized seed and pump generation scheme. A broadband 10/90 beamsplitter divides the oscillator output into two parts: 10% of the oscillator output is directed to the NIR-OPCPA channel centered around 870-nm while the rest of the output is focused into a 2 mm MgO-doped periodically poled congruent lithium niobate (MgO:PPcLN) crystal with a poling period of 13.1 μm, wherein intrapulse DFG creates 2.15-μm seed pulses for the SWIR-OPCPA
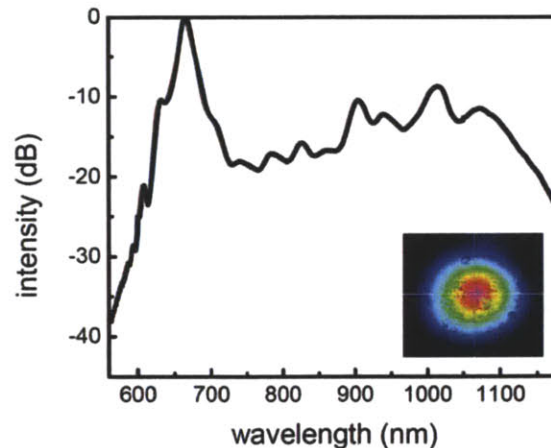

Figure 2.18 The output spectrum of the oscillator. An octave is reached at the spectral density of -25dB. The lower inset is the output beam profile.

channel. Figures 2.20a and 2.20b are the spectrum of the two seeds, both reaching a

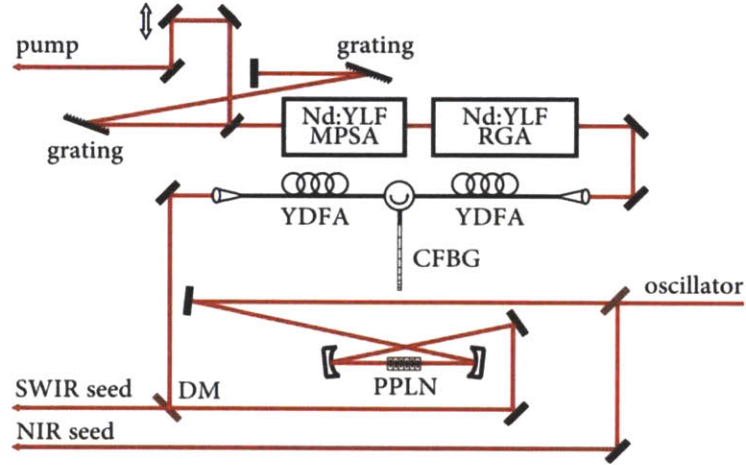bandwidth of more than half an octave (full width at -20dB).

Figure 2.19 Generation of the seed pulses for the OPCPAs and all-optical synchronization.
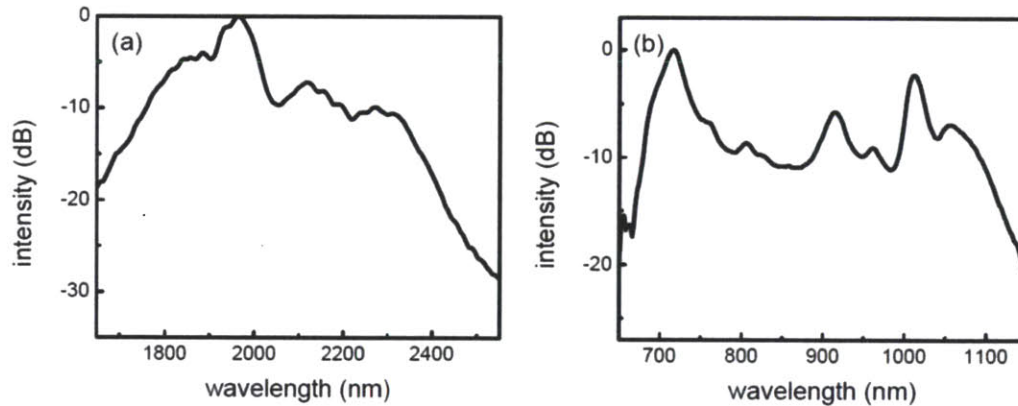
Figure 2.20 (a) The seed spectrum of the SWIR-OPCPA. (b) The seed spectrum of the NIR-OPCPA. Both seeds reach a bandwidth of more than half an octave and cover the phase-matching bandwidth of the corresponding OPCPAs.

After the intrapulse DFG stage, a DM and a 4-nm BPF is used to pick up the

1047nm component for seeding the YDFA/Nd:YLF hybrid CPA, which pumps the

two OPCPAs. To suppress amplified spontaneous emission in the Nd:YLF

regenerative amplifier (RGA), the seed is pre-amplified to 3 pJ in two YDFAs. The

gain of the YDFAs is kept to 10 to avoid parasitic lasing at 1030nm. The Nd:YLF

CPA system consists sequentially of a chirped fiber Bragg grating (CFBG) stretcher,

a Nd:YLF RGA followed by two Nd:YLF multi-pass slab amplifiers (MPSA), and

a diffraction grating compressor. The CFBG has a length of 10 cm, super-Gaussian

apodization and a chirp rate of 440 ps/nm. The grating was inscribed in Nufern

PS1060 photosensitive fiber using a phase-mask scanning technique in a Sagnac

interferometric configuration. The pulse duration after the Nd:YLF RGA is 110 ps

with a bandwidth of 0.25 nm, enough to avoid B-integral-related damage in the

Nd:YLF MPSAs.

Figure 21 shows the schematics of the Nd:YLF RGA (High-Q Laser) and

the Nd:YLF MPSAs (Q-Peak). All Nd:YLF crystals are oriented to operate at the

1047nm emission line, utilizing the high gain quality. In the RGA, the Nd:YLF

crystal is back-coated such that the 1047nm light is reflected while the 798nm

diode pump is transmitted. A quarter waveplate (QWP), a Pockels cell (PC)

operating at $0°$ and $\pi/4$, and a thin-film polarizer (TFP) control the injection and

ejection of the RGA pulses. The total cavity length is 1.5m. To reduce the loss

associated with the thermal lensing, a quasi-CW pumping scheme is employed: the

crystal is pumped for 450μs until the seed is injected. A single-pass small-signal

gain of 2 can be achieved and the RGA output energy is 1.05mJ with a shot-to-shot

r.m.s. energy fluctuation better than 0.5%. The overall RGA gain is more than

90dB and the output bandwidth is reduced to 0.25nm due to the strong gain

narrowing. The RGA output pulse is then further amplified in the two three-pass

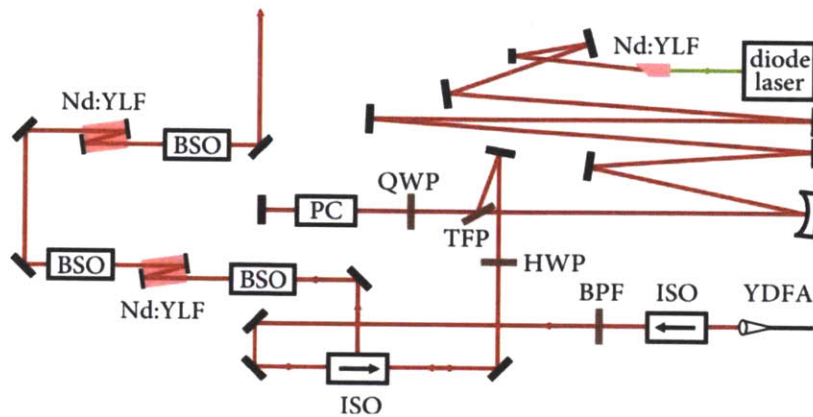Nd:YLF MPSAs. Each Nd:YLF crystal is 28 mm long, 2 mm by 6 mm in aperture,

Figure 2.21 Scheme of the Nd:YLF hybrid chirped pulse amplifier, including a regenerative amplifier (RGA) and two Nd:YLF multi-pass slab amplifiers (MPSAs).

and side pumped with 78 W optical power. Due to the side pumping geometry, the asymmetric thermal lensing introduces astigmatism to the output pulse. A telescope with tilted lenses and cylindrical lenses is thus implemented after each MPSA to correct the astigmatism. Overall, the two Nd:YLF MPSAs offer a gain of 6.3 and an output pulse energy of 5.7 mJ is obtained. The pulse is then compressed using a gold-coated grating pair, where the gratings have a groove density of 1800 lines/mm and a diffraction efficiency of 90%. The separation between the two gratings is set to 2.7 m with multiple bounces off dielectric mirrors to achieve a compact setup. The throughput of the diffraction grating compressor is ~65% and a compressed pulse duration of 12 ps (~1.3x of the transform limit) is measured using a single-shot autocorrelator. A half waveplate and a polarization beamsplitter then divides the pulse into two parts where 1mJ is used to pump the SWIR-OPCPA and 2mJ is first frequency doubled in a 1cm lithium triborate crystal before being used to pump the NIR-OPCPA. The frequency doubling process has a conversion

51

fluorescence suppression are included. While the fine phase management setup enables control and optimization of the synthesized waveform, it inevitably introduces signal loss and thus it is generally better to place it between the pre-amplifier and the power-amplifier for simultaneous optimization of output power and super-fluorescence suppression: If placed before the pre-amplifier, its losses directly reduce the signal-to-noise ratio, which is set by the ratio of seed power to equivalent noise energy in vacuum modes [48]. Placed after the power-amplifier, its losses reduce the output power. An effective spatial filter, created by setting the pump beam width less than a half of the signal beam width and placing the nonlinear crystal a few diffraction lengths away from the signal focus, improves the beam quality and eliminates the phase-matched, super-fluorescence-dominated high-order spatial modes of the signal. If the initial signal-to-noise ratio is particularly low, such as for the SWIR-OPCPA, an additional iris diaphragm is implemented for the same purpose. At the end, a bulk material is used to compress the pulses to their transform limit.

For the SWIR-OPCPA [38], a 30-mm bulk silicon block is used as the Stretcher-1 to stretch the signal to 5 ps. The signal is pre-amplified to 1.5 μJ in a 3-mm MgO:PPcLN with a poling period of 31.0 μm, pumped with 150 μJ pulses. The pre-amplified pulse is further stretched to 9.5 ps by an AOPDF which also serves as a fine phase management setup. Of note, the AOPDF can also shape the output spectrum but care has to be taken to ensure sufficient seed energy for the power-amplifier. The gain medium for the power-amplifier is a 3-mm MgO-doped periodically poled stoichiometric lithium tantalate crystal (MgO:PPsLT) with a

poling period of 31.4 μm, pumped with 750 μJ pulses. The output pulses have 25 μJ energy and can be compressed to nearly transform-limited 24 fs duration in a 300-mm broadband anti-reflection coated Suprasil-300 glass block. For the NIR-OPCPA [23], a Brewster prism pair with 1-m apex-to-apex distance stretches the signal to 5 ps. The signal is pre-amplified to 2 μJ in a double-pass, non-collinear (2.4° pump-signal angle) geometry in a type-I, 5-mm-long BBO crystal cut at θ=24°, and pumped with 250 μJ pulses. The pre-amplified pulse is further stretched to 6.2 ps by a combination of a Treacy grating pair and an AOPDF. The gratings have a groove density of 300 lines/mm and the separation between the two gratings is 82 mm. The Treacy grating pair is included in order to balance the excess high-order dispersion introduced by the Brewster prism pair. Additionally, the CEP drift caused by a Treacy grating pair due to temperature fluctuation is opposite in sign to that of a Brewster prism pair [49] and thus the inclusion of a Treacy grating pair improves the long-term CEP stability. Again the AOPDF also serves as a fine phase management setup here. The gain medium for the power-amplifier is the same as the first OPCPA stage, but pumped with 650 μJ pulses. The output pulses with an energy of 25 μJ are then compressed to 9 fs in a 40-mm Brewster-cut N-LaSF9 glass block.

Figures 23 show the characterization of the two OPCPAs. Both OPCPAs reach bandwidths of more than half an octave (full width at -20dB) and the combined spectrum spans over 1.8 octaves. The OPCPA outputs can be both compressed to within 10% of their transform-limited pulse durations, measured with interferometric autocorrelators (Figures 23c and 23d). Figures 23e to 23h
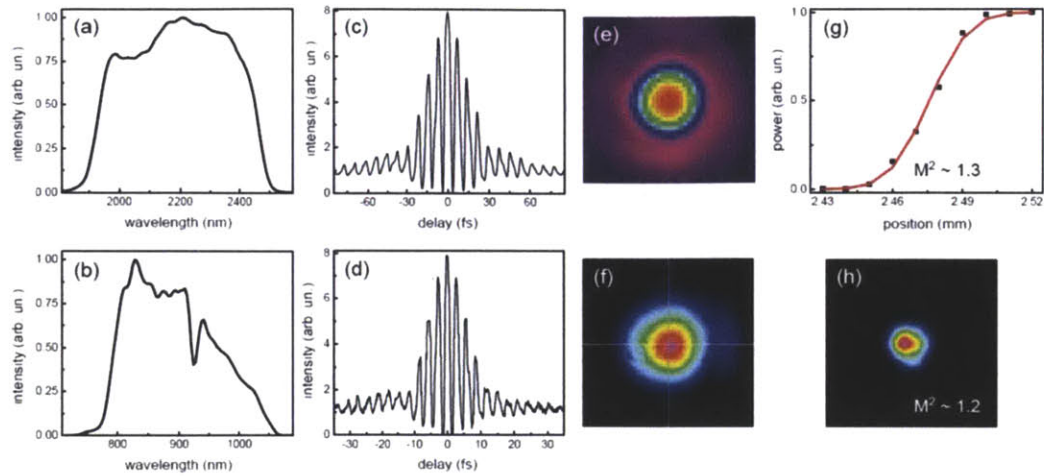
Figure 2.23 (a) The output spectrum of the SWIR-OPCPA. (b) The output spectrum of the NIR-OPCPA. (c) The interferometric autocorrelation trace of the SWIR-OPCPA pulses. (d) The interferometric autocorrelation trace of the NIR-OPCPA pulses. (e) The far-field beam profile of the SWIR-OPCPA. (f) The far-field beam profile of the NIR-OPCPA. (g) The knife-edge measurement of the near-field beam profile of the SWIR-OPCPA, indicating a M^2 value of 1.3. (h) The near-field beam profile of the NIR-OPCPA, indicating a M^2 value of 1.2.

show the near-field and far-field beam profiles, showing clean fundamental Gaussian modes with good M^2 values. M^2 values are calculated by measuring the beam waist and the beam divergence.

2.4   Cryogenically cooled Yb:YAG chirped pulse amplifier

Since the energy scaling of these OPCPA systems at kHz repetition rate is ultimately limited by the power and energy handling of Nd:YLF laser technology, new pump laser technologies based on Yb-doped laser materials are now being rapidly developed. Metzger *et al.* **[50]** developed a 25-mJ ~1-ps Yb:YAG CPA laser at 3 kHz based on thin-disk laser technology to avoid thermal problems. On
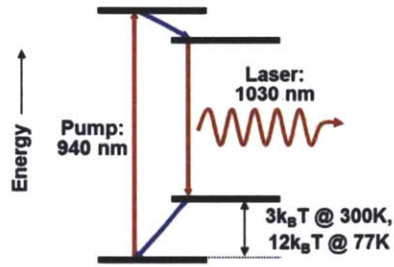
Figure 2.24 The energy level diagram of Yb:YAG.

the other hand, cryogenic solid-state laser technology provides a straightforward way of energy and average power scaling.

Yb:YAG exhibits a number of favorable properties:

1. It has a broad absorption band at 940nm and thus it can be pumped by high-power laser diodes without active spectral control.

2. Its low quantum defect (9%) leads to high conversion efficiency and low thermal load.

3. Its high thermal conductivity (6.6 $Wm^{-1}K^{-1}$ @ 3% Yb doping) reduces the risk of optical damages associated with thermal lensing.

4. A doping level as high as 20% is possible without quenching.

5. Its long upper-state lifetime (~1ms) supports accumulation of substantial population inversion under continuous laser diode pumping.

6. It has a broad emission band at 1030nm and thus it can be used for pico-second pulse amplification.

Unfortunately, Yb:YAG is a quasi-three-level system at room temperature and thus the saturation fluence is rather high ($9J/cm^2$). Figure 2.24 shows the energy level diagram of Yb:YAG. The final state of the lasing transition and the ground state are separated by 612 cm^{-1}, which is only $3k_BT$ at room temperature. With this small of an energy difference, there is a significant thermal population in the final lasing state, leading to quasi-three-level laser operation. At 77 K, however, these two states are separated by $12k_BT$, leading to more efficient four-level laser operation and lower saturation fluence ($2J/cm^2$). Cryogenically cooling thus increases the single-pass gain, which is crucial for stable operation of a RGA without bifurcation and excess timing drifts, and allows efficient energy extraction to take place even at low intra-cavity intensities, which is desirable because to the risk of optical damages is reduced.

Cryogenically cooling also leads to a dramatic improvement of the thermo-optic properties of Yb:YAG [51]. The focal length due to a thermal lensing effect in a cylindrical crystal is given by [51]:

$$f \propto \frac{K}{\frac{dn}{dT} + \alpha Y(n, L)} \qquad Eq.\,2.13$$

where K is the thermal conductivity, α is the thermal expansion coefficient, n is the refractive index, L is the crystal length, and Y is a function describing thermal stress and expansion. In the cryogenically cooled Yb:YAG crystal, the thermal conductivity is improved by a factor of 4, the thermal expansion coefficient is lowered by a factor of 3, and dn/dT is reduced by a factor of 8. Overall, cryogenically cooling make the thermal lensing effect more than an order of magnitude weaker.

Linewidths of energy levels typically narrow as the temperature decreases and thus it is important to check the spectral properties of Yb:YAG at cryogenic temperatures. Figure 2.25 shows the absorption and emission spectra [52], [53]. Despite the fact that there is some sharpening of the absorption spectrum, the spectrum at 77K remains effectively as broad as at room temperature, and is still suitable for diode pumping without active spectral control. The emission bandwidth narrows from 7nm at room temperature to 1.5nm at 77K. Gain narrowing effect will further narrow the amplified bandwidth, $\Delta\lambda_{out}$, which can be estimated by [54]:

$$\Delta\lambda_{out} = \frac{\Delta\lambda_{in}}{\sqrt{1 + lnG\left(\frac{\Delta\lambda_{in}}{\Delta\lambda_{fluo}}\right)^2}} \qquad Eq.\,2.14$$

where G is the gain, $\Delta\lambda_{in}$ is the input bandwidth, and $\Delta\lambda_{fluo}$ is the emission bandwidth. Figure 2.26 plots $\Delta\lambda_{out}$ as a function of the gain G with $\Delta\lambda_{fluo} = 1.5nm$ and $\Delta\lambda_{in} = \frac{\Delta\lambda_{fluo}}{2}$ (red line) or $\Delta\lambda_{fluo}$ (blue line). Even with a gain of 80 dB, the amplified bandwidth is still broader than 0.3nm and supports picosecond pulse amplifications.

Figure 2.27 is a schematic diagram of our high-energy, 14 ps, cryogenic Yb:YAG CPA. It is seeded by the same Ti:sapphire oscillator described in Section 2.3. The stretcher is composed of a chirped volume Bragg grating (CVBG) pair with a chirp rate of ~100 ps/nm per bounce. The spatial chirp of the CVBGs (Ondax, Inc.) has been significantly reduced by stressing the middle of the gratings [55]. After 8 bounces off the CVBGs, we obtained ~560 ps positively chirped pulses with 0.7 nm bandwidth at 1029 nm, as shown in Figures 2.28a and 2.28b.
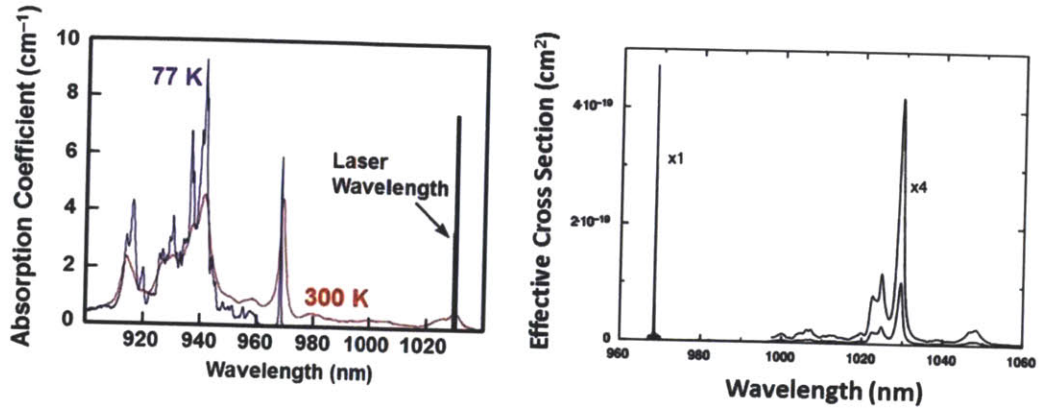
Figure 2.25 (a) The absorption spectrum of Yb:YAG at room temperature and 77K. (b) The emission spectrum of Yb:YAG at 77K.
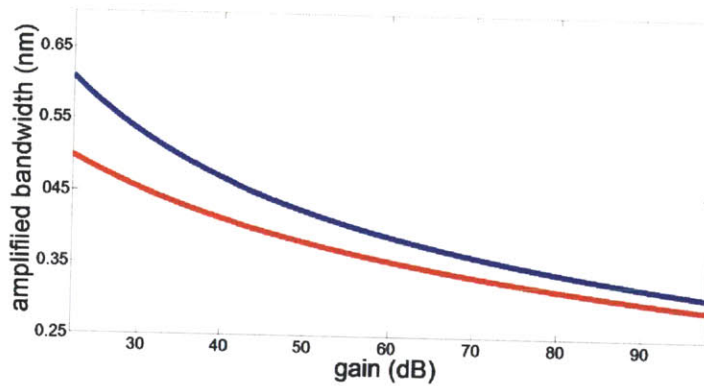

Figure 2.26 Amplified bandwidths as a function of gain with input bandwidths of $\Delta\lambda_{fluo}/2$ (red line) and $\Delta\lambda_{fluo}$ (blue line).

Figure 2.28b was measured using a fast photodiode with a rise time of 27 ps and a sampling oscilloscope. Two YDFAs before and after the CVBG stretcher ensure high enough pulse energy (~100 pJ) for seeding of the cryogenic Yb:YAG RGA. Even though the output energy of the RGA can be higher than 10 mJ, it was fixed to ~5 mJ at 1 kHz for long-term stable operation without optical damage, where the pump power was 45 W from a fiber-coupled cw laser diode at 940 nm. The spectral bandwidth was reduced to 0.24 nm, corresponding to ~190 ps pulse duration after the RGA. The beam from the RGA was delivered to a double-pass cryogenic
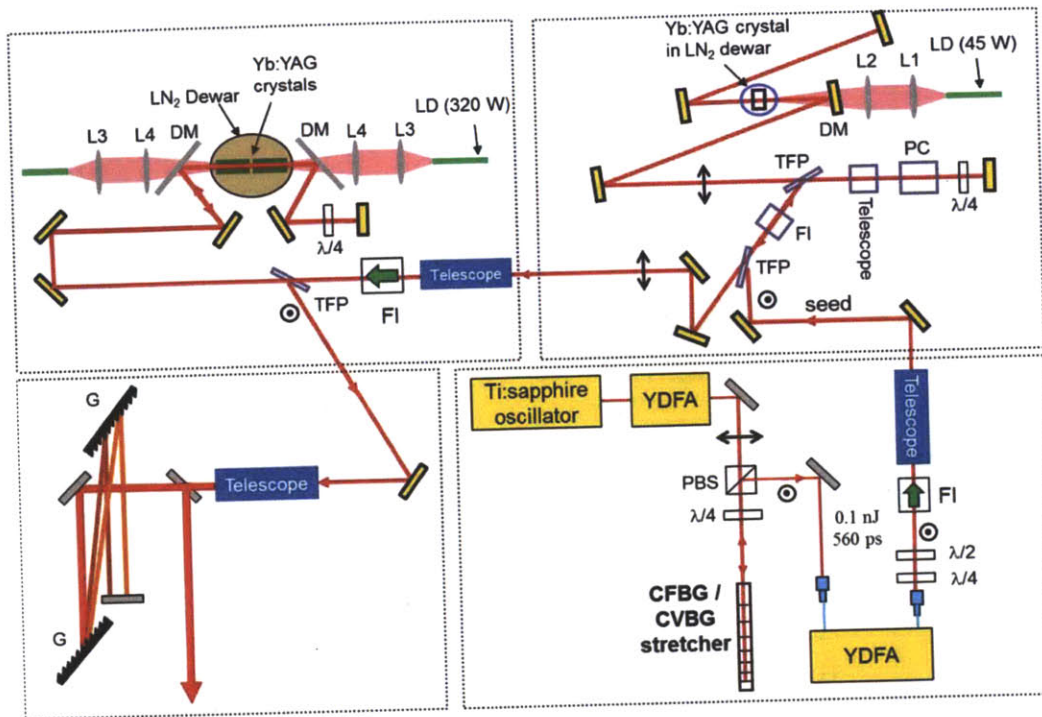
Figure 2.27 A schematic diagram of our high-energy, 14 ps, cryogenic Yb:YAG CPA.

Yb:YAG amplifier with two crystals in an evacuated chamber. We limited the maximum energy from this amplifier to 20 mJ at 1 kHz with a relatively large pump beam size (~3.6 mm $1/e^2$ diameter) also for damage-free long-term operation, as in the RGA. The gain guiding effect along with the thermal lensing reduced the beam size at each pass, leading to optical damage at high-energy operation. The RGA output beam is expanded using a 1:2 telescope and set to be diverging to partially compensate for this gain guiding effect at the cost of efficiency such that the beam size of the unamplified pulse after the double-pass amplifier is ~4.8 mm in diameter. As the maximum pump power approaches 320 W for 20 mJ (20 W) of amplified energy (power), the beam size decreases to ~3.1 mm in diameter. The accumulated nonlinear phase through the amplifier chain is
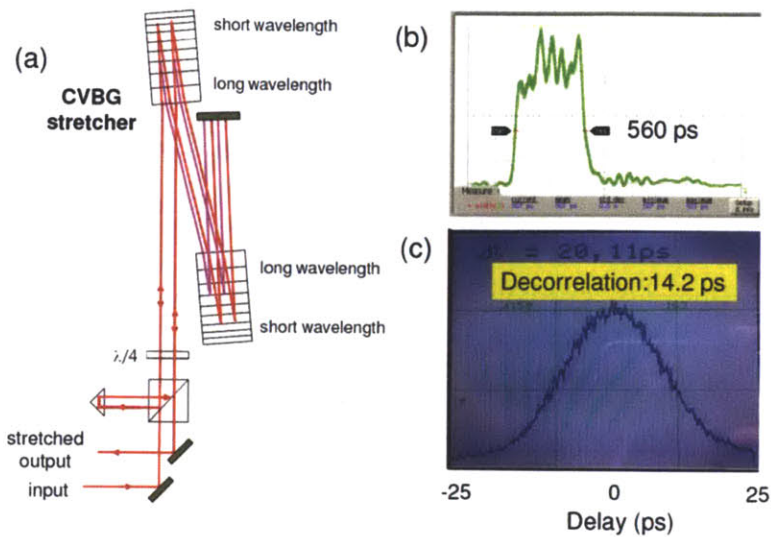
Figure 2.28 Stretching and compression of picoseconds pulses: (a) 8-pass CVBG stretcher, (b) positively chirped, stretched pulse shape with ~560 ps over ~0.7 nm of spectral bandwidth, and (c) autocorrelation trace of compressed 14.2-ps pulses with 0.25 nm of spectral bandwidth after an MLD grating compressor.

estimated to be 0.8 rad. The pulse is compressed using a multi-layer dielectric (MLD) grating pair, where the gratings have a groove density of 1752 lines/mm and a diffraction efficiency of 95%. The separation between two MLD gratings was set to ~2.75 m with multiple bounces off dielectric mirrors to achieve a compact setup. A throughput efficiency of 75% was achieved and a compressed pulse duration of 14.2 ps was measured using a picosecond autocorrelator, as shown in Figure 2.28c. The transform-limited pulse duration supported by the output spectral bandwidth of 0.24 nm is 7.5 ps. The pedestal in the autocorrelation trace goes to zero at around +/−40 ps and the energy shed to the pedestal is estimated to be ~10%. After all the beam delivery optics, the maximum available energy for pumping the OPCPAs is 13 mJ.

Both SPM and the group delay ripple (GDR) in the CVBGs contribute to the formation of the pedestal, limiting better compression. To improve the pulse compression quality, a simple stand-alone stretcher which is free of GDR and can provide a chirp rate of >1ns/nm is necessary. By careful optimization of the fabrication process, our collaborators in Sydney successfully reduce the peak-to-peak GDR in the CFBGs from 120 ps to 42 ps (see Figure 2.29). Such CFBGs will serve as the stretcher for our next-generation cryogenically cooled Yb:YAG CPA.
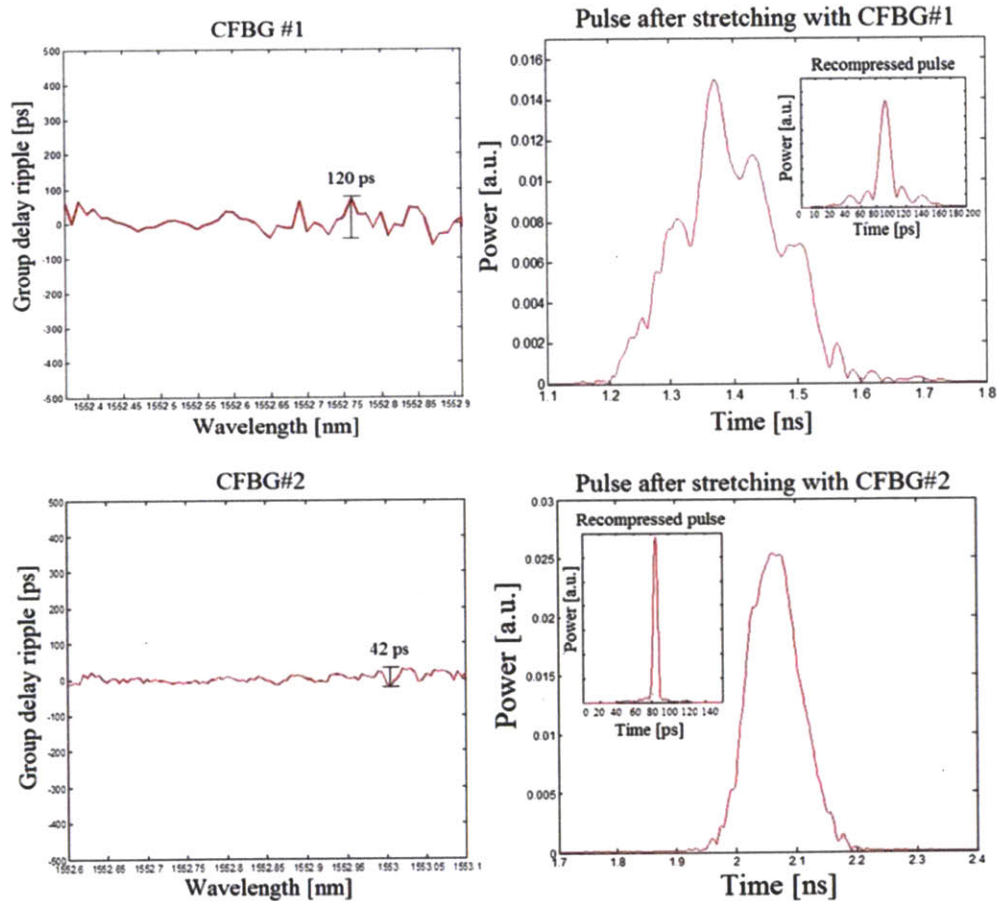

Figure 2.29 The old CFBG (#1) exhibits 120ps (peak-to-peak) GD ripples which leads to a substantial distortion of the recompressed Gaussian pulse. The new CFBG (#2) has a 3 times lower GD ripples and such CFBGs will serve as the stretcher for our next-generation cryogenically cooled Yb:YAG CPA.

2.5 Upgrade SWIR-OPCPA and long-wavelength driven HHG

In this section, the recent progress on the energy scaling of the SWIR OPCPA system is reported. We maintained a lower energy Nd:YLF pump laser for the first two OPCPA stages as pre-amplifiers to minimize the modification of the former system, which operates stably and is already optimized for super-fluorescence suppression. For power amplification, we added an additional OPCPA stage and pumped it with the novel high-energy cryogenically cooled Yb:YAG CPA described in the previous section.
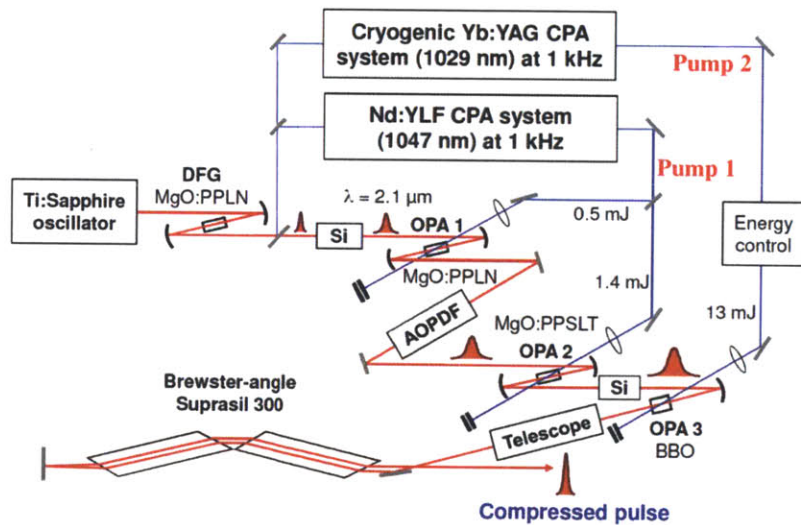
Figure 2.30 Optical layout of the broadband CEP-stable 2.1-μm 3-stage upgraded SWIR-OPCPA system. Fine dispersion control is used for efficient amplification with low superfluorescence. Pulse durations are ~5 ps before the first stage, ~9 ps before the second stage, ~14 ps before the third stage, and 32 fs after the compressor.

The optical layout of the OPCPA system pumped by two CPA lasers is illustrated in Figure 2.30. The majority of the OPCPA setup of the first two stages is the same as described in Section 2.3, but the following modifications have been

Figure 2.31 Calculated 3-stage upgraded SWIR-OPCPA output spectra. Red line is the spectrum obtained by integrating over the whole beam. Blue line is the spectrum obtained by integrating over the center 500μm part of the beam.

made: (i) The pump beam sizes at both stages are increased so that the pump energies are higher while the pump intensities remain (if not lower). Thus, the output energy remains at 25μJ with better signal-to-noise ratio because the OPCPA is less saturated; (ii) The pulse duration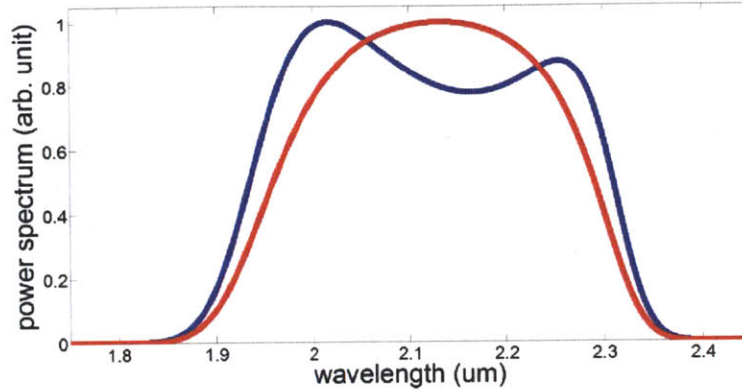 is further stretched to ~14 ps after the second stage by an additional 30-mm silicon block to optimize its match to the pump pulse duration of the Yb:YAG CPA.

Aiming for multi-mJ amplification, the periodically poled crystals are not suitable in the third stage due to the limited aperture size available to us. Thus, we used a 5-mm-long type-I BBO crystal ($\theta = 21.4°$) instead of MgO:PPSLT at the cost of phase-matching bandwidth. Our calculation (Figure 2.31) showed that the supported phase-matching bandwidth of the 5-mm-long BBO crystal is 400 nm at 40 GW/cm^2 pump intensity with a maximum conversion efficiency of 12% for Gaussian beams and pulses in space and time, respectively.

The third stage pump intensity was ~40 GW/cm^2 at 13 mJ of energy. The angle between the pump and the seed was minimized to <2° so as to separate the
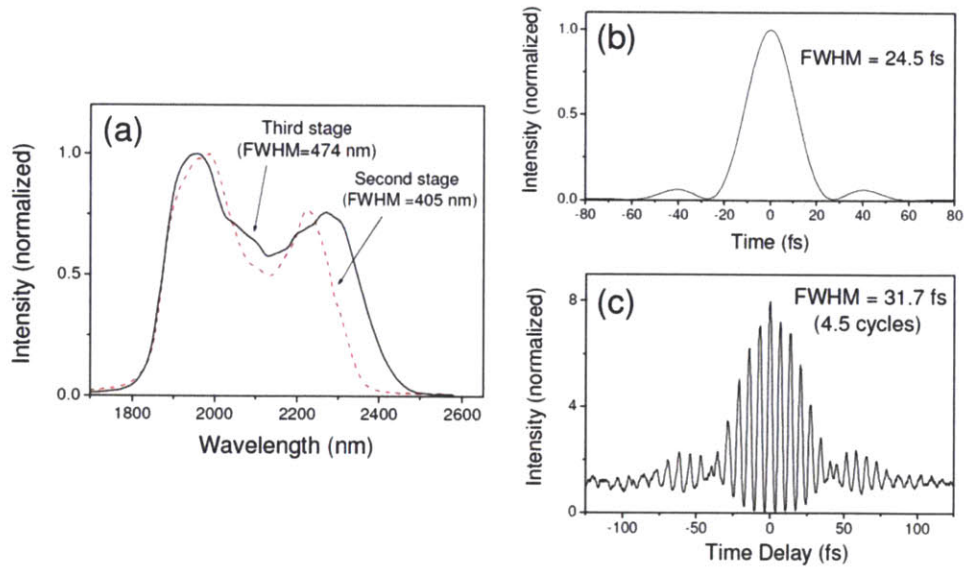
Figure 2.32 Amplified spectra from the second and third stages (a), the transform-limited pulse duration of 3.5 optical cycles supported by the third-stage spectrum, (b) and the measured IAC trace after compression to 4.5 optical cycles (c).

output signal from the pump in a manageable distance while maximizing the phase matching bandwidth. After optimization of temporal and spatial overlaps and incidence angle of the pump beam into the BBO crystal, we obtained a maximum energy of 0.85 mJ, indicating an internal conversion efficiency of 7.5%. The amplified spectrum from the third OPCPA stage is represented as the solid line in Figure 2.32a. The spectral bandwidth of 474 nm FWHM centered at 2.1 μm supports a transform-limited pulse duration of 24.5 fs or 3.5 optical cycles, as shown in Figure 2.32b. The pulse compression was achieved using two Brewster-angle Suprasil 300 blocks with a total path length of 620 mm. We finely adjusted the AOPDF to minimize the pulse duration and suppress the pedestal while monitoring interferometric autocorrelation traces. Figure 2.32c shows the compressed pulse with a duration of 31.7 fs or 4.5 optical cycles, which is 1.3 times

longer than the transform-limited value. The throughput efficiency of the compressor is ~95% with the silver retro-reflector being the main cause of energy loss.

We characterized the stability and noise characteristics of the amplified pulses to identify the energy portion occupied by the amplified super-fluorescence. First, the shot-to-shot energy fluctuation of the amplified 2.1-μm pulses is measured to be 4.1% (r.m.s.). This is about 3 times higher than the measured 1.5% for the former 0.2-mJ system in reference [38]. The stability degradation naturally comes along with the increased super-fluorescence noise in higher-gain amplification. In addition, the stability of the pump laser system is slightly worse because the Nd:YLF RGA is operating slightly under saturation and the overall complexity of using the two pump lasers is also higher. Second, the shot-to-shot intensity fluctuations, calculated by halving the corresponding intensity fluctuations of low-conversion SHG of the 2.1-μm pulses, are 3.9% (r.m.s.). Third, the shot-to-shot fluctuations of the unseeded super-fluorescence are ~23%. Based on the three stability parameters given above, we can estimate the SF noise to be ~9% from a simple statistical treatment (see Appendix). This means that the signal energy in the main pulse is ~0.77 mJ out of 0.85 mJ. Compared to the parameters in the similar work by Gu *et al.* [56], i.e., 9% energy fluctuation and 20% super-fluorescence noise with 0.74 mJ of compressed pulse energy, our system demonstrates twice better noise performance with a slightly higher compressed pulse energy, but with a longer pulse duration due to the limited phase matching bandwidth of BBO (vs. PPLN) in the last stage. There is another indication proving that this comparison is

reasonable. The energy ratio between the amplified pulses and unseeded amplified super-fluorescence was ~2.5:1 or better in our case, whereas it was only ~1.1:1 in the work of Gu *et al.* [56]. The smoother amplified spectra of our OPCPA system is also an indirect indication of the lower super-fluorescence noise.

The ultimate goal of this OPCPA development is to achieve high-flux HHG in the water-window region at kHz repetition rates. As a first step to show the feasibility of achieving this goal, we started HHG experiments in Xe, a heavy noble gas with a low saturation intensity of just above 10^{14} W/cm^2. Even though He and Ne are more suitable for HHG with high photon energy, they have relatively high saturation intensity and require a high pressure of ~10 bars at the interaction region [57]. Since this high pressure is not yet available in our current HHG setup based on a pulsed gas jet operating at kHz repetition rates, Xe is an appropriate gas to start with.

The 2.1-μm OPCPA output was delivered into our HHG vacuum chamber and focused onto the gas jet using an f = 200 mm CaF$_2$ lens. The energy and focal spot were controlled together using an iris before the vacuum chamber. The HHG signal was first detected with an Al-coated XUV photodiode (AXUV100) after another Al filter with 500 nm of thickness allowing ~20% of transmission over the Al transmission window (20−70 eV). The photodiode signal was magnified using a low-noise electronic amplifier to significantly improve the detection sensitivity because the HHG efficiency was expected to be about 2 orders-of-magnitude lower than that driven by 800-nm pulses according to the wavelength scaling. The strongest HHG signal was observed at the peak intensity of (1-2)x10^{14} W/cm^2 at
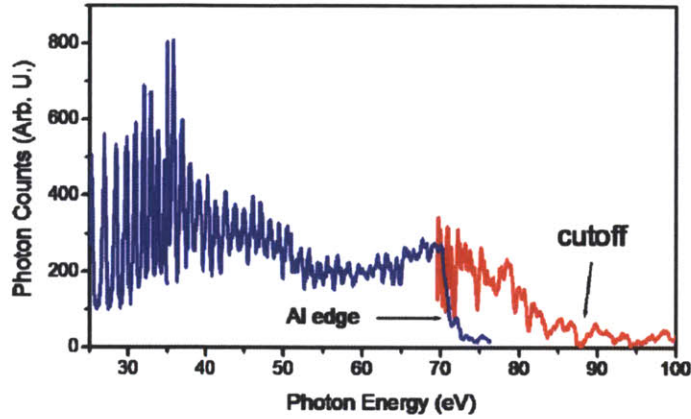
Figure 2.33 HHG spectrum driven by the 3-stage upgraded SWIR-OPCPA using a Xe gas jet. The blue line is measured with an Al filter showing the Al edge at ~70 eV while the red line is measured with a Zr filter showing the cutoff at >85 eV.

~200 mbar of Xe. Since the HHG signal level monotonically increased with pressure, we used the maximum pressure available at the pressure regulator, indicating that the HHG efficiency was limited by the gas pressure. The backing pressure was about 2 bars in this experiment.

After confirming the generation of XUV photons in the Al transmission window, we measured the spectrum using our XUV spectrometer [58] with Al and Zr filters, where the thickness of the Zr filter was 400 nm. Figure 2.33 clearly shows the high-order harmonics up to >85 eV (>149th harmonic, <14 nm), where the Al edge at 70 eV is well identified. The cutoff extension to ~85 eV in Xe is already significant, compared to HHG in Xe driven by our 35-fs, 800-nm driver which is ~35 eV. The achieved cutoff energy is not high enough to satisfy the λ^2 scaling considering the ionization potential of Xe, 12.1 eV, but the phase matching cutoff, scaled with $\lambda^{1.6-1.7}$ [59], for our experimental conditions is in fact calculated to be ~94 eV, indicating near phase-matched HHG in our experiment.

The HHG efficiency per harmonic is estimated to be $\sim 10^{-10}$, which can be improved with higher pressure. However, this efficiency is already consistent with the wavelength scaling of the HHG efficiency starting from 10^{-7}–10^{-8} at 90 eV with an 800-nm driver in Ne or He [58]. Further scaling of photon energy towards the water window region at a kHz repetition rate will be possible with a high-pressure gas jet or a gas cell filled with He or Ne, as demonstrated recently with a 10-Hz OPA system [60]. Our result shows the feasibility of further scaling of photon energy and flux using a broadband CEP-stable kHz OPCPA system as a next-generation source for high-field physics and atto-second science.

2.6   Conformal profile theory for performance scaling

In this section, we use the analytical tools from Section 2.1 to extend conformal profile theory [32], [33] to broadband OPCPA, in which we seek to select time-varying pump, seed, and wave-vector mismatch profiles that allow maximal depletion of the pump. We show that in OPCPA, optimization by use of conformal profiles can significantly boost the bandwidth, conversion efficiency, and the efficiency-bandwidth product (EBP) of an amplifier, thus extending its performance for a wide range of applications.

First let us revisit Eq. 2.3. Close inspection reveals that L_{max}, the crystal length required to reach the maximum possible conversion, is not constant but rather presents an implicit time dependence on three variables: $I_{p0}(t)$, $I_{s0}(t)$, and $\Delta k(t)$. Indeed, for the vast majority of OPCPA systems that do not implement pulse shaping, the resulting variation in $L_{max}(t)$ is great enough that at a chosen

69

crystal length, close to full conversion of pump to signal and idler will occur only across a narrow temporal region. This is one of the main impediments to achieving good overall conversion efficiency. Furthermore, because the signal spectrum is dispersed in time, the non-uniform amplification in the time domain acts as a spectral filter, reducing the amplifier bandwidth.

To illustrate this observation, Figure 2.34 depicts a state-of-the-art type broadband OPCPA stage: amplification of a broadband 1.6 μm chirped seed pulse by a narrowband 0.8 μm pump pulse in a BBO crystal. Because of the degenerate configuration (i.e., signal and idler frequencies are equal) that makes signal and idler group velocities equal by default in a type I collinear geometry, and because BBO has low group-velocity dispersion at 1.6 μm, the phase-matching bandwidth is extremely broad [61]. In this example, it extends from 1.40 to 1.87 μm (1/e full width, corresponding to 53.9 THz) for a 5.0mm long crystal and 13.1GW/cm^2 peak pump intensity. The pump pulse is Gaussian, typical of a laser amplifier, and we choose a relatively flat seed spectrum covering 75 THz (1.33 to 2.00 μm at 1/e full width). The profile of the seed spectrum is transferred exactly to the temporal profile through a strong linear chirp, and the seed and pump pulses both have 12 ps duration (1/e half-width). These long durations ensure that dispersive propagation effects are negligible. Thus, we may calculate amplification of the signal and idler pulses, $I_s(t,z) + I_i(t,z)$, using Eqs. 2.2. The time-varying wave-vector mismatch is translated from $\Delta k(\omega)$ by means of the chirp, $t = (24ps)(\omega - \omega_s)/(2\pi \cdot 75THz)$, and $\Delta k(\omega)$ is calculated from the Sellmeier equations for BBO [62].
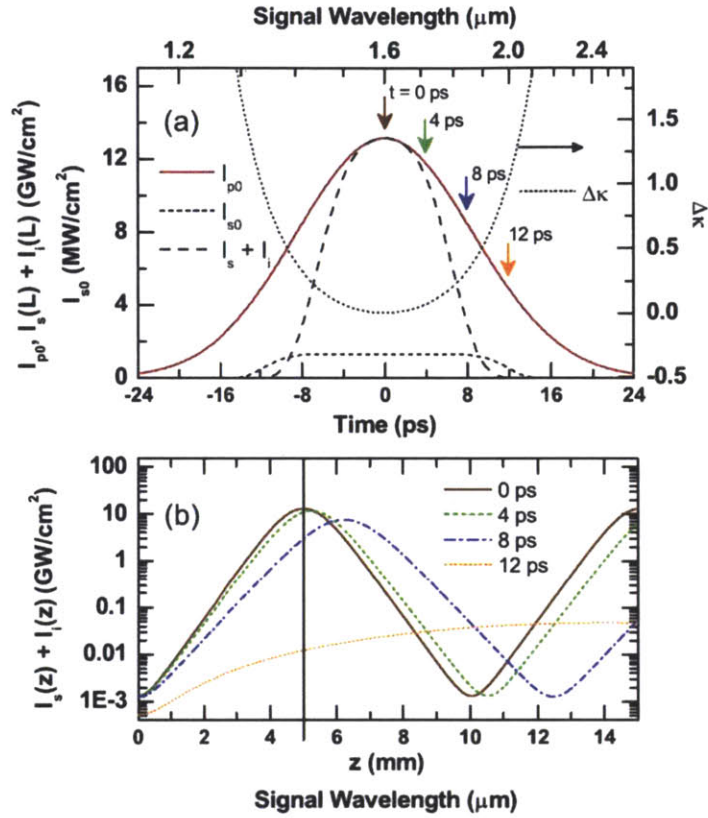
Figure 2.34 (a) Signal plus idler intensity after amplification in BBO. (b) Signal plus idler intensity plotted as a function of propagation distance for temporal coordinates t = 0ps, 4ps, 8ps, and 12ps. These curves correspond to the temporal coordinates indicated by arrows in (a). The vertical bar indicates the crystal length, L = $L_{max}(0)$, corresponding to (a).

Figure 2.34a plots $I_{p0}(t)$, $I_{s0}(t)$, $\Delta k(t)$, and $I_s(t, L) + I_i(t, L)$. Because the seed spectrum covers 1.4× the full phase-matching bandwidth of the amplifier, the variation in $\Delta \kappa(t)$ is significant, ranging from 0 to 1.05 over the wavelength range 1.6 to 2.0 μm. Although full conversion occurs at $t = 0$, lower pump intensity and increasing $\Delta \kappa$ for $|t| > 0$ result in lower conversion and thus the total conversion efficiency is limited 60%. The observed temporal gain narrowing also results in spectral gain narrowing, reducing the amplified bandwidth to $2\pi \cdot 43.9 THz$ (1/e

71

full width), or 59% of the seed bandwidth and 81% of the phase-matching bandwidth.

Figure 2.34b shows the evolution of the signal plus idler intensity as a function of longitudinal position in the amplifier crystal, z, for several values of t, and illustrates a large variation in the position of the first peak of amplification, $L_{max}(t)$. While the difference between $L_{max}(t = 0)$ and $L_{max}(t = 4ps)$ is not great, the peaks of the amplification curves for $t = 8ps$ and $12ps$ are significantly extended in z, because the gain is slowed both by the weaker pump intensity and the higher $\Delta\kappa$. Variation in $I_{p0}(t)/I_{s0}(t)$ also contributes to the variation in $L_{max}(t)$ because the amount of amplication necessary for full conversion (i.e., the total gain) varies. Another effect contributes to the suboptimal conversion efficiency: at $t = 12ps$, the maximum signal plus idler intensity, I'_{p0} (corresponding to the peak of each curve), is a small fraction of I_{p0} because $\Delta\kappa$ is large.

The underlying principle in the use of conformal profiles is to maximize conversion efficiency for all transverse coordinates at a common propagation coordinate in the nonlinear crystal [32], [33]. In the framework of this analysis, this principle requires setting $L_{max}(t)$ constant, thus allowing the maximum conversion of pump to signal and idler, for all values of t, to occur at the same propagation length. In OPCPA, we can make $L_{max}(t)$ uniform through a suitably chosen combination of $I_{p0}(t)$, $I_{s0}(t)$, and $\Delta k(t)$ profiles that are set through the choice of laser parameters and amplification geometry. The answer is determined analytically. For example, choosing two of these three system variables as given, the conformal choice of the third can be found by solving for roots of Eq. 2.3 with a suitable

choice of the crystal length replacing the left-hand side of the equation. This chosen crystal length will be L_{max} for all points in time.

Figure 2.35 illustrates the technique. Keeping all other parameters of Figure 2.34 the same, including $I_{s0}(t)$ and $\Delta k(t)$, we replace the Gaussian pump pulse profile with the conformal $I_{p0}(t)$, found by setting $L = L_{max}(t = 0)$ and solving Eq. 2.3. Shown in Figure 2.35a, $I_{p0}(t)$ has a flattop shape with enhanced edges where the higher pump intensity compensates for the large wave-vector mismatch at large $|t|$. This pump profile has two distinct advantages, illustrated by Figure 2.35b. First, the conversion maxima now line up for all values of t. Second, the increase in I_{p0} at large $|t|$, thus increasing Γ, reduces $\Delta\kappa$ to 0.5 at the edges of the signal bandwidth. This ensures that ϵ_{max} is not much smaller than unity. As a result, the total conversion efficiency is 91%, and because temporal gain narrowing is eliminated, the amplified bandwidth is $2\pi \cdot 76.1 THz$ (1/e full width), or 101% of the seed bandwidth and 141% of the phase-matching bandwidth. Compared to the best result using a Gaussian pump, the efficiency and bandwidth have increased by factors of 1.4 and 1.6, respectively, corresponding to a 2.2× increase in the EBP. Note, for a conformal profile arrangement, the total conversion efficiency simplifies to

$$\eta = \int dt \frac{I'_{p0}(t)}{I_{p0}} = \int dt \cdot \epsilon_{max}(t) \qquad Eq.\,2.16$$

i.e., the maximum conversion possible given $I'_{p0}(t)$.

In the following paragraphs, we investigate the use of conformal profiles of a variety of types and in a variety of settings, analyzing for optimization of
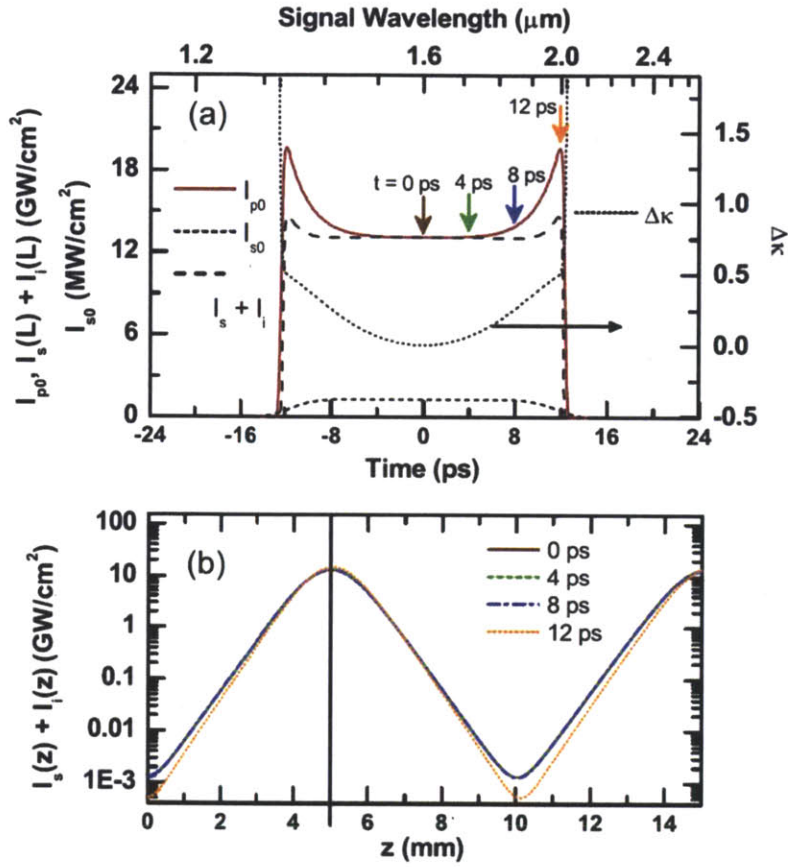
Figure 2.35 (a) Same as Figure 2.34a, but with the Gaussian pump pulse replaced by the conformal pump profile. (b) $I_s(z) + I_i(z)$ for various temporal coordinates corresponding to (a). $L_{max}(t)$ is now uniform.

conversion efficiency and amplifier bandwidth, as well as practical issues such as design tolerances.

Finding a conformal pump profile, given $I_{s0}(t)$ and $\Delta k(t)$, assumes that a root to the master equation

$$L - K(\gamma)\sqrt{\frac{I_{p0}}{I'_{p0}}\frac{\gamma}{\Gamma}} = 0 \qquad\qquad Eq.\,2.17$$

exists for every choice of t in the relevant range. Figure 2.36 plots $I_s(z) + I_i(z)$ for several values of I_{p0}, for a choice of I_{s0}, $\Delta k(t)$, and L for which a root to Eq. 2.17

does exist. There are in fact two roots: one for I_{p0} corresponding to $\Delta\kappa < 1$ and one

at a smaller value of I_{p0} corresponding to $\Delta\kappa > 1$. At these values of I_{p0}, $L = L_{max}$.

We are interested in the larger root, which corresponds to $\Delta\kappa < 1$ and therefore has

a usefully large peak value of I'_{p0}. Determination of this root requires solution of Eq.

2.17 using a root solver with access to a table of values of $K(\gamma)$, as well as an

appropriate choice of lower and upper bounds. Observing the properties of Figure

2.36, $I_{p0}(\Delta\kappa = 1)$ makes a suitable lower bound.

As a practical analysis of the conformal profile technique, we compare and

contrast three pump profile types, shown in Figure 2.37. To represent the typical

bell-shaped pump laser pulse, we analyze Gaussian pump profiles of form $I_{p0}(t) =$

$I_{p0G}(t) \equiv I_{p0}(0)exp[-(t/\tau_0)^2]$ [Figures 2.37a and 2.37b]. Many OPCPA designs

have employed pump pulse shaping to generate flattop pulses [35–37], on the
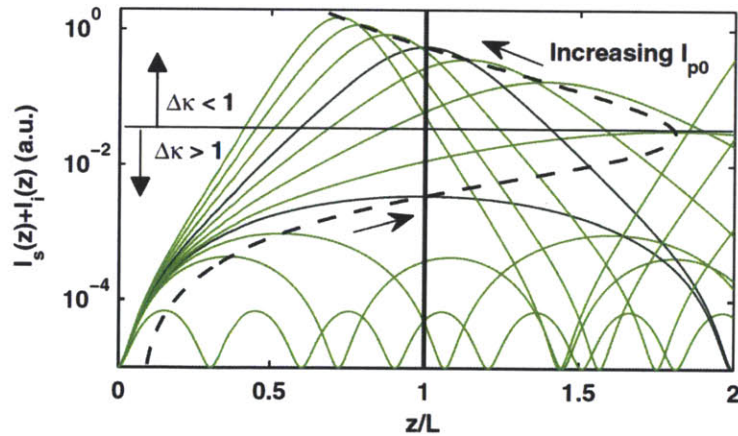
Figure 2.36 (Solid curves) Signal plus idler intensity versus crystal length for varying initial pump intensities. The black curves indicate the amplification curves that peak at the desired crystal length, $i.e.$, $L = L_{max}$. There are two such curves. The upper curve corresponds to the desired conformal value of I_{p0}, which maximizes $I_s + I_i$ at $z = L$, and for which $\Delta\kappa < 1$. (Dashed curve) Locus of points I'_{p0} [peak value of $I_s(z) + I_i(z)$] versus L_{max} [length at which $I_s(z) + I_i(z)$ peaks]. The curve folds at a value of I_{p0} corresponding to $\Delta\kappa \simeq 1.0$.

principle of flattening the nonlinear drive over the temporal profile. We analyze these as high-order super-Gaussians: $I_{p0}(t) = I_{p0F}(t) \equiv I_{p0}(0)exp[-(t/\tau_0)^{20}]$ [Figures 2.37c and 2.37d]. Finally, conformal profiles, $I_{p0}(t) = I_{p0C}(t)$, will be found by means of Eq. 2.17, setting $L = L_{max}(0)$. These profiles are given rounded edges of super-Gaussian form, such that their 1/e half-width has duration τ_0 [e.g., Figures 2.37e and 2.37f]. Note, we use normalized units for this generic analysis, and in all cases, we set $I_{p0}(0) = 1$ and $I_{p0}(0)/I_{s0}(0) = 10^3$. We analyze a roughly flat-top seed pulse shape with only slight variation over the duration of the pump pulse, $I_{s0}(t) = I_{s0}(0)exp[-(t/\tau_0)^8]$. In our performance study, we vary $\Delta k(t)$ to encompass a variety of seed bandwidths and use a linear signal chirp. Note, while the Gaussian and flat-top profiles always take the same form, the conformal profile shape varies according to the solution of Eq. 2.17 given $\Delta k(t)$, as seen in Figures 2.37e and 2.37f, which have different seed bandwidth and chirp.

Since obtaining maximum bandwidth is a typical principle in the design of state-of-the-art OPCPA for ultrafast science, we will in all following examples consider only the group-velocity matched OPCPA. For simplicity, we consider a purely linear signal chirp (although the analysis is easily performed when it includes the typical quadratic and cubic deviations from linear chirp imparted by a grating or prism stretcher), with phase matched signal frequency aligned to $t = 0$. The chirp, $t(\omega) = \tau_0/\delta\omega_s \cdot (\omega - \omega_s)$, allows us to define a temporally varying wave-vector mismatch. In this analysis, we keep the seed duration, τ_0, fixed but vary the seed bandwidth, $\delta\omega_s$, resulting in a different chirp and $\Delta k(t)$ in each case. The phase mismatch can be expressed as $\Delta k(t) = \delta\omega_s^2 \left(\frac{\partial^2 k_s}{\partial \omega^2}\Big|_{\omega_s} + \frac{\partial^2 k_i}{\partial \omega^2}\Big|_{\omega_i} \right)/\tau_0^2 \cdot t^2$.
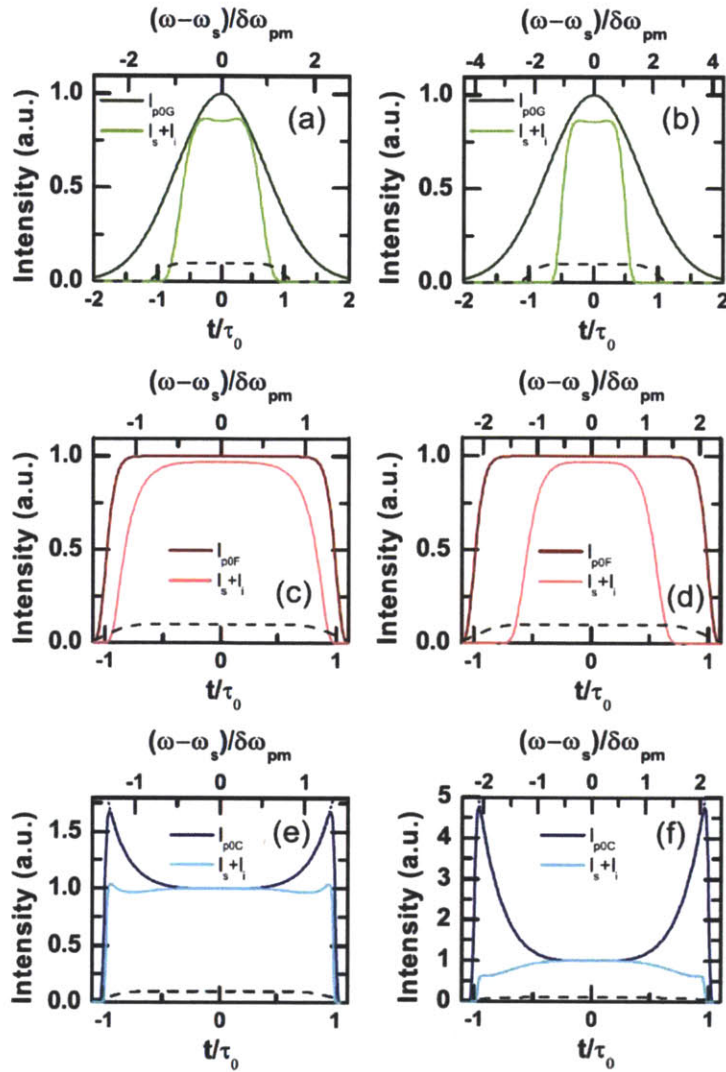
Figure 2.37 (Dark solid curves) (a) and (b) Gaussian, (c) and (d) flattop, and (e) and (f) conformal pump intensity profiles, respectively. In the left column, (a), (c), and (e) have a seed bandwidth $\delta\omega_s = 1.4\delta\omega_{pm}$, and thus share the same $\Delta k(t)$. In the right column, (b), (d), and (f) have a seed bandwidth $\delta\omega_s = 2.2\delta\omega_{pm}$, and also share the same $\Delta k(t)$. The larger seed bandwidth in (f) versus (e) requires taller $I_{p0C}(t)$ wings to compensate for the larger Δk, and thus the corresponding pump profiles have different shapes. All cases share the same seed profile, I_{s0} (dashed curve), plotted here on a scale $100\times$ higher than I_{p0}.

Figure 2.38 compares the performance of the pump profile types outlined above as a function of seed bandwidth. Here, it is useful to normalize the seed bandwidth to the traditionally defined phase-matching bandwidth, $\delta\omega_{pm}$, defined

by $\Delta k(\delta\omega_{pm}) = 2\sqrt{\Gamma/L}$, and where we choose Γ corresponding to $I_{p0}(0) = 1$ and $L = L_{max}(0)$. We compare efficiency, amplified signal bandwidth determined by the standard deviation at crystal length L, and EBP, $\eta\Delta\omega$, a measure of the maximum peak power obtainable from the amplified signal pulse. The following trends are noticeable. Across all profile types, as seed bandwidth is increased, efficiency drops and amplified bandwidth increases. Thus, there is a $\eta\Delta\omega$ maximum for each profile type. Compared to conformal profiles, Gaussian profiles have significantly lower conversion efficiency and flat-top profiles have slightly lower conversion efficiency. However, while conformal profile amplified bandwidths increase with seed bandwidth at a nearly steady rate, flat-top profile bandwidths are capped at a maximum and Gaussian profiles slowly approach the same maximum. This maximum is set by the phase matching bandwidth of the amplifier. As a result, the conformal profile maximum EBP is 107% greater than the Gaussian, and 30% greater than the flattop.

Figure 2.37 sheds light on these performance trends. Gaussian profiles [Figures 2.37a and 2.37b] result in poor efficiency and bandwidth, because of the non-uniformity in $L_{max}(t)$ that is caused by non-uniformities in both $I_{p0}(t)$ and $\Delta k(t)$. These cause temporal narrowing and spectral clipping. Flat-top pulses [Figures 2.37c and 2.37d] impart no temporal narrowing, and thus provide better efficiency and bandwidth than the Gaussian case. However, the varying $\Delta k(t)$ still results in a varying $L_{max}(t)$ and $I_s(t) + I_i(t)$. In other words, spectral narrowing because of $\Delta k(\omega)$ results in temporal narrowing. Note that in Figures 2.37c and 2.37d there are different degrees of temporal narrowing, but nearly the same
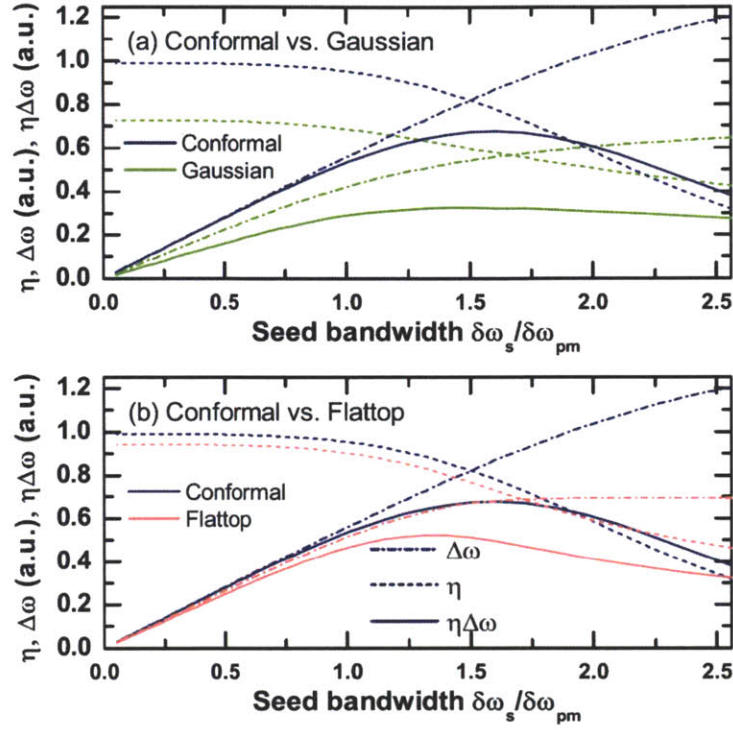
78

Figure 2.38 Efficiency, amplified signal bandwidth, and EBP versus seed bandwidth compared for (a) conformal and Gaussian pump profiles and (b) conformal and flattop pump profiles. For each type of pump profile, we choose the crystal length that provides the highest obtainable EBP for each case, requiring $L = L_{max}(0)$ for the conformal profiles, $L = 1.04L_{max}(0)$ for the flattop profiles, and $L = 1.09L_{max}(0)$ for the Gaussian profiles.

amplified signal bandwidth: the bandwidth is limited to the phase matching bandwidth. In contrast, conformal profiles [Figures 2.37e and 2.37f] employ a higher I_{p0} where $|\Delta k|$ is larger, resulting in a uniform $L_{max}(t)$ and an amplified signal intensity that is roughly uniform across the entire duration of the pump pulse for any seed bandwidth. Thus, the amplified bandwidth scales continuously with the seed bandwidth and can extend beyond the phase matching bandwidth. However, while choice of $I_{p0}(t) = I_{p0C}(t)$, sets $L_{max}(t)$ constant and suppresses $\Delta\kappa(t)$ relative to a flat-top or Gaussian profile (compare, for example, $\Delta\kappa(t)$ in
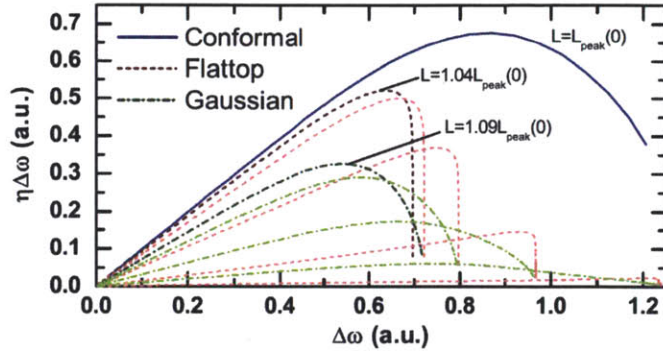
Figure 2.39 EBP versus amplified signal bandwidth for Gaussian, flattop, and conformal profiles. For Gaussian and flattop cases, the darker lines represent the choice of L (*i.e.*, degree of saturation) that maximizes the EBP, while the lighter curves are performance curves for longer crystal lengths. The crystal lengths plotted for the flattop case are $L/L_{max}(0) = 1.04, 1.1, 1.2, 1.4, 1.8$, and for the Gaussian case are $L/L_{max}(0) = 1.09, 1.2, 1.4, 1.8$.

Figures 34 and 35), the nonzero $\Delta\kappa(t)$ still leads to $\epsilon_{max}(t) < 1$, which is especially noticeable at the edges of the pump pulse, and full depletion is prohibited. As the seed bandwidth is increased, this becomes a greater limitation.

Performance is further analyzed by means of Figure 2.39, which plots the EBP as a function of the corresponding amplified signal bandwidth. This comparison is useful in aiding OPCPA design when peak power and signal bandwidth are both important qualities. Maximum EBP occurs when $L = L_{max}$ for conformal profiles, $L = 1.04 \cdot L_{max}$ for flat-top profiles, and $L = 1.09 \cdot L_{max}$ for Gaussian profiles. For longer crystal lengths (heavier oversaturation), the flat-top and Gaussian profiles produce wider bandwidths but lower EBP (lighter curves). Figure 2.39 illustrates that at a desired amplifier bandwidth, conformal profiles significantly outperform both flattop and Gaussian profiles in efficiency, especially at larger bandwidths.

In the previous analysis, we did not consider the possibility of practical limitations to the pump intensity. In OPA, high intensity along with a short crystal length is preferable for obtaining a large phase-matching bandwidth, but low intensity is preferable for avoiding nonlinear refractive effects because the B-integral scales with I_{p0}, but OPA gain scales with $\sqrt{I_{p0}}$. Therefore, I_{p0} is usually maximized such that it is kept reasonably below a B-integral imposed limit or a damage threshold.

It is useful, then, to compare pump profile performance when conformal, Gaussian, and flat-top pump profiles all share the same peak intensity. To carry this out, we repeat the analysis of the previous section with a different prescription for deriving $I_{p0C}(t)$. In order to match the peak I_{p0} of the Gaussian and flat-top profiles, we set the maximum value of I_{p0C} (i.e., at the pulse edges) equal to $I_{p0F}(0)$ and $I_{p0G}(0)$ (equal to 1). We then pick $L = L_{max}(t)$ at the pulse edges rather than at $t = 0$, and use Eq. 2.17 to find the corresponding $I_{p0C}(t)$ for $|t/\tau_0| <$ 1. The new conformal profiles are shown in Figure 2.40. Compared to Figures 2.37e and 2.37f, they have similar shape and performance. An important difference between this case and the case of unlimited I_{p0} is that we no longer have the ability to increase the maximum Γ. This means we cannot suppress $\Delta\kappa$ as well at the wings of the pulse. As a result, the amplified signal bandwidth cannot be extended quite as far beyond the phase matching bandwidth.
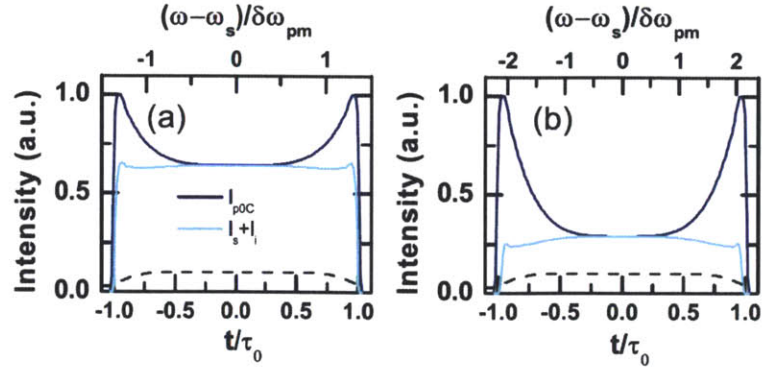
Figure 2.40 (Dark solid curves) Conformal pump intensity profiles, as in Figures 2.37e and 2.37f, but solved for $I_{p0}(\pm\tau_0) = 1$ and $L = L_{max}(\pm\tau_0)$. As in Figure 2.37, the seed bandwidth of (b) is 1.6× larger than (a). Also plotted: $I_{s0}(t)$ (dashed curve), plotted on a scale 100× higher, and $I_s(L) + I_i(L)$ (light solid curves).

Figure 2.41 summarizes the relative performance of conformal, Gaussian, and flattop pump profiles by plotting EBP versus amplified signal bandwidth. Comparing Figure 2.41a to Figure 2.39, we see the conformal case still outperforms flat-top and Gaussian, but is now more limited in maximum bandwidth.

Figure 2.41 also compares performance for different seed pulse shapes. In previous analyses, we have used a close to flat-top seed, $I_{s0}(t) = I_{s0}(0)exp[-(t/\tau_0)^8]$, with little temporal variation. However, typical OPCPA systems, especially broadband designs, often have variations in seed intensity covering 1 or 2 orders of magnitude across the bandwidth, and the signal chirp transfers this variation to the time domain. Figures 2.41b and 2.41c compare pump profile performance for $I_{s0}(t) = I_{s0}(0)exp[-2(t/\tau_0)^2]$ and $I_{s0}(t) = I_{s0}(0)exp[-3(t/\tau_0)^2]$, respectively. In each successive case there is more variation in I_{s0} across the duration of the pump pulse. Several observations are noteworthy. First, the conformal profile performance is always as good or better
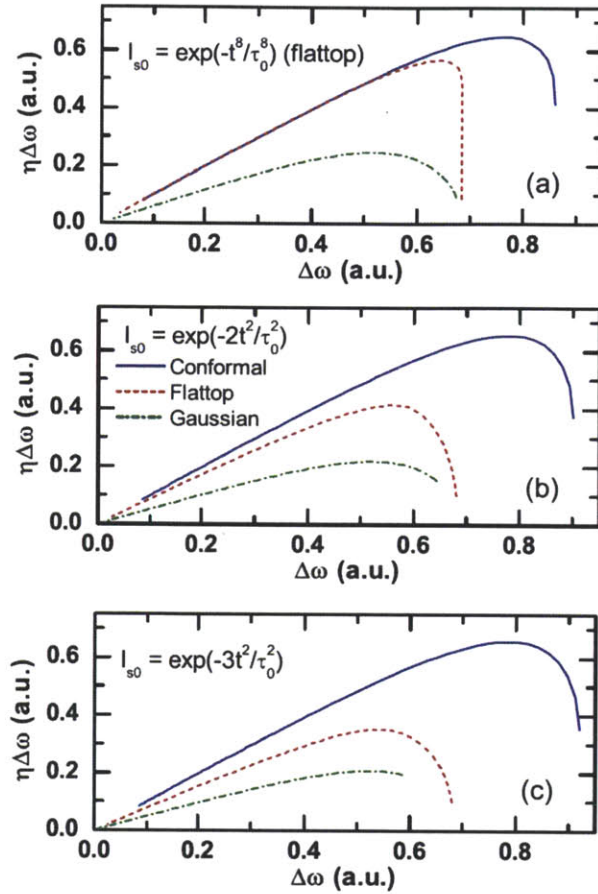
Figure 2.41 EBP versus amplified signal bandwidth for Gaussian, flattop, and conformal profiles, where all profiles (including conformal) share the same peak intensity, $I_{p0} = 1$. Each pane shows the results for a different seed profile, (a) having the least variation in I_{s0}, and (c) having the greatest.

than the flat-top. Second, it is clear that variations in I_{s0} reduce the performance of the flat-top and Gaussian cases, a result of further variation in $L_{max}(t)$. Third, the performance of the conformal profiles does not change much as the variation in $I_{s0}(t)$ increases, because the conformal profiles are adapted to variations in both $\Delta k(t)$ and $I_{s0}(t)$. We note that when the seed bandwidth is much narrower than the phase matching bandwidth and $I_{s0}(t)$ is flat-top, $I_{p0C}(t)$ is itself very nearly a flat-top. In this case, $I_{p0C}(t)$ and $I_{p0F}(t)$ have equal performance, as can be seen in

Figure 2.42a for $\Delta\omega < 0.5$. However, even in the narrow-bandwidth limit, as the variation in $I_{s0}(t)$ increases, $I_{p0C}(t)$ and $I_{p0F}(t)$ become less similar and the conformal profiles result in better performance.

Setting $L_{max}(t)$ uniform requires pulse shaping to the exact specifications of $I_{p0C}(t)$. In practice, it is helpful to understand the tolerance of conversion efficiency to errors $I_{p0}(t) \neq I_{p0C}(t)$. Figure 2.42 plots the values of $I_{p0}(t)$ above and below $I_{p0C}(t)$ at each value of t that corresponds to a 10% drop in gain, i.e., $I_s(L) + I_i(L) = 0.9 I'_{p0}$ for the amplifiers depicted in Figures 2.37e and 2.37f. Because gain saturates with I_{p0} near the conversion peak, the tolerances are reasonably large. For the case of seed bandwidth $\delta\omega_s = 1.4\delta\omega_{pm}$, the tolerances range from $0.82 I_{p0C} \leq I_{p0} \leq 1.19 I_{p0C}$ at $t = 0$ to $0.93 I_{p0C} \leq I_{p0} \leq 1.19 I_{p0C}$ at $t = \pm\tau_0$ [Figures 2.42a and 2.42b]. For larger seed bandwidth, $\delta\omega_s = 2.2\delta\omega_{pm}$, the tolerances tighten at $t = \pm\tau_0$, especially on the low end of I_{p0}: $0.98 I_{p0C} \leq I_{p0} \leq 1.15 I_{p0C}$ [Figures 2.42c and 2.42d]. Even in this case, however, there is a 17% low-end to high-end range over which conversion efficiency is >90% of its maximum.

Figure 2.42 also illustrates that the conformal profile solutions may be well approximated by polynomial functions,

$$I_{p0,Approx}(t) = \frac{I_{p0}(t = 0)}{\Gamma(t = 0)}\left(1 + \frac{\Delta k(t)^2}{4}\right) \qquad Eq.\,2.19$$

a fourth-order function of t for a group-velocity-matched amplifier and a parabolic function of t for a group-velocity unmatched amplifier. In both examples in Figure 2.42, $I_{p0,Approx}(t)$ is well within the calculated tolerances. This simple
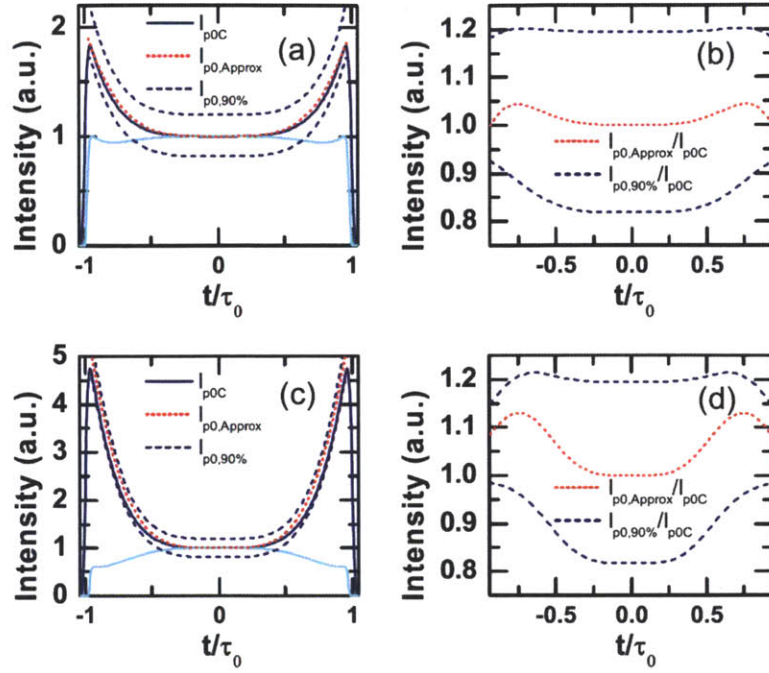
Figure 2.42 Study of tolerance to errors in $I_{p0C}(t)$ (solid curves). (a) and (b) correspond to the same amplifier depicted in Figure 2.37e, while (c) and (d) correspond to the amplifier depicted in Figure 2.37f. The two dashed curves, $I_{p0,90\%}(t)$, are the upper and lower bounds of $I_{p0}(t)$ that result in $I_s(L) + I_i(L) = 0.9I'_{p0}(t)$ at $L = L_{max}(0)$. Therefore, they represent the tolerances in $I_{p0}(t)$ for obtaining 90% of the maximum conformal profile conversion efficiency. $I_{p0,Approx}(t)$, Eq. 2.19, (dotted curve) approximates $I_{p0C}(t)$ well enough to stay within the bounds delineated by $I_{p0,90\%}(t)$.

approximation will become less accurate as the amount of variation of $I_{s0}(t)$ across the duration of the pump pulse increases, but offers a quick way of estimating the conformal profile in many cases.

Our analysis at the beginning suggested that conformal pump profile solutions may not be obtainable for all combinations of L, I_{s0}, and Δk. For example, in Figure 2.36, if we had chosen a new crystal length $L' > 1.8L$, there would not have been a solution. This indicates the existence of a limit to the conformal pump profile approach: for a given choice of L, there is a maximum value of Δk for

which a conformal I_{p0} can be found. In OPCPA, this translates to a limitation in bandwidth.

Suppose, for example, we set out to find a conformal pump profile using Eq. 2.17, setting $L = L_{max}(t = 0)$ for a wave-vector mismatch profile with $\Delta k(t = 0) = 0$. As $|t|$ increases, we will need a larger value of $I_{p0}(t)$ to compensate for the increasing $\Delta k(t)$. Eventually, $\Delta k(t)$ will be too large, and a root to Eq. 2.17 at $L = L_{max}(t = 0)$ will not exist. Given $G = I_{p0}(t = 0)/I_{s0}$, Table 2 lists the maximum Δk for which a conformal solution exists, as well as the corresponding signal frequency, and the corresponding conformal I_{p0C}. Note, for a very small G, $\delta\omega_{max} < \delta\omega_{pm}$ (defined for $I_{p0}(t = 0)$), and thus conformal pump profiles cannot be used to extend an amplifier bandwidth beyond the phase matching bandwidth. On the other hand, at a large G, a conformal profile can be found for a bandwidth far beyond the phase matching bandwidth, but this requires very high pump intensity. Finally, we note that these maxima correspond to a value of $\Delta\kappa = |\Delta k(t)|/2\Gamma(t) \cong 1$, and thus correspond to a $\epsilon_{max} \ll 1$. Therefore, as the seed bandwidth used in the amplifier approaches these maximum bandwidths, the maximum total conversion efficiency, Eq. 2.16, drops significantly.

Table 2   Limits to Conformal Pump Profiles

G	Δk_{max}	$I_{p0C.max}$	$\delta\omega_{max}$
10	0.25	1.00	0.60
30	0.89	1.16	1.21
10^2	1.2	1.6	1.5
10^3	2.2	5.1	2.2
10^4	4.5	20.	3.3
10^5	9.9	98.	5.1
10^6	23.	520.	8.0

In summary, we found that replacing the typically bell-shaped pump intensity profile with a complimentary, or *conformal*, choice of $I_{p0}(t)$ can significantly improve both the conversion efficiency and amplifier bandwidth. In many cases, the conformal profile shape can also provide significant performance enhancement relative to a flat-top profile that shares the same peak intensity, and the technique is useful at both pre- and power-amplification levels of signal gain. In addition to making $L_{max}(t)$ constant for all t, the use of a conformal pump profile has the additional advantage of naturally increasing the pump intensity where wave-vector mismatch is high. In terms of its effect on amplifier bandwidth, the former offsets the latter. As a result, the conformal pump profile method allows decent conversion efficiency when seeding the amplifier with a bandwidth significantly wider than the phase matching bandwidth.

We also explored some limitations of the conformal pump profile technique, including the nonexistence of conformal profile solutions when the seed bandwidth too-far exceeds the phase-matching bandwidth. A comparison of conformal, flat-top, and Gaussian pump profile shapes as a function of amplifier bandwidth also illuminated the utility of the conformal pump profile method in a variety of settings. Figure 2.41 is particularly illuminating in this context, and can be used to support the delineation of OPCPA into three regimes, each with a different degree of utility for the conformal pump profile method.

1. $\delta\omega_s \ll \delta\omega_{pm}$. In the case that the seed bandwidth is much narrower than the phase matching bandwidth, $\Delta k \cong 0$ at all t. In this case, when the seed spectrum is a flat-top, the conformal pump profile is a flat-top as well. This

87

is the regime of several narrow-bandwidth OPCPA designs in which flattop pump profiles have been used to successfully obtain high conversion efficiency in combination with a fairly uniform seed intensity, e.g., **[36]**, **[37]**. However, if I_{s0} varies significantly [e.g., in Figure 2.41c, in which the seed intensity varies by -13 dB over the duration of the pump], the conformal profile will differ from a flattop and perform significantly better.

2. $\delta\omega_s \gg \delta\omega_{pm}$. In the case that the seed bandwidth is much broader than the phase-matching bandwidth, pump profiles of all types perform badly. In the conformal profile case, if a solution can be found (see Table 2), $L_{max}(t)$ is uniform, but the temporal range where signal frequency far exceeds the phase-matching bandwidth will suffer from very low conversion efficiency, making the amplifier too inefficient to be useful.

3. $\delta\omega_s \sim \delta\omega_{pm}$. In this regime, including cases where the seed bandwidth exceeds the phase matching bandwidth by a modest amount, conformal profiles can outperform other profile shapes by a significant amount in both efficiency and bandwidth, and several times in the EBP. In this case, $\Delta k(t)$ varies significantly, but the maximum obtainable conversion efficiency is still usefully large. A conformal pump profile is even more useful in this context if $I_{s0}(t)$ varies significantly.

Conformal profiles are thus especially useful in a regime that is particularly important for the advancement of ultrafast science: when the amplifier bandwidth is limited by the phase matching bandwidth, conformal profiles extend both the bandwidth and conversion efficiency by modest amounts, it can more than double

the EBP compared to flat-top profiles, and push the EBP compared to Gaussian profiles by several times. For amplifiers that do not employ a large fraction of the phase matching bandwidth, conformal profiles still boost performance: Gaussian pump profiles are almost always non-ideal, and flat-top pump profiles are non-ideal when $I_{s0}(t)$ varies significantly.

The use of conformal profiles, of course, requires pulse shaping methods. In the case of pump pulse shaping, it is particularly important that the shaping method is not lossy. Otherwise, loss of pump energy could make the resulting gain in conversion efficiency useless. Several amplifier designs have employed lossless shaping methods by adding a shaping device before the final amplification stage of a pump laser system that pre-compensates for gain saturation effects [36], [37], [63]. In those systems, flat-top pulse shapes were employed, but the technique could be equally applicable to generating conformal-type profile shapes. Lossless shaping of pulses is especially challenging for transform-limited pump pulses with durations in the few-picosecond range (which are often found in broadband OPCPA designs), because the bandwidths are too narrow for easy spectral shaping and the required temporal transients are too short to be generated by the fastest time-domain electronic modulators. In the context of both OPCPA and photoinjector drive lasers for x-ray free electron lasers, several groups have invented picosecond pulse shaping methods, employing pulse splitting and recombination with birefringent materials [35], [64], [65]. These might be promising methods if they can prove to have the efficiency and flexibility needed in our context.

89

Toward this aim, we consider pulses in the hundreds of femtoseconds range transform-limited duration in combination with spectral filters to be a promising possibility. Prior to the power amplification stage of a pump laser system, such pulses could be chirped to tens of picoseconds duration and spectrally shaped using interference filters: the bandwidth would be broad enough to support short enough temporal features, and the long associated dispersion length and large chirp would keep dispersive propagation effects negligible over the OPA crystal length.

Chapter 3

Waveform Synthesis by Coherent Wavelength Multiplexing

Over the last decade, the control of atomic-scale electronic motion by optical fields strong enough to mitigate the atomic Coulomb potential, has broken tremendous new ground with the advent of phase controlled high-energy few-cycle pulse sources. Further investigation and control of these physical processes, including high-harmonic generation, ask for the capability of waveform shaping on sub-cycle time scales, which requires a fully phase-controlled multiple-octave-spanning spectrum. Such features would allow arbitrary shaping of the strong electric-field waveforms for steering ionized electron wavepackets [15] and precise control of tunneling and multiphoton ionization events. To date, no single laser source can support a bandwidth of more than an octave [46], [66]. To extend the laser spectrum, there are in general two directions: (i). nonlinear mixing of high intensity laser light to reach new wavelength ranges, and (ii). coherent synthesis of the multi-wavelength output from intense lasers.

Supercontinuum generation [12], [67–70] and molecular modulation [71–75] are two established nonlinear mixing techniques to expand the laser bandwidth to multiple octaves. Supercontinua with a bandwidth close to two octaves and a pulse energy in the micro-joule range have been demonstrated by self-channeling of a 5-fs laser pulse in helium at high pressure, and the further dispersion management

by chirped mirrors has recently led to the generation of isolated sub-optical cycle pulses [76]. On the other hand, with pulse energy at the nano-joule level, molecular modulation provides the broadest spectrum ever (more than two octaves), and periodic electric-field waveforms with square or triangle shapes have been demonstrated recently [75].

Coherent synthesis of pulses with different spectra, or wavelength multiplexing, presents another route towards obtaining a multi-octave spanning laser spectrum. The benefit of this approach lies in its modular design and scalability in both bandwidth and pulse energy. Attempts to combine two independent mode-locked lasers have seen some success, e.g., for frequency metrology [77], [78], but are challenging because of the differential phase noise beyond the achievable feedback loop bandwidth. This problem was initially circumvented by coherently adding two pulse trains derived from the same fiber laser, resulting in the first demonstration of an isolated single-cycle optical pulse source [79]. This proved the feasibility of pulse synthesis at the nano-joule level, but achieving high pulse-energy requires synthesis of low-repetition-rate pulses, which is a challenge because of the environmental perturbations typical of high-energy amplifiers. Broadband optical parametric chirped pulse amplifier (OPCPA) is the most promising technology for producing wavelength-tunable, high-peak-power and high-average-power, few-cycle optical pulses with good pre-pulse contrast [31]. Broadband OPCPAs also maintain good carrier-envelope phase (CEP) stability due to the low thermal load and the small dispersion required to stretch and compress the signals. Thus, OPCPA stands out as the ideal building
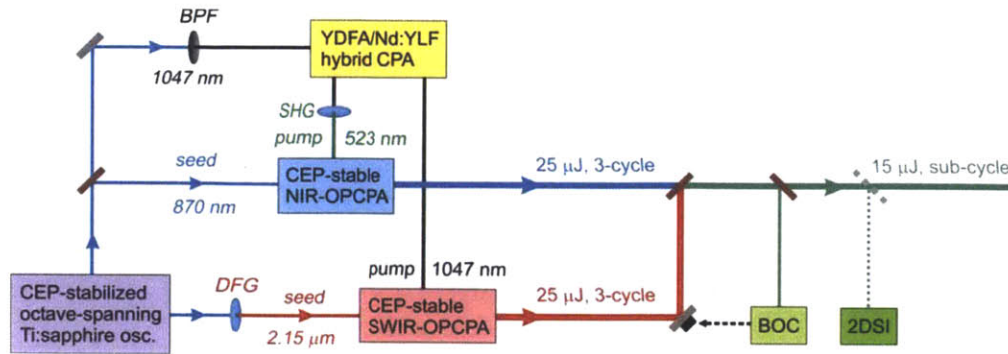
Figure 3.1 Scheme of the high-energy optical waveform synthesizer.

module for high-energy pulse synthesis. An approach to high-energy pulse synthesis based on combining the pump and its second harmonic, signal, and idler of a multi-cycle OPA is being investigated and periodic non-sinusoidal electric-field waveforms under a multi-cycle envelope have been demonstrated recently [80].

In this chapter, we present the coherent synthesis of the already few-cycle pulses from two broadband OPCPAs, working in the near-infrared (NIR) and the short-wavelength infrared (SWIR) respectively. Details of the OPCPAs are already given in Chapter 2. Our source allows the generation of isolated high-energy non-sinusoidal optical waveforms with full phase control capability over the spectra spanning close to two octaves [23]. Figure 3.1 shows a schematic of the system. It starts with an actively CEP-stabilized octave-spanning Ti:sapphire oscillator. The output of the oscillator is used to seed the two OPCPAs as well as the Ytterbium-doped fiber amplifier (YDFA)/Nd:YLF hybrid CPA, which pumps the two OPCPAs. Outputs from the two OPCPAs are combined in a broadband neutral beamsplitter. A feedback loop based on a balanced optical cross-correlator (BOC)
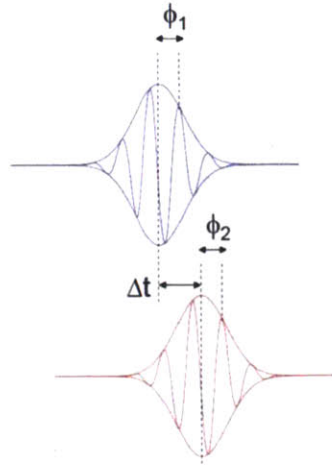
Figure 3.2 Cartoon showing a way to establish the phase coherence between the two OPCPA pulses.

[81], allowing attosecond-precision relative timing stability, is implemented to ensure the coherent synthesis of the two pulses. Furthermore, the inclusion of an acousto-optic programmable dispersive filter (AOPDF) in each OPCPA allows independent spectral phase and amplitude adjustment of each pulse, enabling control and optimization of the synthesized waveform. Overall, a pulse energy of 15µJ is obtained with a bandwidth close to two octaves and the shortest high-field transient lasting only 0.8 cycles (amplitude FWHM) of the centroid frequency. By simulation, we also present an example of the unique features of our source as a driver for high harmonic generation (HHG).

Figure 3.2 shows the procedure taken to ensure the phase coherence between the two OPCPA pulses: we first ensure stabilization of the CEPs of the NIR-OPCPA pulses (ϕ_1) and SWIR-OPCPA pulses (ϕ_2), and then stabilize the relative timing between the two OPCPA pulses (Δt). Precise stabilization of these three parameters is required for coherent synthesis of the two OPCPA pulses, and

subsequent control of each parameter allows precise waveform shaping. In principle, one can choose another way to stabilize these three parameters: first stabilize the CEP of one of the OPCPA pulses (ϕ_1), then stabilize the relative phase between the two OPCPA pulses ($\Delta\phi$), and finally stabilize the relative timing between the two OPCPA pulses (Δt). Since the measurement of $\Delta\phi$ will inevitably be influenced by the change in Δt, diagonalization of the effects from $\Delta\phi$ and Δt becomes critically important and any error in determining the transfer function will lead to residual jitters. In contrast, our method inherently diagonalizes all three parameters so that we can achieve lower residual jitters. In addition, there is only one relative measurement necessary in our method, which thus provides greater scalability and flexibility in the context of modular design.

3.1 Carrier-envelope phase stabilization

There are two factors which determine the CEP stability of the OPCPA pulses: CEP stability of the seed and the excess phase noise added by the amplifiers.

The seed to the SWIR-OPCPA is via intrapulse DFG and thus the CEP is passively stabilized [82]. On the other hand, the seed to the NIR-OPCPA is just the output of an octave-spanning Ti:sapphire oscillator and thus an active feedback control is required to stabilize its CEP. Figure 3.3 shows the active CEP stabilization setup. The output of the oscillator is split in a dichroic mirror (DM) that transmits the light from 650 to 1050nm and reflects the light below 650nm and above 1050nm. The transmission port is used for seeding the rest of the system, and
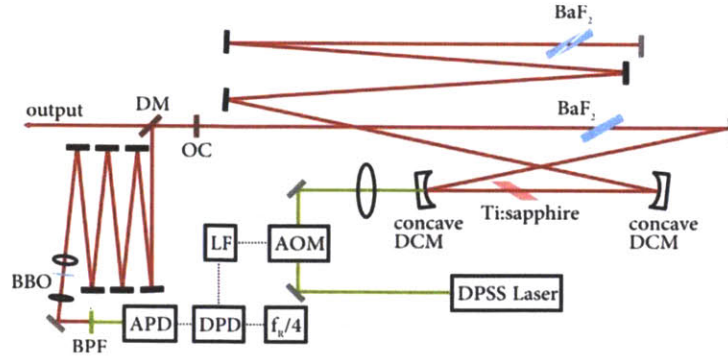
95

Figure 3.3 Scheme of the CEP-stabilized octave-spanning Ti:sapphire oscillator.

the reflection port is directed into a *f-2f* self-referencing interferometer. A collinear configuration is chosen for its robustness against environmental noise. Six bounces on DCMs are employed for proper group-delay adjustment to maximize the CEP-beat signal. After the DCM-based delay line, the beam is focused onto a 1 mm-thick type I β-barium borate (BBO) crystal for second-harmonic generation (SHG). The emitted SHG light and the fundamental light are spatially filtered using an iris diaphragm, spectrally filtered using a 10-nm interference bandpass filter (BPF) centered at 570nm, and directed to a fast avalanche photodiode (MenloSystems APD210). The CEP-offset frequency (f_{ceo}) is locked to a fourth of the oscillator's repetition rate (f_R) through a phase-locked loop (PLL) that feeds back to an acousto-optic modulator (AOM) regulating the pump power, thus shifting the f_{ceo}. Of note, instead of locking the f_{ceo} to zero, we lock it to $f_R/4$. Then we treat this RF signal, $f_R/4$, as the master clock to generate the 1-kHz trigger for the pump systems and the AOPDFs. This way, the seed pulses amplified by the NIR-OPCPA will have identical CEP as also demonstrated by other groups [83]. A digital phase detector (DPD) is used to increase the capture range ($\pm32\pi$) beyond a traditional analog
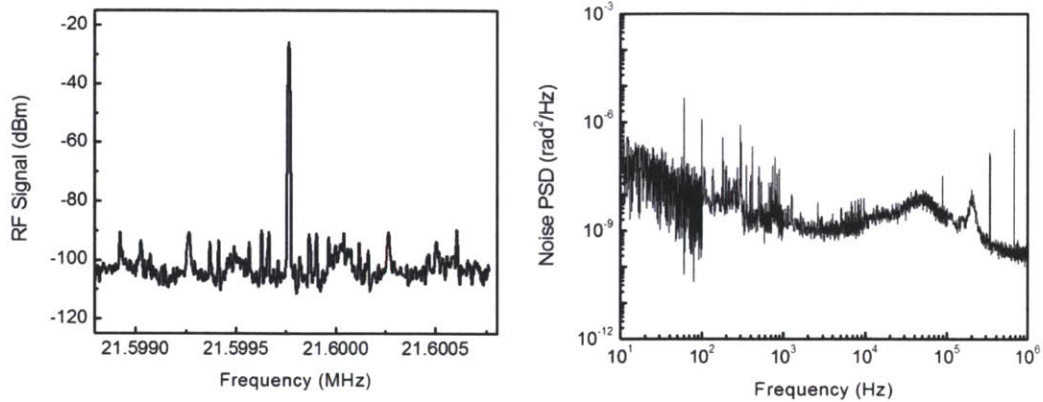
96

Figure 3.4 (a) RF spectrum of the locked CE-beat signal in log scale showing a resolution-limited linewidth of 5 Hz. (b) PSD of the residual CEP fluctuations.

mixer ($\pm\pi/2$). A signal-to-noise ratio of >40dB is constantly achievable with a 100-kHz resolution bandwidth.

Figure 3.4a shows the measured RF spectra of the CE beat note signal when the laser is locked. As demonstrated by the plot, a delta-function-like CE beat note with a linewidth of <5 Hz (the resolution limit of the RF spectrum analyzer) is achieved. In order to precisely estimate the residual CE phase error when the laser is locked, the output from the DPD is fed into a vector signal analyzer (VSA) for measuring the power spectral density (PSD) of the residual CEP fluctuations S_ϕ (Figure 3.4b). The integrated CEP *r.m.s.* phase error, calculated from $\Delta\varphi_{rms} = \sqrt{\int_{10Hz}^{1MHz} S_\varphi(f)df}$ is 60 mrad. Since the major source of CEP is the intracavity intensity fluctuations introduced by pump laser noise, the phase noise rapidly decays beyond the relaxation frequency that is typically a few hundred kHz. Therefore, the upper limit of the measurement is set to be 1 MHz to exclude the

high-frequency noise contributed by the electronics noise floor rather than the laser phase noise itself.

As mentioned in the previous chapter, a high OPA gain of >40dB can be easily achieved in a few mm nonlienar crystal with literally no thermal load. Thus, the CEP stability degradation due to thermal drift is of minor importance in an OPCPA. Pump intensity fluctuation is another source that can introduce excess CEP noise to the signal. The phase evolution equations in derivative form for signal, idler, and pump waves can be expressed as [29]:

$$\frac{d}{dz}\phi_s = \frac{\Delta k}{2}\left[1 - \frac{I_{s0}}{I_s(z)}\right]$$

$$Eq.\,3.1a$$

$$\frac{d}{dz}\phi_i = \frac{\Delta k}{2}$$

$$Eq.\,3.1b$$

$$\frac{d}{dz}\phi_p = \frac{\Delta k}{2}\left[\frac{I_{p0}}{(\omega_p/\omega_s)(I_{s0} - I_s(z)) + I_{p0}} - 1\right]$$

$$Eq.\,3.1c$$

These equations can be directly integrated using the exact solution for $I_s(z)$, Eqs. 2.2. Plugging Eq. 2.4, a simplified form of the OPCPA gain, into Eq. 3.1a, we arrive at a simple form of the phase evolution as

$$\phi_s(z) = \frac{\Delta k}{2}\left[z + \frac{2}{g}exp(-2gz)\right]$$

$$Eq.\,3.2$$

Derivative of the signal phase with respective to the pump intensity is

$$\frac{d}{dI_p}\phi_s = \frac{8\Delta\kappa L^2}{\sqrt{1 - \Delta\kappa^2}}\left(\frac{4\pi^2 d_{eff}^2}{n_s n_i n_p \lambda_s \lambda_i c\varepsilon_0}\right)\left(1 - \frac{1}{G_c^2}\right)exp(-G_c)$$

$$Eq.\,3.3$$

where $G_c = 2gL$. As an example, let us now put in realistic numbers into Eq. 3.3 ($G_c = 9$, $\Delta\kappa = 0.5$, $\lambda_p = 523nm$, $\lambda_s = 800nm$, $L = 3.5mm$), we then get $d\phi_s = 8 \cdot 10^{-17} \cdot dI_p$. Again, the CEP noise introduced by the pump intensity fluctuation is
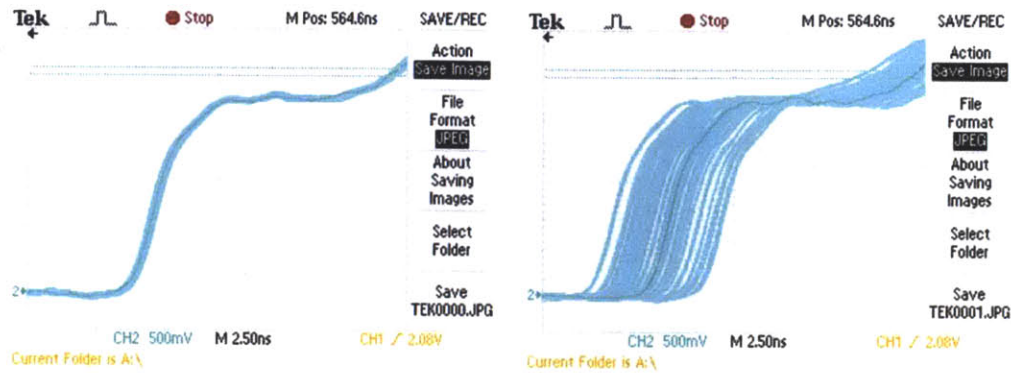
Figure 3.5 A PLL circuit is built to synchronize the AOPDF's internal sampling clock with the master clock and the jitter is reduced by more than an order of magnitude.

negligible. An 1 GW/cm^2 pump intensity fluctuation only introduces a CEP noise of ~1 mrad. A detailed numerical simulation agrees with the observation [41].

Still another source of CEP noise is from the AOPDF, which controls the phase by sending a chirped RF pulse to change the positions where optical wavelengths are diffracted inside the acousto-optic crystal. If the internal sampling clock of the AOPDF is free-running, the jitter between the RF pulse and the optical pulse will result in CEP fluctuation. To solve the problem, a PLL circuit is built to synchronize the AOPDF's internal sampling clock with the master clock. Figure 3.5 shows the jitter between the RF pulse and the optical pulse with (a) and without (b) the PLL in operation. The PLL improves the jitter by more than an order of magnitude and reduces the excess CEP noise to below 100mrad.

To verify the CEP stability of the OPCPA pulses, we set up nonlinear self-referencing interferometers similar to the one sketched in Figure 3.3. The two differences are: (i) the spectrum of each OPCPA is not octave-spanning and thus an additional supercontinuum generation stage is necessary to overlap the fundamental
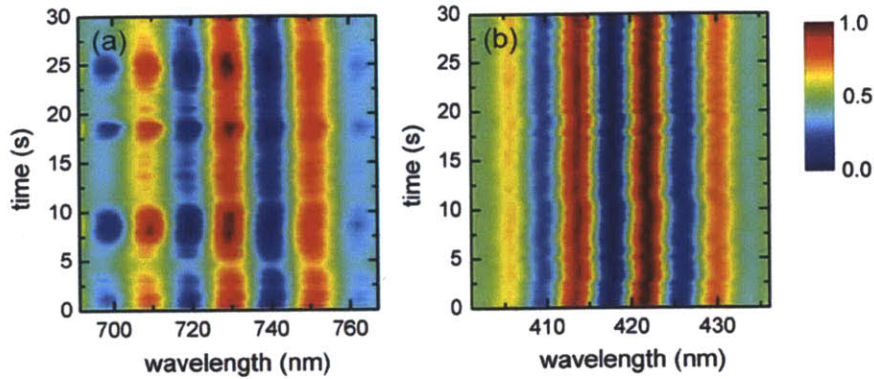
Figure 3.6 (a) *f-3f* inteferogram of the SWIR-OPCPA with 5-shot integration over 30 seconds, measuring an r.m.s. CEP fluctuation of 127 mrad. (b) *f-2f* inteferogram of the NIR-OPCPA with 5-shot integration over 30 seconds, measuring an r.m.s. CEP fluctuation of 135 mrad.

spectrum with the harmonic spectrum; (ii) a spectrometer, instead of a photodetector, is used to record the spectral interference over time. This spectral-resolved measurement decouples the effect of CEP fluctuation from the effect of laser power fluctuation. Using an *f-3f* interferometer and five-shot integration, the CEP stability of the SWIR-OPCPA was confirmed with an *r.m.s.* fluctuation of 127-mrad (Figure 3.6a). A sapphire plate is used here to generate the supercontinuum. An *f-2f* interferometer with five-shot integration was used to confirm the CEP stability of the NIR-OPCPA, which shows an *r.m.s.* fluctuation of 135-mrad (Figure 3.6b). A CaF_2 plate is used here to generate the supercontinuum.

3.2 Relative Timing Stabilization

Outputs from the two OPCPAs are individually collimated with the diameter of the SWIR-OPCPA 2.5 times larger than that of the NIR-OPCPA and then combined in a broadband neutral beamsplitter. When focused, the two beams

at the focus have the same spot size and this "constant waist width" configuration [84] offers the unique property that the temporal pulse form remains unchanged upon propagation, whereas distortion appears in the near-field when the "constant diffraction length" configuration is used [84]. The overall spectrum spans over 1.8 octaves and the energy of the synthesized pulse is 15 µJ.

The broadband neutral beamsplitter introduces additional 25% energy loss. In addition, only half of the synthesized pulse energy is available for experiments because the other half is directed to the BOC. Since the pulse energy directed to the BOC is much more than is needed, a custom-made dichroic mirror can be implemented to improve the experimentally available pulse energy by a factor of >2. Figure 3.7 shows the characterization of the indium-tin-oxide (ITO) dichroic mirror. It is transparent in the visible to NIR regime, but behaves like a metallic mirror in the SWIR regime. The dispersion in the NIR regime is small and smooth such that it can be compensated with the AOPDF. With this new dichroic mirror, the energy of the pulse synthesizer can be improved by a factor of >2.
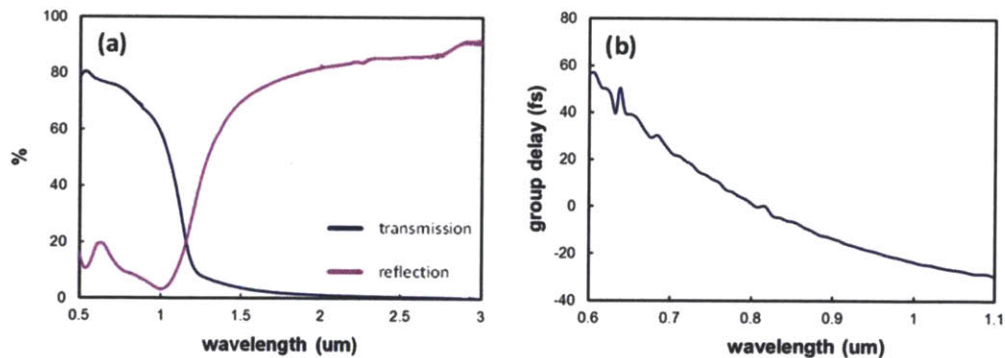

Figure 3.7 (a) Transmission and reflection characteristics of an ITO dichroic mirror. (b) Dispersion characteristics of an ITO dichroic mirror in the near-IR regime where the light is transmitted.

As described in the previous section, the CEP of the SWIR-OPCPA is passively stabilized up to residual *r.m.s.* fluctuations of 127 mrad while the CEP of the NIR-OPCPA is actively stabilized to within a *r.m.s.* fluctuation of 135 mrad. Stabilization of the relative timing then ensures the phase coherence between the two OPCPA pulses. To this end, a feedback loop based on a BOC is implemented **[81]**.

A BOC is the optical equivalent of a balanced microwave phase detector and is particularly suitable for measuring slow timing drifts with atto-second precision because the balanced detection configuration cancels the amplitude noise. Figure 3.8a shows the schematics of the BOC. One part of the combined beam is directed to the BOC which consists of two nearly identical cross-correlators using 200-μm-thick BBO crystals, phase matched for sum-frequency generation (SFG) of 870-nm light and 2.15-μm light. Use of the SWIR-OPCPA delay stage and a 4-mm-thick calcium fluoride (CaF_2) window between cross-correlators sets the group delay between pulses to +25 fs in one cross-correlator and -25 fs in the other. An additional ~2-mm-thick CaF_2 window ensures zero group delay between both pulses at the combined output. For deviations from this zero-delay configuration of up to ±20 fs, the photodetector signal is linearly proportional to the time difference and thus can be used as the error signal fed to the loop filter in the feedback system (Figure 3.8b). Furthermore, in the vicinity of the zero crossing, the setup delivers a balanced signal and thus the amplitude noise of each OPCPA output does not affect the detected error signal. Since the balanced operation is key to atto-second precision, it is thus not desirable to offset the locking point as the mechanism to
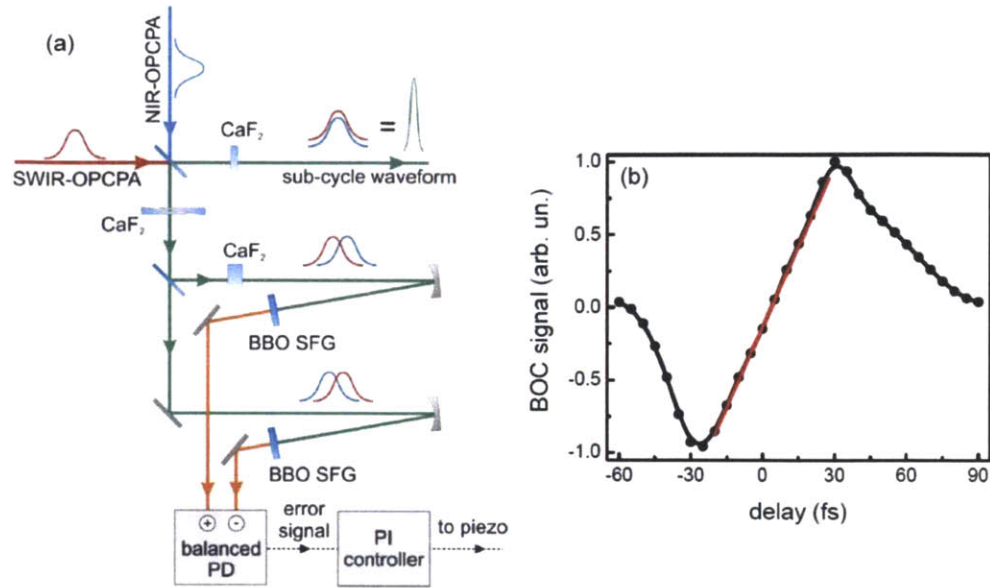
Figure 3.8 (a) Scheme of the BOC-assisted feedback loop for the stabilization of the relative timing. (b) BOC signal as a function of the relative timing between the two OPCPA pulses. The red line indicates the linear operation regime. BOC: balanced optical cross-correlator; SFG: sum-frequency generation; PD: photodetector.

change the relative timing (Δt). Instead, the wedge pair in the path to the BOC should be used to change the relative timing (Δt) without offsetting the locking point and introducing additional dispersion to the combined output.

Since the OPCPAs and pump laser system are all seeded by a single octave-spanning Ti:sapphire oscillator, the two OPCPA pulses are already synchronized to within environmental fluctuations. Freely running, the system displays a peak-to-peak relative timing drift of 30fs over a measurement time of 10s, with the main noise contribution below 30-Hz (Figure 3.9). Feedback control of the SWIR-OPCPA's path length over a bandwidth of 30 Hz reduces the relative timing drift to 250 as, less than 5% of the oscillation period of the SWIR-OPCPA (7.2-fs).
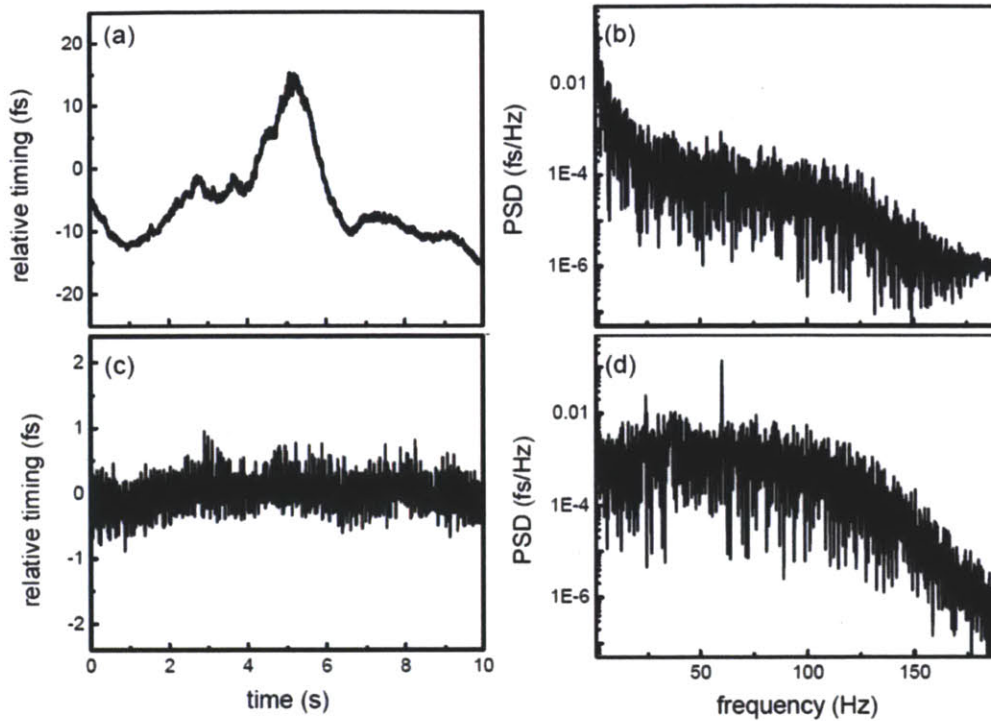
Figure 3.9 (a) Without the feedback loop, the relative timing experience a drift of 30 fs over 10 seconds. (b) The PSD of the relative timing fluctuation, showing the main noise contribution, is below 30 Hz. (c) With the feeback loop, the r.m.s. relative timing jitter is reduced to 250 as over 10 seconds. (d) The PSD of the residual relative timing jitter. PSD: power spectral density.

Since these three parameters (the CEP of the NIR-OPCPA, ϕ_1, the CEP of the SWIR-OPCPA, ϕ_2, and the relative timing between the two OPCPAs, Δt) significantly influence the synthesized electric-field waveform, it is important to make sure that the residual jitter is sufficiently small to impart only a negligible effect. Figure 3.10 shows the synthesized electric-field waveform with the *r.m.s.* value of each residual jitter added to the respective parameters (black dotted line) superimposed with the unperturbed waveform (green solid line). To quantify the waveform difference, we calculate the relative squared error (RSE) in a 10-fs time window that covers the main pulse as well as the two satellite pulses. Currently the

250-as relative timing jitter results in the largest waveform change (2.22% RSE), but it can be further reduced using a broader feedback bandwidth.

Of note, since the BOC is not completely symmetric due to the group-delay walk-off in the BBO and the dispersion in the CaF_2 window, the zero crossing of the BOC signal does not correspond to the point that the two pulses are exactly overlapped, as shown in Figure 3.11 by simulation. Hence, one would need a device to measure the relative timing (Δt) and adjust the CaF_2 window thickness correspondingly. A two-dimensional spectral-shearing interferometer (2DSI) [85], a variation of spectral-shearing interferometry [86], serves the purpose and it is used
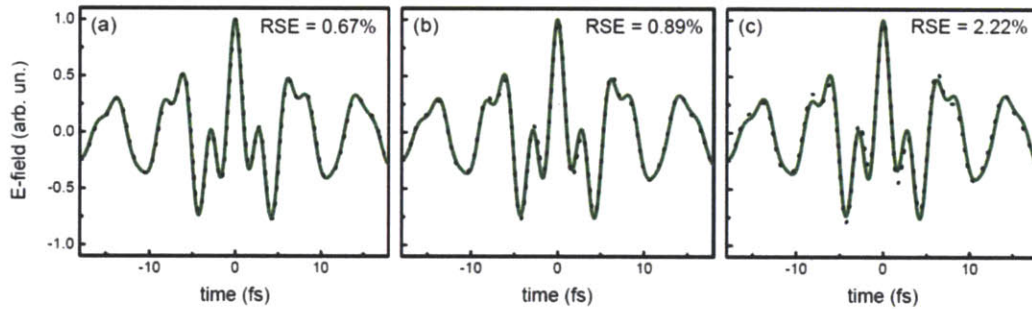

Figure 3.10 Waveforms under r.m.s. residual jitters. While the green solid line is the unperturbed waveform, the black dotted line is obtained by adding 135 mrad to ϕ_1 in (a), adding 127 mrad to ϕ_2 in (b), and adding 250 as to Δt in (c). RSE: relative squared error.
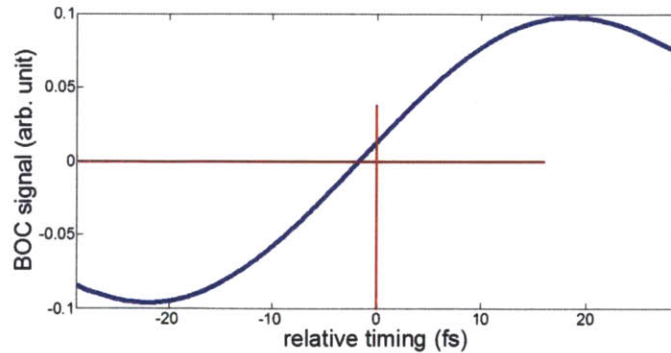

Figure 3.11 Calculated BOC signal as a function of relative timing.

105

to characterize the synthesized pulse. Details of the 2DSI will be given in Section 3.6.

Figure 3.12 shows the schematics of the 2DSI. The synthesized pulse is first split by a beam sampler whose second surface is anti-reflection coated. A part of the beam (4%) is Fresnel reflected and only guided via silver mirrors before being mixed in a 40-μm type II BBO. The other part of the beam (96%) passes through the beam sampler and is highly stretched before being split again by a cube beamsplitter, routed to the BBO and mixed with the unchirped pulse. The portion mixed with the unchirped pulse is purely derived from the NIR-OPCPA to ensure there is a definite reference for the measured wavelength-dependent group-delay throughout the whole spectrum from 700nm to 2500nm. Two collinear, temporally overlapped, but spectrally sheared up-converted pulses are then generated from the mixing of the unchirped pulse and the two chirped pulses. The shear frequency is set at 14.5THz such that a temporal window over which the pulse can be reliably measured without phase ambiguity is 70fs. To observe the interference between the two up-converted pulses, which encodes the wavelength-dependent group-delay information, the delay of one of the highly chirped pulses is scanned over a few optical cycles. Due to the strong chirp, the scanning of the delay over a few optical cycles can be approximated as a pure phase modulation (ϕ_{gd}). The spectrum of the up-converted signal is recorded as a function of this delay, yielding a two-dimensional intensity plot that is shown in Figure 3.13a. The interpretation of the 2DSI data is relatively straight-forward: each spectral component is vertically shifted in proportion to its group-delay.
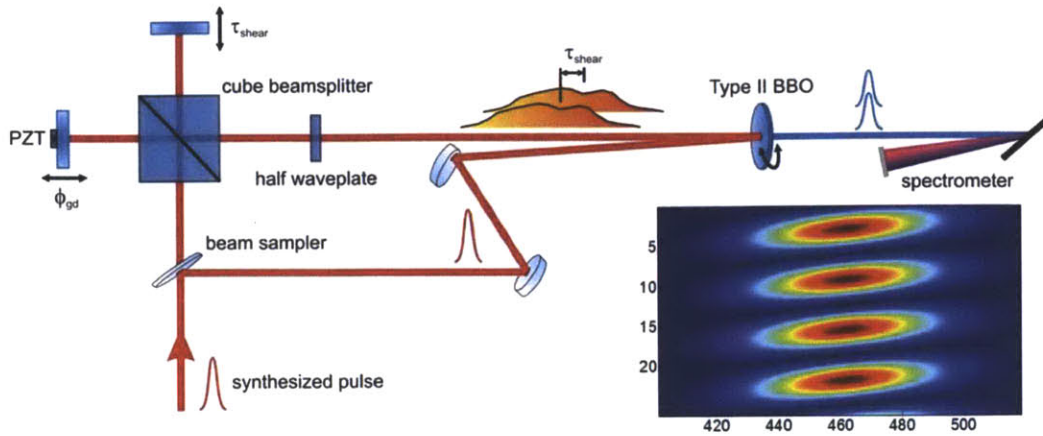
Figure 3.12 Scheme of the 2DSI for characterizing the synthesized pulse.

Figure 3.13b plots (dashed lines) the wavelength-dependent group-delay of the synthesized pulse extracted from the 2DSI measurement (Figure 3.13a). It shows that the two OPCPA pulses are indeed temporally overlapped and each is well compressed to within 10% of its transform-limited pulse duration. Figure 3.13c plots a synthesized electric-field waveform and intensity profile assuming the CEPs (ϕ_1 = 650mrad, ϕ_2 = -750mrad) optimal for achieving the shortest high-field transient, which lasts only 0.8 cycles (amplitude FWHM) of the centroid frequency (λ_c = 1.26 µm). The lower inset of Figure 3.13c clearly shows that the synthesized electric-field waveform is non-sinusoidal and the main feature lasts less than an optical cycle. Due to the large gap in the combined spectrum, there are wings 4.8 fs from the central peak as shown in Figure 3.13c. As we will show in Section 3.4, for processes initiated by strong-field ionization, these wings have a negligible effect. For more demanding applications, the wings can be suppressed by extension of the coherent wavelength multiplexing scheme to include a third OPCPA, centered at 1.5 µm **[87]**, to fill the spectral gap.
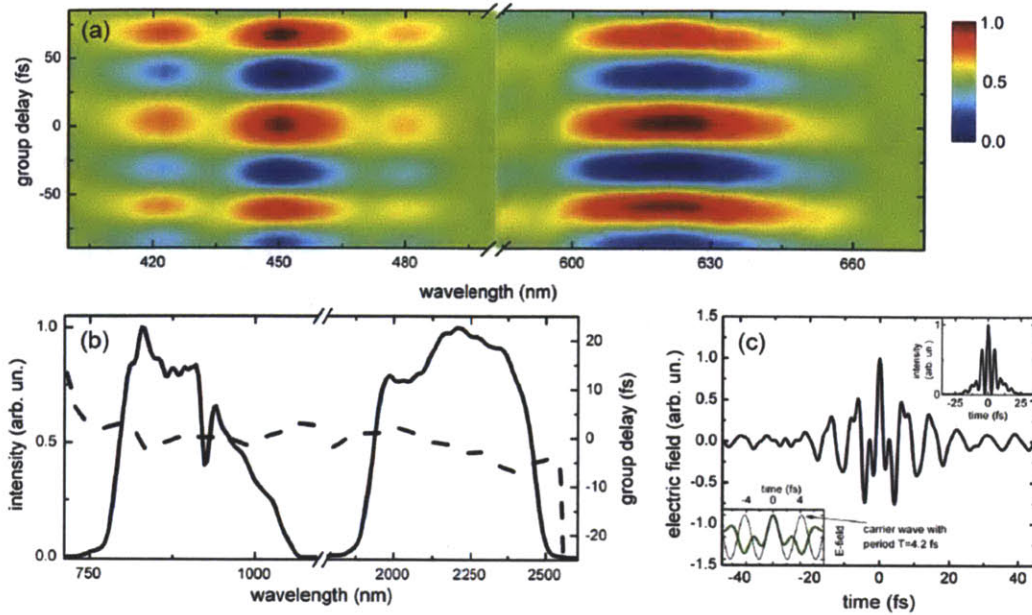
Figure 3.13 (a) 2DSI data of the synthesized pulse. (b) The extracted wavelength-dependent group-delays superimposed on the OPCPA output spectra. (c) The synthesized electric-field waveform assuming CEPs (ϕ_1=650 mrad, ϕ_2=-750 mrad) optimal for achieving the shortest high-field transient, which lasts only 0.8 cycles (amplitude FWHM) of the centroid frequency. Lower inset: the synthesized waveform is superimposed with the electric field oscillating at the centroid frequency, showing that the synthesized waveform is non-sinusoidal and the main feature lasts less than an optical cycle. Upper inset: corresponding intensity profile.

3.3 NIR waveform synthesizer seeded by white light continuum

The concept and technology demonstrated here can be further scaled in both energy and bandwidth to expand its applicability to strong-field physics experiments. Figure 3.14 shows a schematic of the proposed scaled-up system. It is comprised of a number of OPCPAs seeded by a single CEP-stabilized light source both directly and through nonlinear effects (NLEs) which preserve the CEP
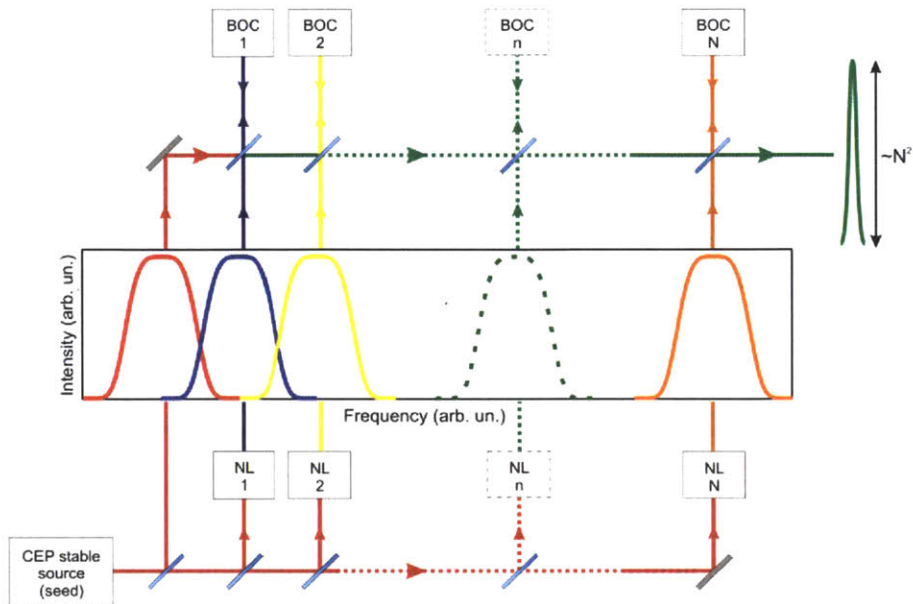
108

Figure 3.14 Scheme of the future scaled-up system.

stability such as intrapulse DFG, self-phase modulation, and Raman shifting. The OPCPA pulses are combined in custom-made dichroic mirrors and the BOC-assisted feedback loops stabilize the relative timing. Different from the simple coherent beam combination of identical optical amplifiers, which leads to a linear peak-power scaling with the number of sub-modules, the proposed system increases the peak-power quadratically since both energy and bandwidth scale linearly with the number of sub-modules.

The wavelength multiplexing gives us additional flexibility to control and optimize the synthesized waveform because each individual OPCPA has to amplify only a moderate bandwidth, much less than an octave. In this regime, the CEP (relative to the reference module) and the relative timing can be approximately lumped as only one independent variable. For a system consisting of N sub-modules, only N feedback loops are necessary as opposed to 2N-1. Figure 3.15

depicts the concept using the 3-cycle pulses. Assume now we shift the CEP of the SWIR-OPCPA pulses by π compared to the condition which results in the synthesized waveform shown in Figure 3.13c (red solid line here). The effect of the CEP shift on the synthesized waveform can be cancelled by changing the relative timing by 3.6 fs (black dotted line). The waveform difference in a window of 26 fs, which contains 86% of the pulse energy, is only 1.02% (relative squared error). A CEP jitter of 100 mrad will result in the same relative squared error. Thus we conclude that control of the reference module's CEP and the relative timing is sufficient for systems based on synthesizing 3-cycle (or more) pulses.

In the following paragraphs, a NIR waveform synthesizer combining two broadband OPAs seeded by white light continuum (WLC) is presented. The work is a joint effort of Professor Giulio Cerullo's group at Politecnico di Milano and the MIT group. The experiment is conducted at Politecnico di Milano.

The experimental setup for coherent synthesis of OPAs, summarized in the block diagram of Figure 3.16a, consists of (i) a WLC seed generation stage (ii) two
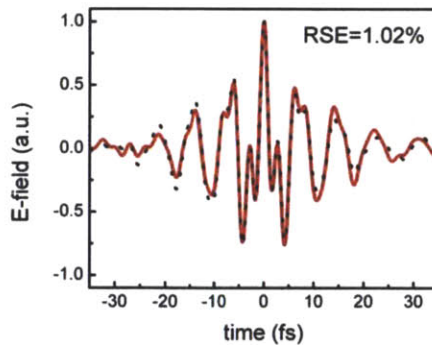

Figure 3.15 While the red solid line is the unperturbed waveform as shown in Figure 3.13c, the black dotted line is obtained by adding a CEP shift of π and a relative timing of 3.6 fs to the SWIR-OPCPA pulses. The waveform difference is comparable to a CEP jitter of 100 mrad.

broadband OPAs seeded by distinct portions of the WLC and (iii) coherent combination of their outputs. The system is powered by an amplified Ti:sapphire laser, providing 550-µJ, 130-fs pulses at 800 nm and 1 kHz. Since the WLC presents highly structured intensity and spectral phase profiles around the driving pulse wavelength, it is not possible to use the WLC directly generated by the fundamental frequency (FF) to seed the degenerate optical parametric amplifier (DOPA). Therefore an additional stage is necessary to shift the WLC driving wavelength to the infrared (IR), thus generating a well-behaved WLC around 800 nm [88]. This two-stage IR OPA, using type II BBO crystals, is pumped by the FF of Ti:sapphire and seeded by the WLC generated in a sapphire plate [89]. When pumped by 250-µJ pulses, this OPA provides a total signal + idler energy of 40 µJ. The IR OPA can produce idler pulses with passively stabilized CEP, exploiting the DFG process that occurs between pump and signal sharing the same CEP [82]. Both the signal and the CEP-stable idler can be used to generate the WLC [41]. For this experiment we use the signal at 1.3 µm to generate the WLC in a 3-mm-thick sapphire plate.

The short-wavelength portion of this seed ranges from 500 to 1000 nm (solid line in Figure 3.17a), and covers the gain range of the visible NOPA and SH-pumped DOPA (dashed lines in Figure 3.17a). We split the seed with a neutral-density ultrathin beam-splitter, and amplified the two replicas with the visible NOPA and the DOPA. Both OPAs were pumped by the SH from the remaining 300-µJ FF pulses; we used thick SH crystals to narrow the bandwidth of the SH pulse, facilitating its temporal overlap with the chirped WLC. In the visible NOPA
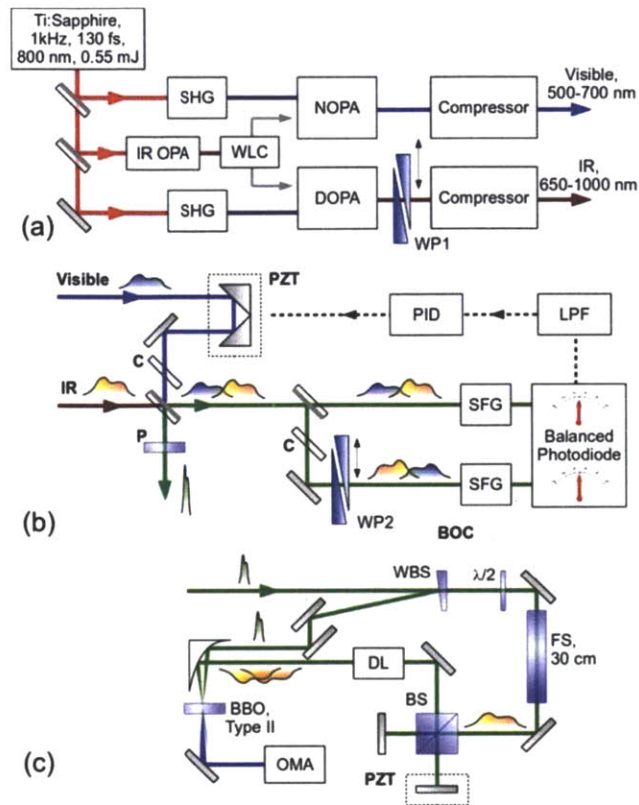
Figure 3.16 (a) setup for separate amplification, compression and synthesis of visible and infrared pulses: SHG: second harmonic generation; WP1: fused silica wedge plates for the tuning of the VIS-IR relative phase; (b) schematic of the BOC: PZT: piezo-electric actuator; WP2: CaF_2 wedge plates for delay tuning; P: 2-mm thick CaF_2 plate; C: compensation plates; LPF: electronic low-pass-filter; SFG: sum-frequency generation; (c) 2DSI schematic diagram: WBS: wedge beam splitter; DL: delay line.

we used a 1-mm-thick type-I BBO crystal cut at $\theta = 32°$ and an external pump-signal angle of ~6°, while in the DOPA we used a 1-mm-thick BBO with $\theta = 29°$ and a nearly collinear interaction; each OPA generates pulses with 1-2 µJ energy. To ensure spatial overlap of the collimated beams, we used the same focal lengths and propagated the beams for the same distances in the two OPAs. We compressed the two OPA outputs by broadband visible **[90]** and IR **[91]** chirped mirrors, which provided pulse durations close to the TL values (~7 fs for both OPAs). We then
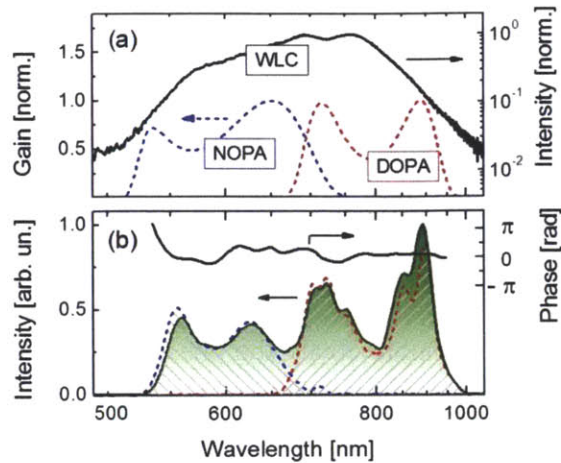
112

Figure 3.17 (a) Log scale: Spectrum of the gap-free WLC (solid line) generated in the sapphire plate, compared to the calculated gain of the visible and infrared OPAs (dashed lines, linear scale); (b) Linear scale: Spectra of the individual OPA pulses (dashed lines) and of the synthesized pulses. The spectral phase (solid black line) is deduced from the 2DSI measurement.

synchronized the two amplified pulses with a delay line equipped with a piezoelectric actuator (PZT), and collinearly combined them with an ultrathin metallic beam-splitter with spectrally flat 50:50 splitting ratio. A gap-free spectrum arising from the combination of the two pulses is shown on a linear scale in Figure 3.17b; it ranges from 520 to 1000 nm with very good spectral uniformity and supports a TL 3.65 fs pulse duration.

The last step of the pulse synthesis is the coherent combination of the two pulses, which calls for careful control of their relative delay and CEP. The relative CEP can be finely tuned by wedge pair WP_1. We detected the relative delay between the two pulses with the BOC sketched in Figure 3.16b, where two replicas of the synthesized pulse with opposite chirp are cross-correlated in 1-mm-thick BBO crystals, phase matched for SFG of 600-nm light from the NOPA and 800-nm light from the DOPA. Thanks to balanced detection, the BOC allows atto-second

precision relative timing measurement. We sent the low-pass filtered (<30Hz) BOC signal into a feedback loop based on a PID controller driving the PZT. The feedback locks the relative delay between the pulses, tuned by WP_2, with fluctuations below 30-as *r.m.s.* over a measurement time of 10 minutes, corresponding to less than 1/80th optical cycle (Figure 3.18). Since the two spectra have overlaps, we can double check the phase coherence by directly observing the linear spectral interference. Figure 3.19b is the closed-loop result, as opposed to the open-loop measurement shown in Figure 3.19a, and it is clear that the BOC-assisted feedback ensures the phase coherence.

Temporal characterization of the synthesized pulse was performed with 2DSI. 2DSI up-converts the pulse to be measured with two strongly chirped and time-delayed replicas, encoding the wavelength-dependent group-delay (GD) in the interference between the two temporally-overlapped up-converted pulses; thanks to its ultrabroad acceptance bandwidth and the avoidance of delay calibration, it is suited for the characterization of our octave-spanning pulses. Here the implementation of 2DSI is shown in Figure 3.16c; we chirp the IR portion of the spectrum and the 40-μm type II BBO up-conversion crystal guarantees a broad acceptance bandwidth along the ordinary axis. Figure 3.20a shows a 2DSI map of the whole synthesized spectrum and the retrieved wavelength-dependent group-delay, which is substantially flat over the whole pulse bandwidth; the residual group-delay oscillations in the visible spectral range are due to the large number of bounces on the chirped mirrors. The retrieved spectral phase, reported in Figure 3.17b, was applied to the measured spectral amplitude, giving the pulse shown in
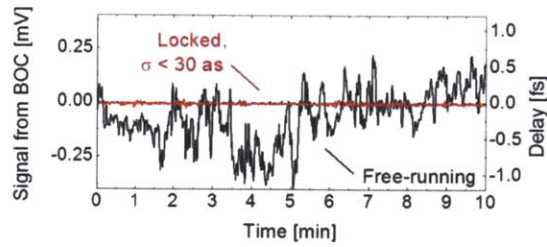
Figure 3.18 Relative pulse delay deduced from the BOC signal, measured in free-running and in closed feedback loop.
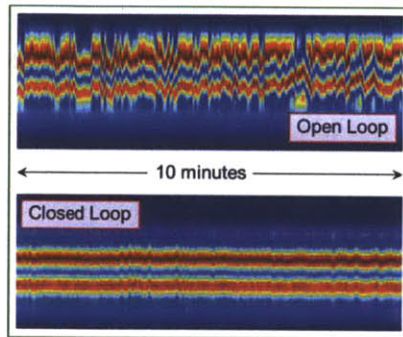
Figure 3.19 Since the two spectra have overlaps, the phase coherence can be double checked by directly observing the linear spectral interference.
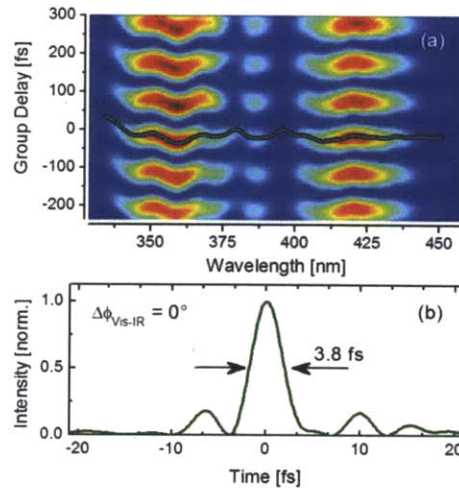
Figure 3.20 (a) 2DSI map and retrieved group delay; the signal arises from sum-frequency generation of the whole pulse with components at 900 nm; (b) intensity of the reconstructed pulse.

Figure 3.20b. The FWHM of its intensity profile is 3.8 fs, indicating that the pulse is compressed to within 4% of the TL duration. The good compression and the gap-

115

free, smooth synthesized spectrum concentrate 70 to 80% of the pulse energy in the main lobe, as opposed to 30 to 40% energy concentration in the other waveform synthesizer shown in the previous section.

3.4   Attosecond Pulse Generation

The synthesized waveforms are important for optimizing the HHG process, which is to date the only demonstrated technique for generating isolated atto-second pulses. Due to the inherent half-cycle symmetry of the HHG process, novel techniques like polarization gating [92], [93], two-color gating [94], [95], ionization gating [96], double optical gating [97], and ground-state depletion gating [98] are required to produce isolated atto-second pulses when the driving pulse duration is more than an optical cycle. These techniques open up the field of atto-second science, but the efficiency is fundamentally limited because energy outside the gating period is not used. Single-cycle and sub-cycle driving pulses can be used for generating the shortest and most intense isolated atto-second pulses with a given driving pulse energy. Moreover, by shaping the driving pulse one can control the spectral phase of the harmonics, as it was shown in a recent study [99], allowing more control for compressing the atto-second pulses.

As an example, we numerically solve the time-dependent Schrödinger equation (TDSE) for a helium atom in a strong laser field to illustrate a possible use of our source for driving direct isolated soft-x-ray pulse generation (Figure 3.21). The routine for solving TDSE is developed by Siddharth Bhardwaj, another graduate student in Professor Kärtner's group. The peak intensity of 6×10^{14} W/cm^2,

which can be reached with a beam diameter of 27 μm, is chosen such that the total ionization is below the critical ionization level in helium [59]. The transmission and dispersion of the Sn filter are taken from reference [100]. To gain more insight into the results given by the 3D TDSE simulation, we also calculated the ionization dynamics using the ADK formula (the blue curve in Figure 3.21a) and the classical electron trajectories (overlaid on top of the spectrogram in Figure 3.21b). Electron trajectories from three ionization events, which are labeled by numbers, are calculated and those trajectories that return to the ionized atom are shown in Figure 3.21b. For visualization, electrons ionized by the electric field with strength weaker than half of the maximum are neglected since they have negligible contribution to the HHG emission, as confirmed by the TDSE simulation.

The dipole approximation is used in describing the light-atom interaction both for the trajectory calculation and for solving the TDSE. Under the single-active electron approximation, the 3D TDSE is solved numerically with an asymptotic behavior correspondence discretization of the Hamiltonian [101]. The atomic potential of helium is modeled as described in reference [102], and we optimize the coefficients for agreement between the calculated and measured ionization energies for helium. The dipole acceleration, and hence the HHG radiation, is then evaluated using the Ehrenfest theorem. The spectrogram (Figure 3.21b) is calculated using a short-time Fourier transform with a Gaussian windowing function of 58 as (FWHM).

With choice of CEPs as in Figure 3.21a, substantial ionization is limited to one optical half-cycle and an isolated soft-x-ray pulse spanning over 250 eV is
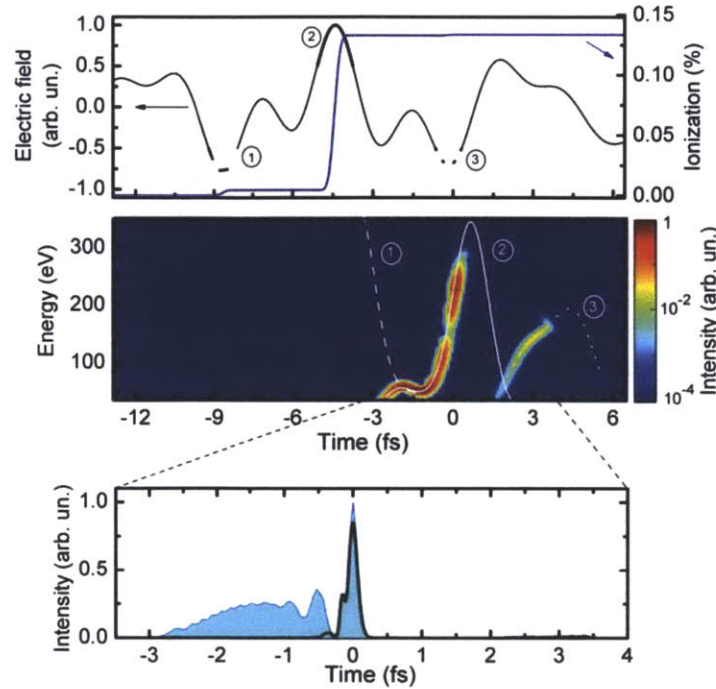
Figure 3.21 TDSE simulation results of the single-atom HHG with the synthesized waveforms. (a) Ionization dynamics (blue) induced in helium by a linearly polarized electric-field waveform (black) assuming a peak intensity of 6×10^{14} W/cm^2, ϕ_1=960 mrad, and ϕ_2=-440 mrad. (b) Spectrogram of the HHG superimposed with the calculated classical trajectories. Returning trajectories from three ionization events (2: the main pulse; 1 and 3: the satellite pulses) are shown for clear interpretation of the spectrogram. The synthesized pulse isolates the ionization process to a half optical cycle and a continuum spectrum spanning more than 250eV can be achieved. The isolated soft x-ray pulse has the same sign of chirp over 80% of the spectrum and so the compression setup can be simplified. (c) The isolated soft x-ray pulse plotted in the time domain before (blue) and after (black line) a 100-nm thick Sn filter. The Sn filter is chosen for its capability to block the strong IR driving field and the nonlinearly chirped low-photon energy spectral content, and its good transmission in the soft x-ray range. The filtered isolated soft x-ray pulse has a FWHM duration of 150 as.

generated (Figure 3.21b and 3.21c) without the need for gating techniques or spectral filtering which typically limit the efficiency and the obtainable bandwidth. Using an additional Sn filter, which blocks the strong IR driving field and the nonlinearly chirped low-photon-energy spectral content below 70 eV, leads to an

isolated 150-as pulse centered at 200 eV. Of note, the non-sinusoidal electric-field waveform leads to drastically changed electron trajectories (compared to those from a sinusoidal driving field) resulting in corresponding changes in quantum diffusion and atto-chirp, which can be controlled by means of the waveform synthesis parameters (ϕ_1, ϕ_2, and Δt).

In HHG, quantum diffusion and ionization rate are two competing factors in determining the ratio between radiation from long and short electron trajectories. While quantum diffusion always favors the short trajectories, when the HHG process is driven by conventional sinusoidal electric-field waveforms, the stronger ionization rate for the long trajectories results in significant radiation from electrons of both trajectories. For the example shown in Figure 3.21b, where a sub-cycle waveform is used, the difference in travel time between long and short trajectories is increased. In addition, the ionization contribution to short trajectory radiation is boosted. Overall, quantum diffusion dominates over ionization rate and effectively eliminates the radiation from long trajectories, resulting in isolated soft x-ray pulse generation solely from short trajectories. This gives an example of the capability of our light source to simultaneously isolate the ionization process and manipulate electron trajectories within an optical cycle, allowing unprecedented control of the HHG process.

3.5   Grism design

For many strong-field applications, a long-term beam pointing stability is necessary. While the beam pointing can be actively stabilized by a camera-assisted
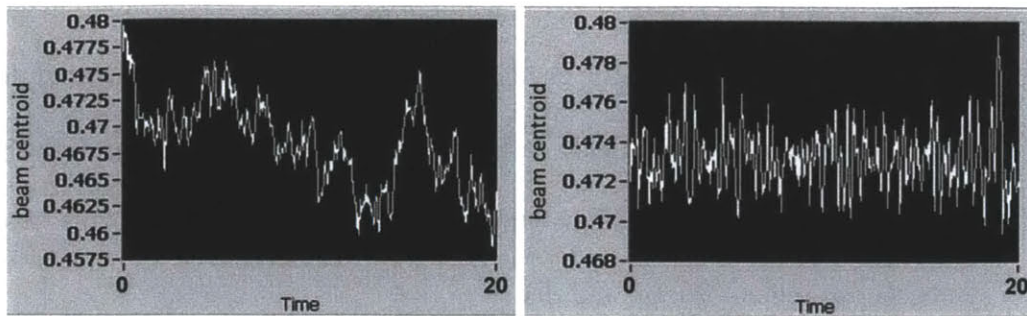
119

Figure 3.22 Beam pointing can be actively stabilized by a camera-assisted computer feedback control.

computer feedback control (Figure 3.22), it is still worthwhile to put efforts into a new stretcher design which can significantly reduce the overall NIR-OPCPA path-length. It is recently demonstrated that a grism pair is an easy-to-align and compact stretcher that can support >300nm bandwidth of an NIR-OPCPA **[103]**. Compared to a prism stretcher, the grism stretcher can be made with a path-length more than an order of magnitude shorter.

Figure 3.23 shows the design of our homemade grism stretcher, which consists of a combined gold-coated grating (200g/mm) and a BK7 glass prism. By using this grating/prism combination with 1-mm spacing between elements, we are able to obtain a custom grism optic while avoiding the difficulties in manufacturing a grism with the grating etched directly onto the face of a prism. The advantage of using a grism pair rather than a prism pair is a huge increase in compactness. Likewise, we will also replace the grating stretcher between the two OPA stages with a grism pair of the same design.

The dispersion from a grism stretcher can be calculated analytically from ray-tracing as follows:

grating (200 gpmm)

N-BK7 prism

$\alpha = 20deg$

$d_g = 1mm$

$e_i = 3mm$
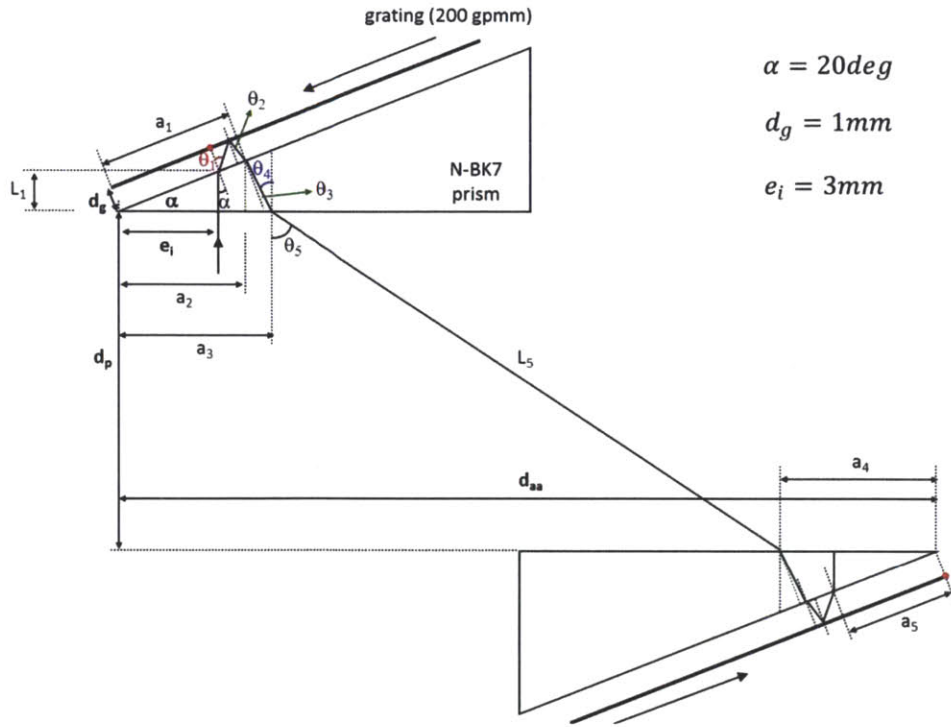
Figure 3.23 Design of the grism pairs used to achieve compact stretching. The design pairs a 200g/mm grating with a BK7 glass prism, separated by 1 mm.

$$
\begin{cases}
\theta_1 = sin^{-1}[nsin(\alpha)] & Eq.\,3.4a \\
\theta_2 = sin^{-1}\left[sin(\theta_1) - \frac{\lambda}{\Lambda}\right] & Eq.\,3.4b \\
\theta_3 = sin^{-1}\left[\frac{sin(\theta_2)}{n}\right] & Eq.\,3.4c \\
\theta_4 = \alpha + \theta_3 & Eq.\,3.4d \\
\theta_5 = sin^{-1}[nsin(\theta_4)] & Eq.\,3.4e
\end{cases}
$$

$$
\begin{cases}
L_1 = e_i tan(\alpha) & Eq.\,3.5a \\
L_2 = \dfrac{d_g}{cos(\theta_1)} & Eq.\,3.5b \\
L_3 = \dfrac{d_g}{cos(\theta_2)} & Eq.\,3.5c
\end{cases}
$$

$$
\begin{cases}
a_1 = \dfrac{e_i}{cos(\alpha)} + L_2 sin(\theta_1) + L_3 sin(\theta_2) & Eq.\,3.5d \\
L_4 = a_1 \dfrac{sin(\alpha)}{cos(\theta_4)} & Eq.\,3.5e \\
L_5 = \dfrac{d_p}{cos(\theta_5)} & Eq.\,3.5f
\end{cases}
$$

121

$$\begin{cases} a_2 = a_1 cos(\alpha) & Eq.\,3.5g \\ a_3 = a_2 + L_4 sin(\theta_4) & Eq.\,3.5h \\ a_4 = d_{aa} - a_3 - L_5 sin(\theta_5) & Eq.\,3.5i \end{cases}$$

$$\begin{cases} L_6 = a_4 \dfrac{sin(\alpha)}{cos(\theta_3)} & Eq.\,3.5j \\[2ex] L_7 = \dfrac{d_g}{cos(\theta_2)} & Eq.\,3.5k \\[2ex] L_8 = \dfrac{d_g}{cos(\theta_1)} & Eq.\,3.5l \end{cases}$$

$$\begin{cases} a_5 = a_4 cos(\alpha) - L_6 sin(\theta_3) - L_7 sin(\theta_2) - L_8 sin(\theta_1) & Eq.\,3.5m \\ L_9 = a_5 sin(\alpha) & Eq.\,3.5n \end{cases}$$

The spectral phase from propagation (double-pass) is

$$\phi_{prop} = 2\left[\frac{2\pi}{\lambda}(L_2 + L_3 + L_5 + L_7 + L_8) + \frac{2\pi n}{\lambda}(L_1 + L_4 + L_6 + L_9)\right] \qquad Eq.\,3.6$$

The phase imparted by the gratings are

$$\begin{cases} \phi_{G1} = 2\left[-\dfrac{2\pi}{\Lambda}L_2 sin(\theta_1)\right] & Eq.\,3.7a \\[2ex] \phi_{G2} = 2\left[-\dfrac{2\pi}{\Lambda}[a_5 + L_8 sin(\theta_1)]\right] & Eq.\,3.7b \end{cases}$$

The total phase is

$$\phi(\omega) = \phi_{prop}(\omega) + \phi_{G1}(\omega) + \phi_{G2}(\omega) \qquad Eq.\,3.8$$

The dispersion can then be calculated from the derivatives of the total phase at the center frequency ω_c.

3.6   Two-dimensional spectral shearing interferometry

Interference is the most widely used technique to measure the difference of the optical phases between two waves. Thus, if one has a reference pulse with a well-known spectral phase, it is natural to characterize the spectral phase of the
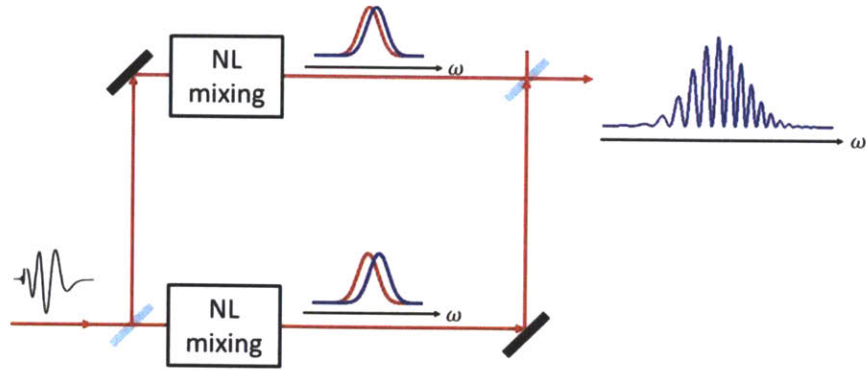
Figure 3.24 Principle of the SPIDER pulse characterization technique.

pulse under test by measuring the spectral interference between the pulse under test and the reference pulse. However, such a reference pulse is usually, if not always, unavailable. Spectral phase interferometry for direct electric-field reconstruction (SPIDER) is a technique developed to solve the problem of unavailable reference pulse [86]. The idea is generate two up-converted spectra slightly shifted in frequency and investigate the spectral interference of these two copies. Figure 3.24 shows the operation principle of SPIDER. The pulse under test is first split into two replicas by a beamsplitter. Both replicas undergo nonlinear mixing such that the optical frequencies are up-shifted to ω from ω-δ and ω-δ-Ω, respectively. Ω is referred to as the spectral shear between the two replicas. The two replicas are then combined with a slightly delay τ between the two replicas and directed into a spectrometer. The spectrum can be expressed as [104]:

$$S(\omega) = \left| A_R(\omega - \delta)e^{j(\varphi(\omega-\delta)+\varphi_\delta)} + A_S(\omega - \delta - \Omega)e^{j(\omega\tau+\varphi(\omega-\delta-\Omega)+\varphi_{\delta+\Omega})} \right|^2 =$$

$$S_{DC}(\omega) + S^+(\omega)e^{-j\omega\tau} + S^-(\omega)e^{j\omega\tau} \qquad\qquad Eq.\,3.9$$

When the delay τ is sufficiently large, $S^+(\omega)e^{-j\omega\tau}$ can be isolated from the other two terms and its phase can be determined unambiguously [104]:

$$\varphi(\omega) = [\varphi(\omega - \delta) - \varphi(\omega - \delta - \Omega)] - \omega\tau + (\varphi_\delta - \varphi_{\delta+\Omega})$$

$$\cong GD(\omega - \delta - \Omega/2) \cdot \Omega - \omega\tau + (\varphi_\delta - \varphi_{\delta+\Omega}) \qquad Eq. 3.10$$

where the third term is a constant phase introduced during the nonlinear mixing. If the delay τ is characterized with high precision, the linear phase $\omega\tau$ can be subtracted off and then we are left with the information of the wavelength-dependent group-delay, which is sufficient to determine the pulse envelope.

The subtraction of $\omega\tau$ is key to successful reconstruction of the spectral group-delay. As shown in reference [105], an error in determining the delay, $\delta\tau$, will result in a relative error in the measured pulse width, $\frac{\delta T}{T} \approx \frac{\omega_{FWHM}{}^2}{2\Omega} \delta\tau$. The relative error scales quadratically with the bandwidth in an optical system. Such a catastrophic scaling makes the delay calibration increasingly hard for measurements of single-cycle or sub-cycle pulses.

2DSI is developed to eliminate such a hard calibration task. As shown in Figure 3.12, there is no delay between the two spectrally shifted replicas of the pulse under test and thus no spectral interference is present. Rather, the group-delay at each wavelength is encoded in the phase of the interference fringes along a wavelength independent axis, created by scanning the relative phase between the two spectrally shifted replicas (ϕ_{gd}). Thus, 2DSI is free from the challenge of calibrating interferometer delay. Furthermore, creating a wavelength independent dimension for the interference means that the fringes are purely sinusoidal and thus a simple algorithm such as a single-term harmonic inversion can be implemented to reconstruct the wavelength-dependent group-delay.
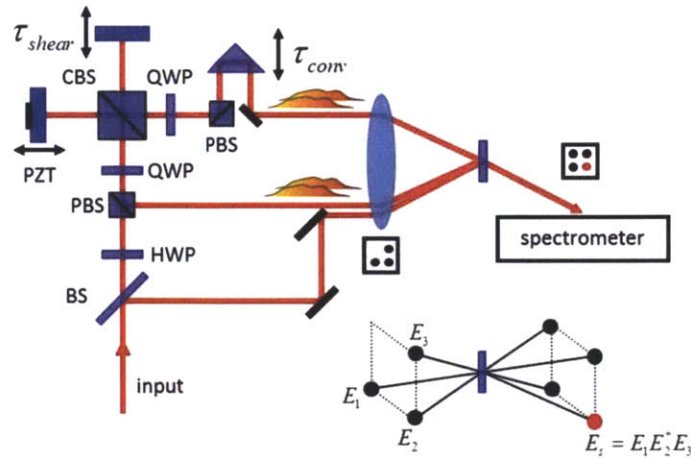
Figure 3.25 Scheme of the TG-2DSI.

The non-linear mixing used in the current 2DSIs is sum-frequency generation (SFG), which up-convert the optical frequencies from NIR and SWIR to NUV to visible. While such a $\chi^{(2)}$ process certainly offer a high sensitivity compared to higher-order processes, their application to UV and visible pulse characterization is limited since the up-converted optical frequencies are above the response range of a silicon detector. In the following paragraphs, a 2DSI based on transient grating (TG), a $\chi^{(3)}$ process which can either up-convert or down-convert the optical frequencies, is presented.

Figure 3.25 shows the schematics of the TG-2DSI. The pulse under test is first split by a beam sampler whose second surface is anti-reflection coated. A part of the beam is Fresnel reflected and only guided via silver mirrors before being mixed with the other parts. The transmitted part of the beam is highly stretched before its polarization is rotated by 90° via a half waveplate (HWP). It then goes through a polarization beamsplitter (PBS) and a quarter waveplate (QWP) before being split again by a cube beamsplitter (CBS). The back-reflected beams go
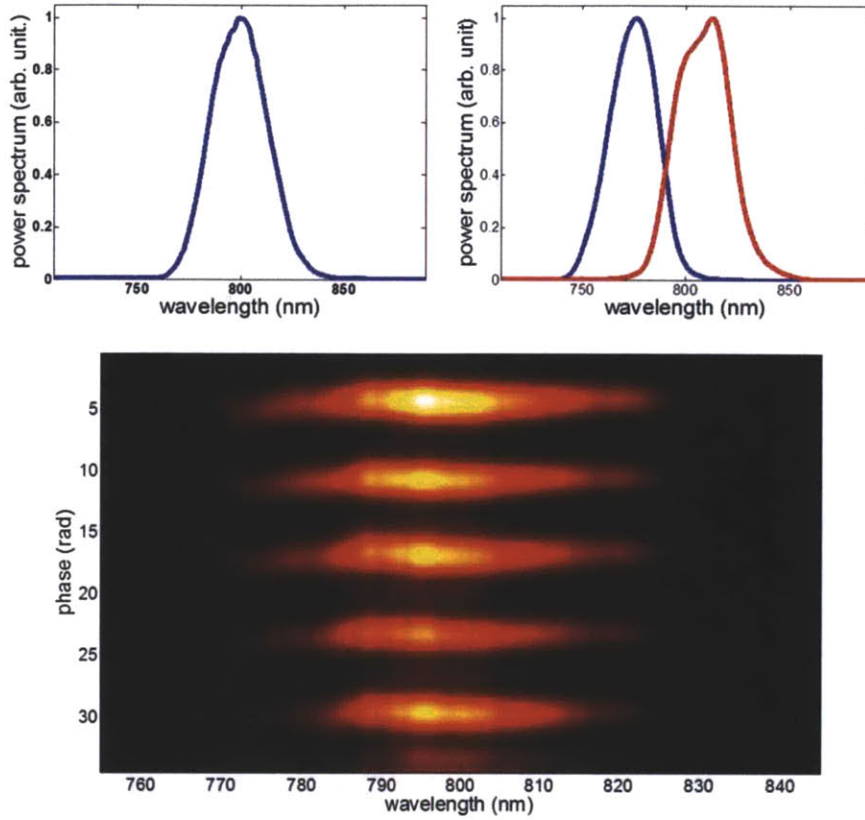
Figure 3.26 (a) The fundamental spectrum of a Ti:sapphire regenerative amplifier. (b) The frequency of the TG signal can be either up-converted or down-converted. (c) The raw TG-2DSI data.

through the same QWP and get reflected by the same PBS. The TG is arranged in a folded BOXCAR arrangement commonly used in four-wave-mixing spectroscopy experiments [106]. The three beams are collimated and parallel with one another before being focused by a concave mirror and interacted at the focus in a 250-μm fused silica coverslip. The signal will emerge on the other edge of the BOXCAR and it has the form $E^{TG} = (E_1 E_2^*)E_3$. E_1 and E_2 are both highly chirped and thus we can express them as

$$E_1 = e^{j\delta_1 t} + e^{j(\delta_1 + \Omega)t} e^{j\phi_m} \qquad Eq.\,3.11a$$

$$E_2 = e^{j\delta_2 t} + e^{j(\delta_2 + \Omega)t} e^{j\phi_m} \qquad Eq.\,3.11b$$

and

$$(E_1 E_2^*) = 2e^{j\delta t} + e^{j(\delta - \Omega)t}e^{-j\phi_m} + e^{j(\delta + \Omega)t}e^{j\phi_m} \qquad Eq.\,3.12$$

where ϕ_m is the phase modulation by the PZT, Ω is the shear frequency, and $\delta = \delta_1 - \delta_2$ is the converted frequency. Of note, δ can be either positive or negative depending on τ_{conv}. As demonstrated in Figure 3.26b, the frequency of the TG signal can be either up-converted or down-converted. The two-dimensional intensity plot can be expressed as

$$I^{TG}(\omega, \phi_m) = 6S(\omega)$$

$$+ 8S(\omega)\cos\left[\phi(\omega) - \frac{\phi(\omega - \Omega) + \phi(\omega + \Omega)}{2}\right]\cos[\phi_m - GD(\omega)\Omega]$$

$$+ 2S(\omega)\cos[2\phi_m + 2GD(\omega)\Omega] \qquad Eq.\,3.13$$

Isolating the second term for the others, we reach a two-dimensional intensity plot very similar to the typical 2DSI result.

$$I^{TG}(\omega, \phi_m) \propto \cos\left[\phi(\omega) - \frac{\phi(\omega - \Omega) + \phi(\omega + \Omega)}{2}\right]\cos[\phi_m$$

$$- GD(\omega)\Omega] \qquad Eq.\,3.14$$

where $\cos[\phi(\omega) - \phi(\omega - \Omega) + \phi(\omega + \Omega)/2]$ is the spectral amplitude modulation. Since the information of spectral group-delay is encoded in the other wavelength independent axis, such spectral amplitude modulation does not influence the reconstruction of the wavelength-dependent group-delay. Besides, Ω is small for most cases, $\phi(\omega) \cong \phi(\omega - \Omega) + \phi(\omega + \Omega)/2$ and thus there is only minor spectral amplitude modulation.

Figure 3.26c is the raw data measuring our 35-fs Ti:sapphire CPA pulses. To verify the accuracy of the TG-2DSI, the pulse is measured, with TG-2DSI used
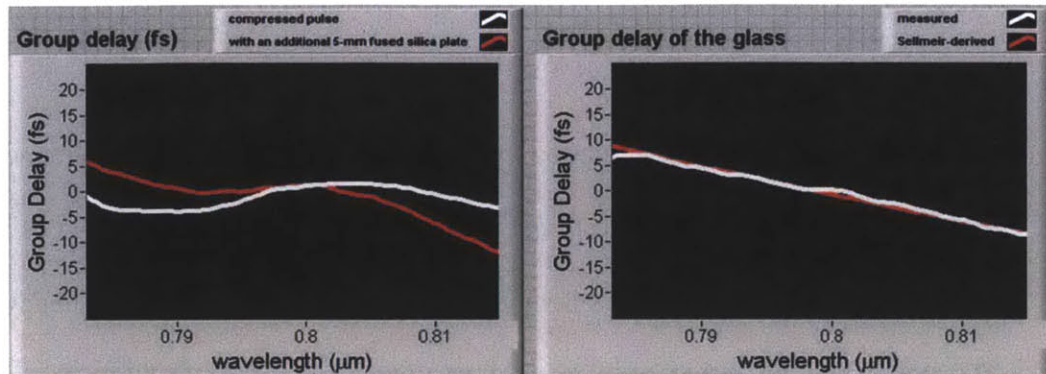
Figure 3.27 To verify the accuracy of the TG-2DSI, the pulse is measured, with TG-2DSI used both before and after dispersion by a 5 mm fused-silica plate. (a) plots the extracted wavelength-dependent group-delay of the compressed pulse (white line) and the dispersed pulse (red line). The measured wavelength-dependent group-delay well matches the Sellmeier predicted curve, as shown in (b).

both before and after dispersion by a 5 mm fused-silica plate. Figure 3.27a plots the extracted wavelength-dependent group-delay of the compressed pulse (white line) and the dispersed pulse (red line). The measured spectral group-delay well matches the Sellmeier predicted curve, as shown in Figure 3.27b.

3.7   Broadband non-collinear optical parametric amplification without angularly dispersed idler

Broadband mid-IR sources have been an integral part of time-resolved vibrational spectroscopies because this wavelength range is in resonance with vibrational transitions of important bio-molecules such as O-H stretching [107] and C-O stretching [108]. Recently, there also has been interest in applying mid-IR sources to strong-field physics research such as the study of photoionization processes [109] and long-wavelength driven HHG [57], [110], [111].
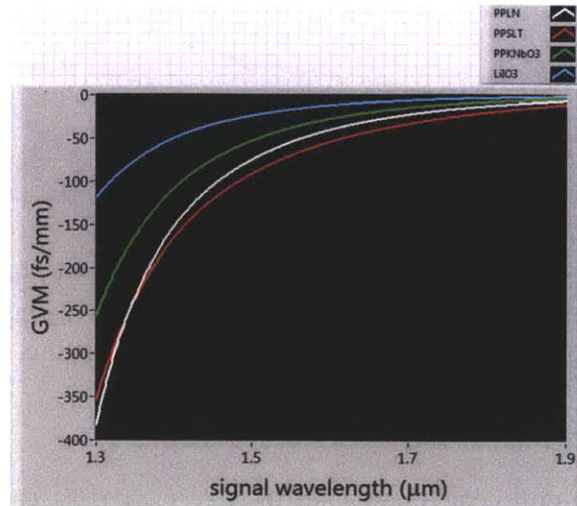
Figure 3.28 GVM of several mid-IR nonlinear crystals.

Due to the lack of mid-IR laser media, DFG or OPA has been largely employed to down-convert visible or near-IR light sources [112–114]. It has been shown that mid-IR crystals such as $LiIO_3$, $KNbO_3$, and $MgO:LiNbO_3$ have group-velocity matched wavelengths, when pumped at 800nm, between 950nm and 1050nm and thus allow the direct generation of broadband mid-IR idler with spectra supporting three-cycle pulses [112]. For wavelengths where signal and idler group velocities (V_{gs} and V_{gi}) are not matched, a non-collinear geometry can sometimes be employed to achieve broad phase-matching bandwidth, at the cost of introducing idler angular dispersion [115]. Once its angular dispersion is compensated, it has been shown that the idler can also be utilized for experiments [116].

However, when pumped at 1μm, such mid-IR crystals only possess matched group velocities at the degenerate wavelengths. Even worse, the signal group velocities are higher than those of the idler (Figure 3.28) and the condition of the
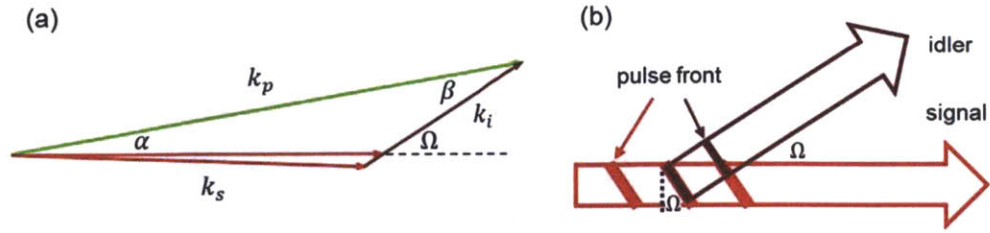
Figure 3.29 (a) Schematic of the OPA geometry. (b) Interpretation of Equation 3.17. The signal and the idler will stay effectively overlapped when Eq. 3.17a is fulfilled. The idler will have no pulse front tilting, and thus no angular dispersion, if Eq. 3.17b is satisfied.

traditional non-collinear OPA, i.e. $V_{gs} = V_{gi} \cos\Omega$, cannot be satisfied. Thus broadband amplification is not achievable. On the other hand, pumping at 1µm is advantageous for power and energy scalability because it is compatible with high-power Ytterbium (Yb) fiber technology and high-energy Yb:YAG laser technology.

In this section, we present a new scheme for direct generation of broadband, angular-dispersion-free mid-IR idler pulses when signal-idler group velocity matching cannot be achieved and the traditional non-collinear geometry fails to increase the phase-matching bandwidth. The conditions for broadband amplification and absence of idler angular dispersion can be fulfilled simultaneously by introducing not only non-collinear geometry but also signal angular dispersion. A broadband (1.8-2.4µm), angular-dispersion-free idler pulse, designed to seed our SWIR-OPCPA, is demonstrated. Furthermore, we identify the potential of the scheme to generate sub-2-cycle, 3.5µm idler pulses, more than a factor of 2 shorter than the current state-of-the-art **[113]**, **[114]**. The scheme may also find applications in high-energy waveform synthesis because one may employ a NIR-OPCPA until the final power amplification stage where the light is converted

to longer wavelengths via our scheme. The minimized uncommon path simplifies the required feedback loops and increases the stability of the system.

Figure 3.29 shows the principle of the scheme and defines the angles α, β, and Ω between interacting wave-vectors k_s, k_i, and k_p. To obtain a broadband amplification, not only the wave-vector mismatch but also its derivative with respective to the signal optical frequency has to be set to zero as shown in Eqs. 3.15 and 3.16.

$$\begin{cases} \Delta k_{\parallel} = k_p cos\beta - k_i - k_s cos\Omega = 0 & Eq.\,3.15a \\ \Delta k_{\perp} = k_p sin\beta - k_s sin\Omega = 0 & Eq.\,3.15b \end{cases}$$

$$\begin{cases} k_p sin\beta \dfrac{d\beta}{d\omega_s} + \dfrac{dk_i}{d\omega_s} + \dfrac{dk_s}{d\omega_s} cos\Omega - k_s sin\Omega \dfrac{d\Omega}{d\omega_s} = 0 & Eq.\,3.16a \\ k_p cos\beta \dfrac{d\beta}{d\omega_s} - \dfrac{dk_s}{d\omega_s} sin\Omega - k_s cos\Omega \dfrac{d\Omega}{d\omega_s} = 0 & Eq.\,3.16b \end{cases}$$

With some algebraic manipulations and the constraint that the idler has no angular dispersion, i.e. $d\beta/d\omega = 0$, one can reach Eq. 3.17, which determines the required non-collinear angle and signal angular dispersion ($d\alpha/d\lambda$) for simultaneous broad phase-matching bandwidth and angular-dispersion-free idler.

$$\begin{cases} V_{gi} = V_{gs} cos\Omega & Eq.\,3.17a \\ tan\Omega = \lambda_s \dfrac{V_{gs}}{V_{ps}} \dfrac{d\alpha}{d\lambda} & Eq.\,3.17b \end{cases}$$

, where Vps is the signal phase velocity.

The interpretation of Eq. 3.17 is depicted in Figure 3.29b. Eq. 3.17a means that the required signal-idler angle is the one that makes the idler group velocity equal to the projection of the signal group velocity along the idler propagation direction. Of note, the relation between V_{gs} and V_{gi} is inverse to that of a traditional non-collinear OPA. Eq. 3.17b means that the signal pulse front has to be tilted to
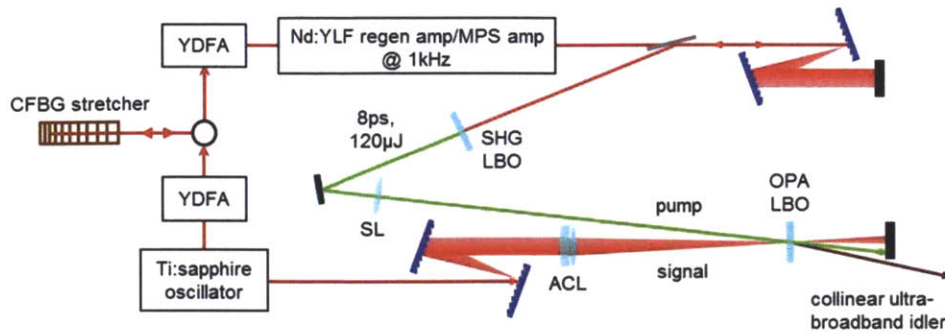
Figure 3.30 Schematic diagram of the experimental setup. YDFA: Ytterbium-doped fiber amplifier; CFBG: chirped fiber Bragg grating; MPS amp: multi-pass slab amplifier.

the idler propagation direction. The idler, when pumped by a picosecond pulse where its physical length is larger than its beam diameter, will simply acquire a pulse front that matches the signal pulse front **[117]**. If the signal pulse front is tilted to the idler propagation direction, the generated idler will possess no pulse-front tilting, that is, no angular dispersion **[117]**. It is slightly more complicated when a femto-second pump pulse is used since pump pulse-front tilting is also needed to keep the idler free from angular dispersion.

To demonstrate the idea, we built a single-stage OPCPA generating broadband, angular-dispersion-free 2.15μm idler pulses. In this example, $V_{gs} > V_{gi}$ and thus neither collinear geometry nor traditional non-collinear geometry can be used to achieve broad phase-matching bandwidth. Figure 3.30 shows the schematic diagram of the setup. It starts with an octave-spanning Ti:sapphire oscillator (Idesta QE). A 1-kHz Nd:YLF chirped pulse amplifier (CPA) **[118]** was injection-seeded by the 1047-nm spectral component of the oscillator for the optical synchronization. A small fraction of the Nd:YLF CPA output was used to generate the 8-ps, 120-μJ,
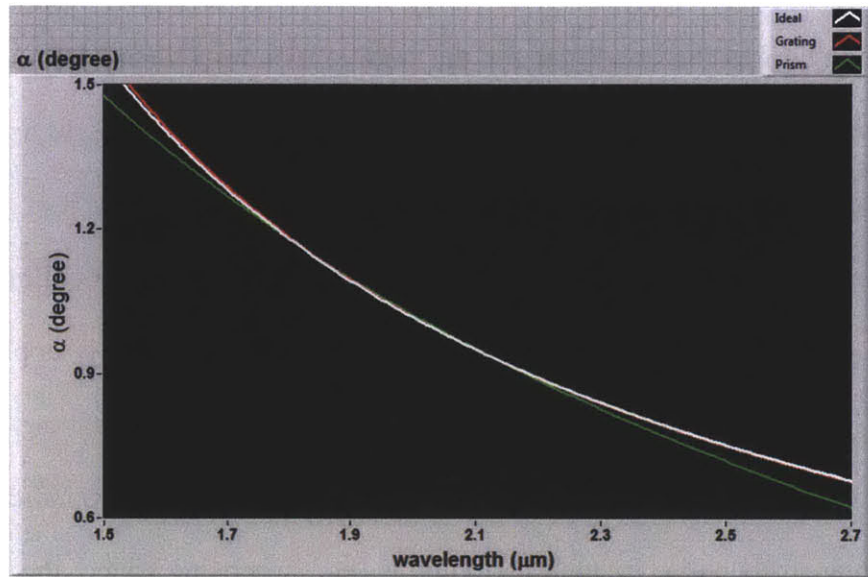
Figure 3.31 (white line) Signal angular dispersion required to make the idler perfectly free from angular dispersion. (red line) Signal angular dispersion introduced by a grating pair matches the requirement over a bandwidth of >1μm. (green line) Signal angular dispersion introduced by a prism pair.

523-nm pump pulses by second-harmonic generation in a lithium triborate (LBO) crystal. The remaining oscillator output was spatially chirped by a grating pair before being focused by an achromatic lens (ACL). The grating separation determines the angular dispersion applied to the signal. A Brewster prism pair can also be used to introduce the required angular dispersion, but the performance is inferior because it gives too much higher order dispersion compared to typical material dispersion (Figure 3.31). The available signal pulse energy for seeding the OPCPA was 0.25 nJ. A single-stage OPCPA with a gain of 2,000 is constructed using a 10-mm type-I LBO crystal.

Figure 3.32 presents the far-field idler spectra. Three spectra taken at different transverse positions of the beam are shown for each experimental condition. The baseline result, obtained with $\alpha = 1.0^o$ and $d\alpha/d\lambda = 0$, is shown in

Figure 3.32a. As expected, the amplification bandwidth is narrow because there is no solution to the condition for the traditional non-collinear OPA. Figure 3.32b shows the result when the signal angular dispersion was properly applied, but the non-collinear angle was not set correctly (α = 1.6^o and $d\alpha/d\lambda$ = 100µrad/nm). Figure 3.32c, on the other hand, shows the result when the non-collinear angle was set correctly, but the signal angular dispersion was not properly applied (α = 1.0^o and $d\alpha/d\lambda$ = 64µrad/nm). In either condition, the amplification bandwidth is increased compared to Figure 3.32a. However, the spatial chirp indicates that idler angular dispersion is present. This is not surprising since the condition of broadband amplification (Eq. 3.16) can still hold if one would allow idler angular dispersion ($d\beta/d\omega \neq 0$). In fact, it has been previously shown that an angularly dispersed signal can be employed to extend the phase-matching bandwidth of a NIR-OPCPA [119], [120]. However, it is only when both conditions in Eq. 3.17 are fulfilled (α = 1.0^o and $d\alpha/d\lambda$ = 100µrad/nm) that one can obtain a broadband, angular-dispersion-free idler as illustrated in Figure 3.32d. The centroid of the spectra remains the same across the beam, showing no measurable angular dispersion. The inset shows the far-field beam profile, showing low beam ellipticity of less than 1.1.

The generated broadband, angular-dispersion-free idler can be used for the seeding of our SWIR-OPCPA for long-wavelength driven HHG. Generally, the weak seed, a few pJ, limits the amplified output energy of the current 2.15µm OPCPA because of the pump depletion by super-fluorescence [118], [121]. It has been a recent endeavor to improve the 2-µm seed power [56], [122]. Starting with
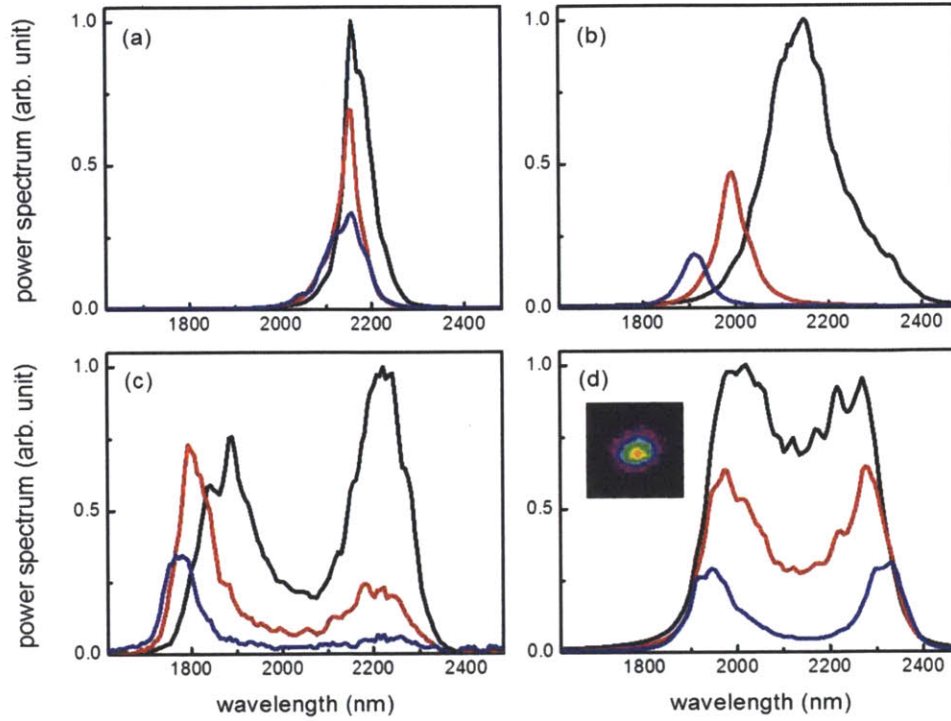
Figure 3.32 Far-field idler spectra measured at different transverse positions of the beam (black, red, and blue) under different experimental conditions. (a) $\alpha = 1.0^\circ$ and $d\alpha/d\lambda = 0$. (b) $\alpha = 1.6^\circ$ and $d\alpha/d\lambda = 100\mu rad/nm$. (c) $\alpha = 1.0^\circ$ and $d\alpha/d\lambda = 64\mu rad/nm$. (d) $\alpha = 1.0^\circ$ and $d\alpha/d\lambda = 100\mu rad/nm$. Inset: the far-field beam profile.

the scheme shown here, the effective seed has a photon number equal to the phase-matched signal band of the Ti:sapphire oscillator (nJ-level energy), and thus the initial signal-to-noise ratio is improved by two orders of magnitude [123].

Figure 3.33 shows another example of our scheme, applied to the 3-5µm regime. Applying the local approximation, we have used the elliptic function analytic formulas for describing the gain of an OPCPA [124], [125]. The parameters used in the calculation were: $\lambda_p = 1030nm$, $I_p = 20GW/cm^2$, and $\lambda_s = 1250-1850nm$. In a 1mm periodically poled lithium niobate crystal with a poling period of 22.8µm, Eq. 3.17 can be satisfied by setting $\alpha = 4.1^o$ and $d\alpha/d\lambda =$

145μrad/nm. The whole system is compatible with Yb fiber technology or Yb:YAG laser technology as the signal can also be generated by super-continuum generation in a photonic crystal fiber [126]. The calculation shows that a bandwidth of 43 THz (-10dB) centered at 3.5μm can be obtained with a negligible angular dispersion (200μrad across the full amplification bandwidth). The transform-limited pulse duration of such a bandwidth is 19fs (1.6cycle), more than a factor of 2 shorter than the state-of-the-art 3-5μm OPCPA pulses, pumped at 1μm [113], [114].
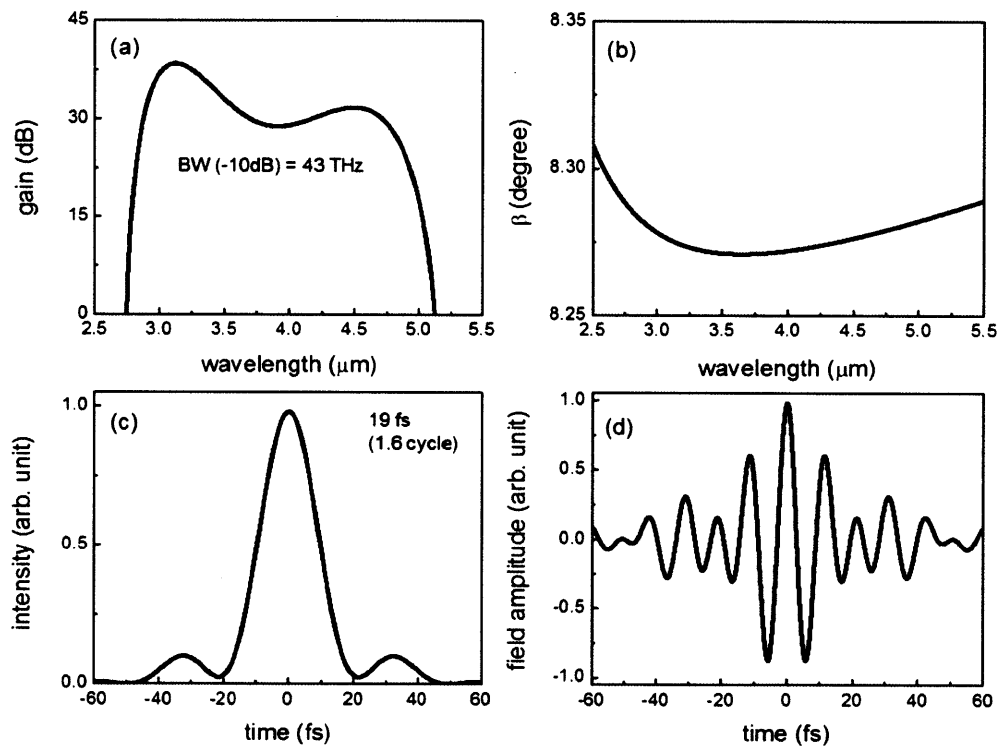
Figure 3.33 The simulation results of an OPCPA utilizing the proposed concept. A bandwidth close to an octave, centered at 3.5μm, can be obtained (a) with negligible angular dispersion (b). Such a bandwidth supports a 1.6 cycle, 19fs, pulse (c) with an electric-field waveform as shown in (d).

In conclusion, we present a new type of non-collinear OPA for direct generation of broadband, angular-dispersion-free mid-IR idler pulses. A broadband

(1.8-2.4μm), angular-dispersion-free idler pulse, designed to seed our SWIR-OPCPA, was generated as an experimental demonstration. A calculation shows that the scheme can generate a 19fs (1.6cycle), 3.5μm idler pulse, a promising source for time-resolved vibrational spectroscopies. The scheme may also find applications in high-energy waveform synthesis because one may employ a NIR-OPCPA until the final power amplification stage where the light is converted to longer wavelengths via our scheme. The minimized uncommon path simplifies the required feedback loops and increases the stability of the system.

THIS PAGE IS INTENTIONALLY LEFT BLANK

Chapter 4

Conclusion

In conclusion, we have presented in this thesis the theory, optimization, and experimental results of broadband OPCPAs at different spectral ranges. Furthermore, we have demonstrated prototype high-energy sub-cycle waveform synthesizers based on the coherent wavelength multiplexing of broadband OPAs/OPCPAs. The approach can be generalized to a system of N OPCPAs resulting in peak-power scaling of the output by N^2. Such laser systems constitute a novel optical tool for atto-second control of strong-field physics experiments and for energy and bandwidth scaling of few- or sub-cycle high-energy optical sources in general. Work such as the TG-2DSI and the new NOPA which might benefit the construction of a large-scale waveform synthesizer is also reported.

In the later two sections, two ongoing projects on pulse characterization techniques are presented.

4.1   Spatio-temporal pulse characterization

Just like all other nonlinear processes, spatial properties of the driving laser field also play an important role if one wants to achieve efficient HHG. Besides, spatio-temporal dynamics become increasingly important as the driving laser pulse duration approaches single- or sub-cycle. Thus we are extending the capability of the 2DSI to the full spatio-temporal pulse characterization. Due to the collinear
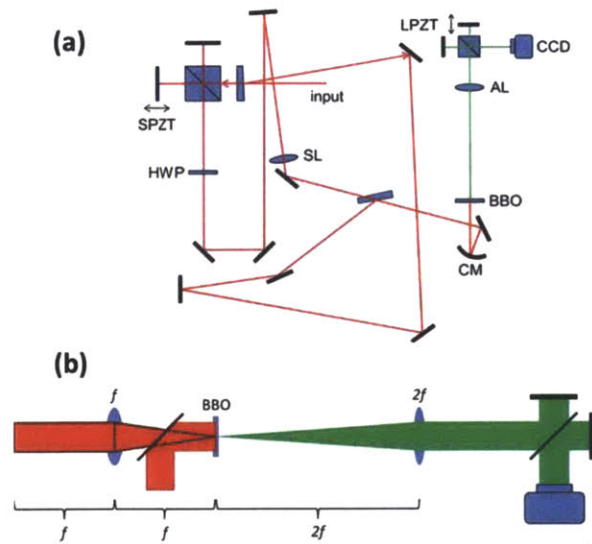
Figure 4.1 (a) Scheme of the 4DSI for the spatio-temporal pulse characterization. HWP: half waveplate; SL: spherical lens; CM: concave mirror; AL: achromatic lens; SPZT: short-range PZT; LPZT: long-range PZT. (b) Zoom-in view of the different focusing conditions between the two beams and the imaging spectrometer.

nature of the 2DSI measurement, the fringes as shown in Figure 3.12 are available at each point in the beam profile. This will result in a 4D data set (a 2D fringe obtained at each transverse spatial coordinate) from which the wavelength-dependent group-delay can be obtained at each point in the beam.

Figure 4.1 shows the schematics of the current 4DSI setup, which shares the basic configuration with the 2DSI. However, while the pulse under test is focused onto the BBO crystal, the chirped pulses are collimated at the BBO crystal. This way, the chirped pulses can not only be treated as monochromatic waves but also be treated as plane waves. A full 2DSI measurement at a 2D array of points along both transverse axes can be done using an imaging spectrometer. To obtain sufficient spectral resolution, 1600 image frames have to be taken for the spectrum reconstruction. If a continuous phase modulation (as done in 2DSI) is performed,
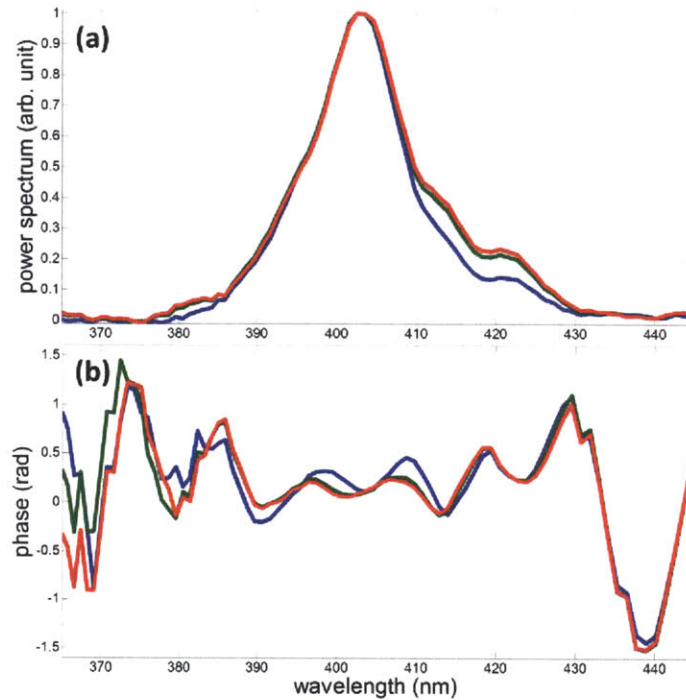
Figure 4.2 Spectra (a) and reconstructed phase (b) measured at three different transverse points of the beam.

the total image frames to be taken will be more than 200,000. Instead, here we implement the Hariharan phase stepping technique **[127]** which only requires 5 discrete phase modulations (with a step size of $\pi/2$) and the total image frames to be taken is reduced to 8,000. Hariharan algorithm is used for its robustness to phase step calibration errors. The phase reconstruction error introduced by the 10-nm repeatability of our PZT is calculated to be less than 1% (20mrad).

Figure 4.2 shows the measured spectra and retrieved phases at three different points in the beam profile. The laser under test is a Kerr-lens mode-locked Ti:sapphire oscillator which has a spectrum spanning from 700nm to 900nm. The first two spectra resemble each other while the third spectrum is different from the others in the long wavelength part. The retrieved phases follow the same trend as

expected since there is a correlation between spectrum and phase in a Kerr-lens mode-locked laser.

With the current setup, we measure the wavelength-dependent group-delay at each transverse spatial coordinate, i.e. $GD(\vec{r}, \omega) = \frac{\partial \phi(\vec{r}, \omega)}{\partial \omega}$. Since $d\phi(\vec{r}, \omega) = \frac{\partial \phi(\vec{r}, \omega)}{\partial \omega} d\omega + \frac{\partial \phi(\vec{r}, \omega)}{\partial \vec{r}} d\vec{r}$, an additional spatial shear interferometer, which measures the wavelength-dependent spatial phase, is necessary to fully enable the complete spatio-temporal characterization of the pulse [128].

4.2   Measurement of the carrier-envelope phase value

The measurement of the CEP value becomes an indispensable pulse characterization tool for determination of an extreme ultrashort pulse, single to sub cycle. A method based on the detection of the asymmetric photoelectron generation by the above-threshold ionization was proposed and demonstrated recently [129]. Alternatively, we propose in this section an all-optical measurement scheme.

f-2f self-referencing nonlinear interferometer is a well-established technique to measure the CEP drift and has been implemented routinely to stabilize the CEP offset frequency (f_{ceo}) of the laser sources. Figure 4.3a is a standard Mach–Zehnder type *f-2f* interferometer. A dichroic beamsplitter first separates the long wavelength part from the short wavelength part of the spectrum. While the long wavelength beam undergoes second-harmonic generation (SHG) in a nonlinear crystal, the short wavelength beam only experiences free-propagation. Then the two beams are overlapped again in both transverse and longitudinal coordinates and interfere linearly on a photodetector. Several different schemes have been proposed and
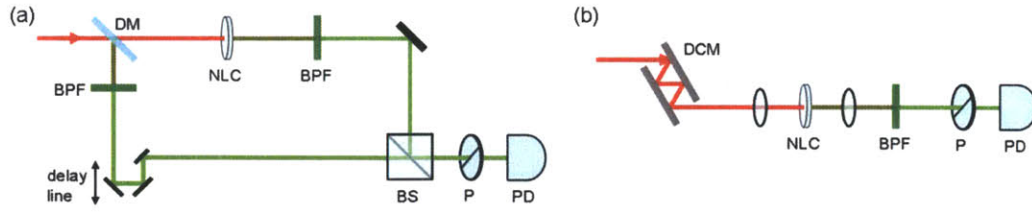
Figure 4.3 (a) Standard Mach-Zehnder type *f-2f* interferometer. (b) Collinear *f-2f* interferometer.

demonstrated, but they all share the same principle as outlined here. For example, collinear geometry (Figure 4.3b) has been developed to eliminate the excess phase error from the interferometer [130]. While this is a perfect way to stabilize the CEP offset frequency (f_{ceo}), a nonlinear crystal itself presents an ultimate obstacle to the measurement of CEP value due to the dispersion in the nonlinear crystal. The dispersion of a 1μm thick β-barium borate (BBO) crystal is enough to introduce a phase shift of more than 150mrad (phase matched, type I SHG of 1200nm) and thus the CEP value cannot be measured accurately.

As mentioned in Chapter 2, the power flow of the three-wave mixing process depends on the relative phase between the three waves given that they are all present at the beginning of the process. In non-dimensional form, the governing equations of the three-wave mixing process are [26]

$$
\begin{cases}
\dfrac{d}{d\zeta}u_1 = -u_2 u_3 \sin\theta \\[2mm]
\dfrac{d}{d\zeta}u_2 = -u_3 u_1 \sin\theta \\[2mm]
\dfrac{d}{d\zeta}u_3 = u_1 u_2 \sin\theta \\[2mm]
\dfrac{d}{d\zeta}\theta = \Delta S + \cot\theta[\ln(u_1 u_2 u_3)]
\end{cases}
\qquad Eq.\,4.1
$$
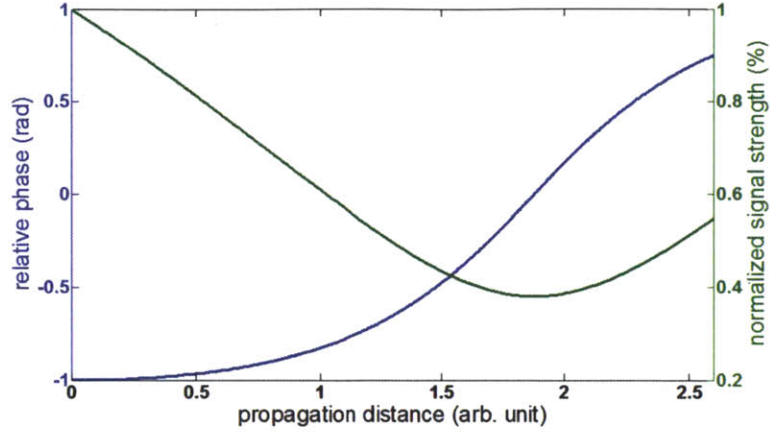
Figure 4.4 Evolution of the relative phase and the signal strength.

, where $u_j = \sqrt{I_j/4\pi\varepsilon_0\omega_j}$, $\theta = \Delta kz - \phi_3 + \phi_2 + \phi_1$, $\Delta S = \Delta kz/\zeta$, and $\zeta = \sqrt{8\pi\omega_1\omega_2\omega_3 d_{eff}^2/c^3 n_1 n_2 n_3}\, z$. Eq. 4.1 can be directly integrated to obtain

$$cos\theta = \frac{C + \Delta S u_3^2/2}{u_1 u_2 u_3} \qquad Eq.\,4.2$$

, where C is a constant of integration depending on the initial condition [26]. For a phase matched three-wave mixing process, as depicted in Figure 4.4, the relative phase remains close to its initial value and only experiences a big change when the process is close to saturation. Thus, the power flow is indicative of the relative phase if we keep the three-wave mixing process well below saturation.

For simplicity, let us consider a type I SHG of an octave-spanning (or more) laser. We numerically solve the governing coupled equations under the slowly evolving wave approximation. We assume the interacting waves have peak intensities of 1GW/cm^2 and the BBO crystal is phase matched for type I SHG of 1200nm light and has a thickness of 100μm. The dispersion of BBO is taken into

144

account by using the IR-corrected Sellmeier equation **[131]**. 40-nm bandpass filters centered at 600nm are assumed to be placed before the photodetectors.

As shown in Figure 4.5a, when the crystal axis is intentionally put at 45-degree off from the laser polarization, all three interaction waves are present at the beginning of the three-wave mixing process. Furthermore, since they are all derived from the same laser, the power flow now depends only on the CEP value and the spectral phase of the laser. The spectral phase can be determined by many optical methods in prior and hence a read of the power change of the SHG signal tells one the CEP value as shown in Figure 4.5b.

Note that this scheme differs fundamentally from standard *f-2f* interferometers because the interference happens during the nonlinear propagation. It is this fundamental difference that takes out the measurement error imposed by the nonlinear crystal. The setup shown in Figure 4.5a can already be used to lock the f_{ceo} and the fact that the third wave exists at the very beginning improves the signal-to-noise ratio and thus better f_{ceo} locking can be achieved compared to that with standard *f-2f* interferometers. To measure the CEP value without ambiguity, we need to perform quadrature detection as shown in Figure 4.6a. The lower arm is identical to the upper arm except that an additional $\pi/4$ CEP is imposed by the fused silica wedge. The argument of $(R_U + iR_L)$ then measures the CEP value without ambiguity, where R_U ($\equiv \frac{PD1}{PD2} - 1$) and R_L ($\equiv \frac{PD3}{PD4} - 1$) are the ratio between the two photodetector signals from the upper arm and the lower arm, respectively. Figure 4.6b shows the simulation result and it shows the CEP value can be unambiguously measured with accuracy better than 100mrad.
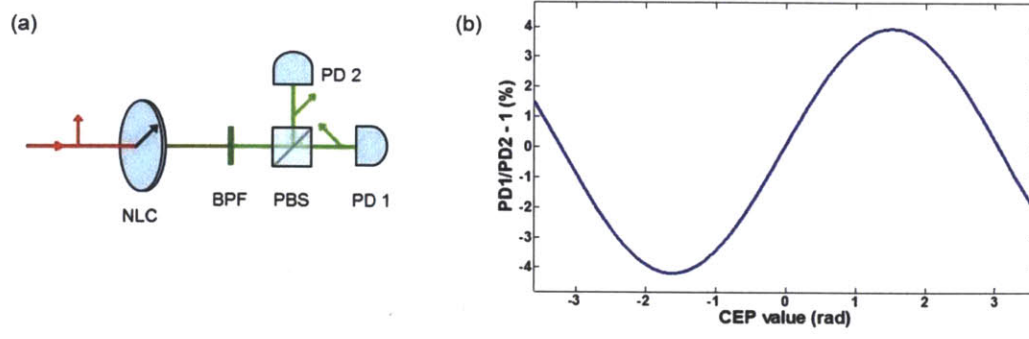
Figure 4.5 (a) The optical setup which can be used to lock the f_{ceo}. PD1 measures the e-polarized wave which carries the CEP information while PD2 measures the laser power. (b) The difference between PD1 and PD2 is almost a sinusoidal function of CEP value.
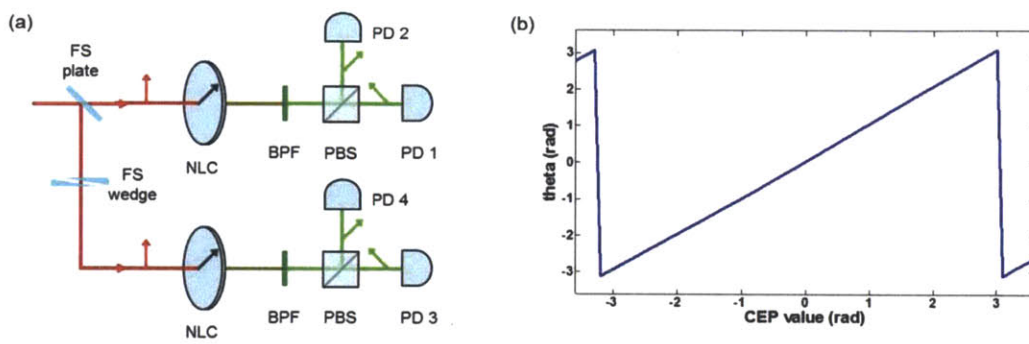
Figure 4.6 (a) The optical setup which measures the CEP value without ambiguity. (b) The argument of (R_U+iR_L) with respect to CEP values, where R_U = $(PD1/PD2) - 1$ and $R_L = (PD3/PD4) - 1$.

References

[1] D. Huang, E. Swanson, C. Lin, J. Schuman, W. Stinson, W. Chang, M. Hee, T. Flotte, K. Gregory, C. Puliafito, and J. G. Fujimoto, "Optical coherence tomography," *Science* **254**, 1178 (1991).

[2] C.-H. Li, A. J. Benedick, P. Fendel, A. G. Glenday, F. X. Kärtner, D. F. Phillips, D. Sasselov, A. Szentgyorgyi, and R. L. Walsworth, "A laser frequency comb that enables radial velocity measurements with a precision of 1 cm s^{-1}," *Nature* **452**, 610 (2008).

[3] C. V. Shank, "Investigation of ultrafast phenomena in the femtosecond time domain," *Science* **233**, 1276 (1986).

[4] A. H. Zewail, "Laser femtochemistry," *Science* **242**, 1645 (1988).

[5] V. Sundström, "Femtobiology," *Annu. Rev. Phys. Chem.* **59**, 53 (2008).

[6] D. J. Jones, S. A. Diddams, J. K. Ranka, A. Stentz, R. S. Windeler, J. L. Hall, and S. T. Cundiff, "Carrier-envelope phase control of femtosecond mode-locked lasers and direct optical frequency synthesis," *Science* **288**, 635 (2000).

[7] R. Holzwarth, T. Udem, T. W. Hänsch, J. C. Knight, W. J. Wadsworth, and P. S. J. Russell, "Optical frequency synthesizer for precision spectroscopy," *Phys. Rev. Lett.* **85**, 2264 (2000).

[8] E. Esarey, C. B. Schroeder, and W. P. Leemans, "Physics of laser-driven plasma-based electron accelerators," *Rev. Mod. Phys.* **81**, 1229 (2009).

[9] D. Strickland and G. Mourou, "Compression of amplified chirped optical pulses," *Opt. Commun.* **56**, 219 (1985).

[10] P. B. Corkum, "Plasma perspective on strong field multiphoton ionization," *Phys. Rev. Lett.* **71**, 1994 (1993).

[11] L. V. Keldysh, "Ionization in the field of a strong electromagnetic wave," *Soviet Physics - JETP* **20**, 1307 (1965).

[12] E. Goulielmakis, M. Schultze, M. Hofstetter, V. S. Yakovlev, J. Gagnon, M. Uiberacker, A. L. Aquila, E. M. Gullikson, D. T. Attwood, R. Kienberger, F. Krausz, and U. Kleineberg, "Single-cycle nonlinear optics," *Science* **320**, 1614 (2008).

[13] F. Krausz and M. Ivanov, "Attosecond physics," *Rev. Mod. Phys.* **81**, 163 (2009).

[14] M. Schultze, M. Fieß, N. Karpowicz, J. Gagnon, M. Korbman, M. Hofstetter, S. Neppl, A. L. Cavalieri, Y. Komninos, T. Mercouris, C. A. Nicolaides, R. Pazourek, S. Nagele, J. Feist, J. Burgdörfer, A. M. Azzeer, R. Ernstorfer, R. Kienberger, U. Kleineberg, E. Goulielmakis, F. Krausz, and V. S. Yakovlev, "Delay in photoemission," *Science* **328**, 1658 (2010).

[15] L. E. Chipperfield, J. S. Robinson, J. W. G. Tisch, and J. P. Marangos, "Ideal waveform to generate the maximum possible electron recollision energy for any given oscillation period," *Phys. Rev. Lett.* **102**, 063003 (2009).

[16] D. E. Spence, P. N. Kean, and W. Sibbett, "60-fsec pulse generation from a self-mode-locked Ti:sapphire laser," *Opt. Lett.* **16**, 42 (1991).

[17] M. Piché and F. Salin, "Self-mode locking of solid-state lasers without apertures," *Opt. Lett.* **18**, 1041 (1993).

[18] F. X. Kärtner, N. Matuschek, T. Schibli, U. Keller, H. A. Haus, C. Heine, R. Morf, V. Scheuer, M. Tilsch, and T. Tschudi, "Design and fabrication of double-chirped mirrors," *Opt. Lett.* **22**, 831 (1997).

[19] M. Pessot, P. Maine, and G. Mourou, "1000 times expansion/compression of optical pulses for chirped pulse amplification," *Opt. Commun.* **62**, 419 (1987).

[20] M. Lewenstein, P. Balcou, M. Y. Ivanov, A. L'Huillier, and P. B. Corkum, "Theory of high-harmonic generation by low-frequency laser fields," *Phys. Rev. A* **49**, 2117 (1994).

[21] P. B. Corkum and F. Krausz, "Attosecond science," *Nat. Phys.* **3**, 381 (2007).

[22] J. Moses, C. Manzoni, S.-W. Huang, G. Cerullo, and F. X. Kärtner, "Temporal optimization ofultrabroadband high-energy OPCPA," *Opt. Express* **17**, 5540 (2009).

[23] S.-W. Huang, G. Cirmi, J. Moses, K.-H. Hong, S. Bhardwaj, J. R. Birge, L.-J. Chen, E. Li, B. J. Eggleton, G. Cerullo, and F. X. Kärtner, "High-energy pulse synthesis with sub-cycle waveform control for strong-field physics," *Nat. Photon.* **5**, 475 (2011).

[24] S.-W. Huang, G. Cirmi, J. Moses, K.-H. Hong, S. Bhardwaj, J. R. Birge, L.-J. Chen, I. V. Kabakova, E. Li, B. J. Eggleton, G. Cerullo, and F. X. Kärtner, "Optical waveform synthesizer and its application to high-harmonic generation," *J. Phys. B* **45**, 074009 (2012).

[25] K.-H. Hong, S.-W. Huang, J. Moses, X. Fu, C.-J. Lai, G. Cirmi, A. Sell, E. Granados, P. Keathley, and F. X. Kärtner, "High-energy, phase-stable, ultrabroadband kHz OPCPA at 2.1 μm pumped by a picosecond cryogenic Yb:YAG laser," *Opt. Express* **19**, 15538 (2011).

[26] J. Moses and S.-W. Huang, "Conformal profile theory for performance scaling of ultrabroadband optical parametric chirped pulse amplification," *J. Opt. Soc. Am. B* **28**, 812 (2011).

[27] R. W. Boyd, *Nonlinear Optics*, 2nd ed. Boston: Academic Press, 2003.

[28] G. Cerullo and S. De Silvestri, "Ultrafast optical parametric amplifiers," *Rev. Sci. Instrum.* **74**, 1 (2003).

[29] I. N. Ross, P. Matousek, G. H. C. New, and K. Osvay, "Analysis and optimization of optical parametric chirped pulse amplification," *J. Opt. Soc. Am. B* **19**, 2945 (2002).

[30] J. A. Armstrong, N. Bloembergen, J. Ducuing, and P. S. Pershan, "Interactions between Light Waves in a Nonlinear Dielectric," *Phys. Rev.* **127**, 1918 (1962).

[31] A. Dubietis, R. Butkus, and A. P. Piskarskas, "Trends in chirped pulse optical parametric amplification," *IEEE J. Sel. Topics Quantum Electron.* **12**, 163 (2006).

[32] I. A. Begishev, A. A. Gulamov, E. A. Erofeev, é A. Ibragimov, S. R. Kamalov, T. Usmanov, and A. D. Khadzhaev, "Highly efficient parametric amplification of optical beams. I. Optimization of the profiles of interacting waves in parametric amplification," *Soviet J. Quantum Electron.* **20**, 1100 (1990).

[33] I. A. Begishev, A. A. Gulamov, E. A. Erofeev, é A. Ibragimov, S. R. Kamalov, T. Usmanov, and A. D. Khadzhaev, "Highly efficient parametric amplification of optical beams. II. Parametric interaction of waves with conformal profiles," *Soviet J. Quantum Electron.* **20**, 1104 (1990).

[34] M. Guardalben, J. Keegan, L. Waxer, V. Bagnoud, I. Begishev, J. Puth, and J. Zuegel, "Design of a highly stable, high-conversion-efficiency, optical parametric chirped-pulse amplification system with good beam quality," *Opt. Express* **11**, 2511 (2003).

[35] J. A. Fülöp, Z. Major, B. Horváth, F. Tavella, A. Baltuška, and F. Krausz, "Shaping of picosecond pulses for pumping optical parametric amplification," *Appl. Phys. B* **87**, 79 (2007).

[36] L. J. Waxer, V. Bagnoud, I. A. Begishev, M. J. Guardalben, J. Puth, and J. D. Zuegel, "High-conversion-efficiency optical parametric chirped-pulse amplification system using spatiotemporally shaped pump pulses," *Opt. Lett.* **28**, 1245 (2003).

[37] V. Bagnoud, I. A. Begishev, M. J. Guardalben, J. Puth, and J. D. Zuegel, "5 Hz, >250 mJ optical parametric chirped-pulse amplifier at 1053 nm," *Opt. Lett.* **30**, 1843 (2005).

[38] J. Moses, S.-W. Huang, K.-H. Hong, O. D. Mücke, E. L. Falcão-Filho, A. Benedick, F. Ö. Ilday, A. Dergachev, J. A. Bolger, B. J. Eggleton, and F. X. Kärtner, "Highly stable ultrabroadband mid-IR optical parametric chirped-pulse amplifier optimized for superfluorescence suppression," *Opt. Lett.*, **34**, 1639 (2009).

[39] E. Sidick, A. Knoesen, and A. Dienes, "Ultrashort-pulse second-harmonic generation. I. Transform-limited fundamental pulses," *J. Opt. Soc. Am. B* **12**, 1704 (1995).

[40] E. Sidick, A. Dienes, and A. Knoesen, "Ultrashort-pulse second-harmonic generation. II. Non-transform-limited fundamental pulses," *J. Opt. Soc. Am. B* **12**, 1713 (1995).

[41] G. Cirmi, C. Manzoni, D. Brida, S. De Silvestri, and G. Cerullo, "Carrier-envelope phase stable, few-optical-cycle pulses tunable from visible to near IR," *J. Opt. Soc. Am. B* **25**, B62 (2008).

[42] S. A. Akhmanov, V. A. Vysloukh, and A. S. Chirkin, *Optics of femtosecond laser pulses*. New York: American Institute of Physics, 1992.

[43] G. P. Agrawal, *Nonlinear Fiber Optics*, 3rd ed. Boston: Academic Press, 2001.

[44] H. A. Haus, *Electromagnetic Noise and Quantum Optical Measurements*. Berlin: Springer-Verlag, 2000.

[45] J. Moses, O. D. Mücke, S.-W. Huang, A. Benedick, E. L. Falcão-Filho, K.-H. Hong, A. M. Siddiqui, J. R. Birge, F. Ö. Ilday, and F. X. Kärtner, "Optimized 2-micron Optical Parametric Chirped Pulse Amplifier for High Harmonic Generation," presented at the XVI International Conference on Ultrafast Phenomena, Stresa, Italy, 2008.

[46] L. Matos, D. Kleppner, O. Kuzucu, T. R. Schibli, J. Kim, E. P. Ippen, and F. X. Kärtner, "Direct frequency comb generation from an octave-spanning, prismlessTi:sapphire laser," *Opt. Lett.* **29**, 1683 (2004).

[47] T. Miura, K. Kobayashi, K. Takasago, Z. Zhang, K. Torizuka, and F. Kannari, "Timing jitter in a kilohertz regenerative amplifier of a femtosecond-pulse Ti:Al2O3 laser," *Opt. Lett.* **25**, 1795 (2000).

[48] C. Manzoni, J. Moses, F. X. Kärtner, and G. Cerullo, "Excess quantum noise in optical parametric chirped-pulse amplification," *Opt. Express* **19**, 8357 (2011).

[49] Z. Chang, "Carrier-envelope phase shift caused by grating-based stretchers and compressors," *Appl. Opt.* **45**, 8350 (2006).

[50] T. Metzger, A. Schwarz, C. Y. Teisset, D. Sutter, A. Killi, R. Kienberger, and F. Krausz, "High-repetition-rate picosecond pump laser based on a Yb:YAG disk amplifier for optical parametric amplification," *Opt. Lett.* **34**, 2123 (2009).

[51] R. L. Aggarwal, D. J. Ripin, J. R. Ochoa, and T. Y. Fan, "Measurement of thermo-optic properties of Y3Al5O12, Lu3Al5O12, YAlO3, LiYF4, LiLuF4,

BaY2F8, KGd(WO4)2, and KY(WO4)2 laser crystals in the 80–300 K temperature range," *J. Appl. Phys.* **98**, 103514 (2005).

[52] T. Y. Fan, D. J. Ripin, R. L. Aggarwal, J. R. Ochoa, B. Chann, M. Tilleman, and J. Spitzberg, "Cryogenic Yb^{3+}-Doped Solid-State Lasers," *IEEE J. Sel. Topics Quantum Electron.* **13**, 448 (2007).

[53] M. Ostermeyer and A. Straesser, "Theoretical investigation of feasibility of Yb:YAG as laser material for nanosecond pulse emission with large energies in the Joule range," *Opt. Commun.* **274**, 422 (2007).

[54] C. Rouyer, É. Mazataud, I. Allais, A. Pierre, S. Seznec, C. Sauteret, G. Mourou, and A. Migus, "Generation of 50-TW femtosecond pulses in a Ti:sapphire/Nd:glass chain," *Opt. Lett.* **18**, 214 (1993).

[55] [Online]. Available: http://www.ondax.com/.

[56] X. Gu, G. Marcus, Y. Deng, T. Metzger, C. Teisset, N. Ishii, T. Fuji, A. Baltuska, R. Butkus, V. Pervak, H. Ishizuki, T. Taira, T. Kobayashi, R. Kienberger, and F. Krausz, "Generation of carrier-envelope-phase-stable 2-cycle 740-µJ pulses at 2.1-µm carrier wavelength," *Opt. Express* **17**, 62 (2009).

[57] M.-C. Chen, P. Arpin, T. Popmintchev, M. Gerrity, B. Zhang, M. Seaberg, D. Popmintchev, M. M. Murnane, and H. C. Kapteyn, "Bright, Coherent, Ultrafast Soft X-Ray Harmonics Spanning the Water Window from a Tabletop Light Source," *Phys. Rev. Lett.* **105**, 173901 (2010).

[58] E. L. Falcão-Filho, C.-J. Lai, K.-H. Hong, V.-M. Gkortsas, S.-W. Huang, L.-J. Chen, and F. X. Kärtner, "Scaling of high-order harmonic efficiencies with visible wavelength drivers: A route to efficient extreme ultraviolet sources," *Appl. Phys. Lett.* **97**, 061107 (2010).

[59] T. Popmintchev, M.-C. Chen, A. Bahabad, M. Gerrity, P. Sidorenko, O. Cohen, I. P. Christov, M. M. Murnane, and H. C. Kapteyn, "Phase matching of high harmonic generation in the soft and hard X-ray regions of the spectrum," *Proc. Natl. Acad. Sci. USA* **106**, 10516 (2009).

[60] M.-C. Chen, P. Arpin, T. Popmintchev, M. Gerrity, B. Zhang, M. Seaberg, D. Popmintchev, M. M. Murnane, and H. C. Kapteyn, "Bright, Coherent, Ultrafast Soft X-Ray Harmonics Spanning the Water Window from a Tabletop Light Source," *Phys. Rev. Lett.* **105**, 173901 (2010).

[61] D. Brida, G. Cirmi, C. Manzoni, S. Bonora, P. Villoresi, S. De Silvestri, and G. Cerullo, "Sub-two-cycle light pulses at 1.6 ?m from an optical parametric amplifier," *Opt. Lett.* **33**, 741 (2008).

[62] K. Kato, "Second-harmonic generation to 2048Å in β-BaB$_2$O$_4$," *IEEE J. Quantum Electron.* **22**, 1013 (1986).

[63] O. V. Chekhlov, J. L. Collier, I. N. Ross, P. K. Bates, M. Notley, C. Hernandez-Gomez, W. Shaikh, C. N. Danson, D. Neely, P. Matousek, S. Hancock, and L. Cardoso, "35 J broadband femtosecond optical parametric chirped pulse amplification system," *Opt. Lett.* **31**, 3665 (2006).

[64] S. Zhou, D. Ouzounov, H. Li, I. Bazarov, B. Dunham, C. Sinclair, and F. W. Wise, "Efficient temporal shaping of ultrashort pulses with birefringent crystals," *Appl. Opt.* **46**, 8488 (2007).

[65] I. Will and G. Klemz, "Generation of flat-top picosecond pulses by coherent pulse stackingin a multicrystal birefringent filter," *Opt. Express* **16**, 14922 (2008).

[66] A. Gaydardzhiev, I. Nikolov, I. Buchvarov, V. Petrov, and F. Noack, "Ultrabroadband operation of a femtosecondoptical parametric generator based on BiB3O6 inthe near-IR," *Opt. Express* **16**, 2363 (2008).

[67] M. Nisoli, S. De Silvestri, and O. Svelto, "Generation of high energy 10 fs pulses by a new pulse compression technique," *Appl. Phys. Lett.* **68**, 2793 (1996).

[68] X. Chen, A. Jullien, A. Malvache, L. Canova, A. Borot, A. Trisorio, C. G. Durfee, and R. Lopez-Martens, "Generation of 4.3 fs, 1 mJ laser pulses via compression of circularly polarized pulses in a gas-filled hollow-core fiber," *Opt. Lett.* **34**, 1588 (2009).

[69] J. Park, J. Lee, and C. H. Nam, "Generation of 1.5 cycle 0.3 TW laser pulses using a hollow-fiber pulse compressor," *Opt. Lett.* **34**, 2342 (2009).

[70] S. Bohman, A. Suda, T. Kanai, S. Yamaguchi, and K. Midorikawa, "Generation of 5.0 fs, 5.0 mJ pulses at 1-kHz using hollow-fiber pulse compression," *Opt. Lett.* **35**, 1887 (2010).

[71] S. E. Harris and A. V. Sokolov, "Subfemtosecond Pulse Generation by Molecular Modulation," *Phys. Rev. Lett.* **81**, 2894 (1998).

[72] M. Y. Shverdin, D. R. Walker, D. D. Yavuz, G. Y. Yin, and S. E. Harris, "Generation of a Single-Cycle Optical Pulse," *Phys. Rev. Lett.* **94**, 033904 (2005).

[73] S. W. Huang, W.-J. Chen, and A. H. Kung, "Vibrational molecular modulation in hydrogen," *Phys. Rev. A* **74**, 063825 (2006).

[74] W.-J. Chen, Z.-M. Hsieh, S. W. Huang, H.-Y. Su, C.-J. Lai, T.-T. Tang, C.-H. Lin, C.-K. Lee, R.-P. Pan, C.-L. Pan, and A. H. Kung, "Sub-Single-Cycle

Optical Pulse Train with Constant Carrier Envelope Phase," *Phys. Rev. Lett.* **100**, 163906 (2008).

[75] H.-S. Chan, Z.-M. Hsieh, W.-H. Liang, A. H. Kung, C.-K. Lee, C.-J. Lai, R.-P. Pan, and L.-H. Peng, "Synthesis and Measurement of Ultrafast Waveforms from Five Discrete Optical Harmonics," *Science* **331**, 1165 (2011).

[76] A. Wirth, M. T. Hassan, I. Grguraš, J. Gagnon, A. Moulet, T. T. Luu, S. Pabst, R. Santra, Z. A. Alahmed, A. M. Azzeer, V. S. Yakovlev, V. Pervak, F. Krausz, and E. Goulielmakis, "Synthesized Light Transients," *Science* **334**, 195 (2011).

[77] Z. Wei, Y. Kobayashi, Z. Zhang, and K. Torizuka, "Generation of two-color femtosecond pulses by self-synchronizing Ti:sapphire and Cr:forsterite lasers," *Opt. Lett.* **26**, 1806 (2001).

[78] R. K. Shelton, L.-S. Ma, H. C. Kapteyn, M. M. Murnane, J. L. Hall, and J. Ye, "Phase-Coherent Optical Pulse Synthesis from Separate Femtosecond Lasers," *Science* **293**, 1286 (2001).

[79] G. Krauss, S. Lohss, T. Hanke, A. Sell, S. Eggert, R. Huber, and A. Leitenstorfer, "Synthesis of a single cycle of light with compact erbium-doped fibre technology," *Nat. Photon.* 4, 33 (2010).

[80] S. Haessler, T. Balčiūnas, P. Salieres, and A. Baltuška, "Challenges in self-probing of molecules, to be met by a waveform synthesizer," presented at the The 3rd International Conference on Attosecond Physics, Sapporo, Japan, 2011, p. E–2.

[81] T. R. Schibli, J. Kim, O. Kuzucu, J. T. Gopinath, S. N. Tandon, G. S. Petrich, L. A. Kolodziejski, J. G. Fujimoto, E. P. Ippen, and F. X. Kärtner, "Attosecond active synchronization of passively mode-locked lasers by balanced cross correlation," *Opt. Lett.* **28**, 947 (2003).

[82] A. Baltuška, T. Fuji, and T. Kobayashi, "Controlling the Carrier-Envelope Phase of Ultrashort Light Pulses with Optical Parametric Amplifiers," *Phys. Rev. Lett.* **88**, 133901 (2002).

[83] S. Adachi, N. Ishii, Y. Kobayashi, Y. Nomura, J. Itatani, T. Kanai, and S. Watanabe, "Carrier-Envelope Phase Control of Few-Cycle Parametric Chirped-Pulse Amplifier," *Jpn. J. Appl. Phys.* **49**, 032703 (2010).

[84] Q. Zou and B. Lü, "Propagation properties of ultrashort pulsed beams with constant waist width in free space," *Opt. Laser Technol.* **39**, 619 (2007).

[85] J. R. Birge, H. M. Crespo, and F. X. Kärtner, "Theory and design of two-dimensional spectral shearing interferometry for few-cycle pulse measurement," *J. Opt. Soc. Am. B* **27**, 1165 (2010).

[86] C. Iaconis and I. A. Walmsley, "Self-referencing spectral interferometry for measuring ultrashort optical pulses," *IEEE J. Quantum Electron.* **35**, 501 (1999).

[87] O. D. Mücke, D. Sidorov, P. Dombi, A. Pugžlys, A. Baltuška, S. Ališauskas, V. Smilgevičius, J. Pocius, L. Giniūnas, R. Danielius, and N. Forget, "Scalable Yb-MOPA-driven carrier-envelope phase-stable few-cycle parametric amplifier at 1.5 μm," *Opt. Lett.* **34**, 118 (2009).

[88] A. M. Siddiqui, G. Cirmi, D. Brida, F. X. Kärtner, and G. Cerullo, "Generation of <7 fs pulses at 800 nm from a blue-pumped optical parametric amplifier at degeneracy," *Opt. Lett.* **34**, 3592 (2009).

[89] R. A. Kaindl, M. Wurm, K. Reimann, P. Hamm, A. M. Weiner, and M. Woerner, "Generation, shaping, and characterization of intense femtosecond pulses tunable from 3 to 20 μm," *J. Opt. Soc. Am. B* **17**, 2086 (2000).

[90] M. Zavelani-Rossi, G. Cerullo, S. De Silvestri, L. Gallmann, N. Matuschek, G. Steinmeyer, U. Keller, G. Angelow, V. Scheuer, and T. Tschudi, "Pulse compression over a 170-THz bandwidth in the visible by use of only chirped mirrors," *Opt. Lett.* **26**, 1155 (2001).

[91] T. R. Schibli, O. Kuzucu, J.-W. Kim, E. P. Ippen, J. G. Fujimoto, F. X. Kärtner, V. Scheuer, and G. Angelow, "Toward single-cycle laser systems," *IEEE J. Sel. Topics Quantum Electro.* **9**, 990 (2003).

[92] Z. Chang, B. Shan, and S. Ghimire, "Generation of the attosecond extreme ultraviolet supercontinuum by a polarization gating," *J. Mod. Opt.* **52**, 277 (2005).

[93] G. Sansone, E. Benedetti, F. Calegari, C. Vozzi, L. Avaldi, R. Flammini, L. Poletto, P. Villoresi, C. Altucci, R. Velotta, S. Stagira, S. De Silvestri, and M. Nisoli, "Isolated Single-Cycle Attosecond Pulses," *Science* **314**, 443 (2006).

[94] I. J. Kim, C. M. Kim, H. T. Kim, G. H. Lee, Y. S. Lee, J. Y. Park, D. J. Cho, and C. H. Nam, "Highly Efficient High-Harmonic Generation in an Orthogonally Polarized Two-Color Laser Field," *Phys. Rev. Lett.* **94**, 243901 (2005).

[95] Y. Oishi, M. Kaku, A. Suda, F. Kannari, and K. Midorikawa, "Generation of extreme ultraviolet continuum radiation driven by a sub-10-fs two-color field," *Opt. Express* **14**, 7230 (2006).

[96] M. J. Abel, T. Pfeifer, P. M. Nagel, W. Boutu, M. J. Bell, C. P. Steiner, D. M. Neumark, and S. R. Leone, "Isolated attosecond pulses from ionization gating of high-harmonic emission," *Chem. Phys.* **366**, 9 (2009).

[97] H. Mashiko, S. Gilbertson, C. Li, S. D. Khan, M. M. Shakya, E. Moon, and Z. Chang, "Double Optical Gating of High-Order Harmonic Generation with Carrier-Envelope Phase Stabilized Lasers," *Phys. Rev. Lett.* **100**, 103906 (2008).

[98] F. Ferrari, F. Calegari, M. Lucchini, C. Vozzi, S. Stagira, G. Sansone, and M. Nisoli, "High-energy isolated attosecond pulses generated by above-saturation few-cycle fields," *Nat. Photon.* **4**, 875 (2010).

[99] N. Dudovich, O. Smirnova, J. Levesque, Y. Mairesse, M. Y. Ivanov, D. M. Villeneuve, and P. B. Corkum, "Measuring and controlling the birth of attosecond XUV pulses," *Nat. Phys.* **2**, 781 (2006).

[100] B. Henke, "X-Ray Interactions: Photoabsorption, Scattering, Transmission, and Reflection at E = 50-30,000 eV, Z = 1-92," *Atomic Data and Nuclear Data Tables* **54**, 181 (1993).

[101] A. Gordon, C. Jirauschek, and F. X. Kärtner, "Numerical solver of the time-dependent Schrödinger equation with Coulomb singularities," *Phys. Rev. A* **73**, 042505 (2006).

[102] X. M. Tong and C. D. Lin, "Empirical formula for static field ionization rates of atoms and molecules by lasers in the barrier-suppression regime," *J. Phys. B* **38**, 2593 (2005).

[103] F. Tavella, Y. Nomura, L. Veisz, V. Pervak, A. Marcinkevičius, and F. Krausz, "Dispersion management for a sub-10-fs, 10 TW optical parametric chirped-pulse amplifier," *Opt. Lett.* **32**, 2227 (2007).

[104] I. A. Walmsley and C. Dorrer, "Characterization of ultrashort electromagnetic pulses," *Advances in Optics and Photonics* **1**, 308 (2009).

[105] J. Birge, "Methods for Engineering Sub-Two-Cycle Mode-Locked Lasers," *PhD thesis* (2010).

[106] J. N. Sweetser, D. N. Fittinghoff, and R. Trebino, "Transient-grating frequency-resolved optical gating," *Opt. Lett.* **22**, 519 (1997).

[107] S. Woutersen, U. Emmerichs, and H. J. Bakker, "Femtosecond Mid-IR Pump-Probe Spectroscopy of Liquid Water: Evidence for a Two-Component Structure," *Science* **278**, 658 (1997).

[108] M. Bonn, C. Hess, S. Funk, J. H. Miners, B. N. J. Persson, M. Wolf, and G. Ertl, "Femtosecond Surface Vibrational Spectroscopy of CO Adsorbed on Ru(001) during Desorption," *Phys. Rev. Lett.* **84**, 4653 (2000).

[109] C. I. Blaga, F. Catoire, P. Colosimo, G. G. Paulus, H. G. Muller, P. Agostini, and L. F. DiMauro, "Strong-field photoionization revisited," *Nat. Phys.* **5**, 335 (2009).

[110] A. D. Shiner, B. E. Schmidt, C. Trallero-Herrero, H. J. Wörner, S. Patchkovskii, P. B. Corkum, J.-C. Kieffer, F. Légaré, and D. M. Villeneuve, "Probing collective multi-electron dynamics in xenon with high-harmonic spectroscopy," *Nat. Phys.* **7**, 464 (2011).

[111] K.-H. Hong, S.-W. Huang, J. Moses, X. Fu, C.-J. Lai, G. Cirmi, A. Sell, E. Granados, P. Keathley, and F. X. Kärtner, "High-energy, phase-stable, ultrabroadband kHz OPCPA at 2.1 μm pumped by a picosecond cryogenic Yb:YAG laser," *Opt. Express* **19**, 15538 (2011).

[112] D. Brida, C. Manzoni, G. Cirmi, M. Marangoni, S. De Silvestri, and G. Cerullo, "Generation of broadband mid-infrared pulsesfrom an optical parametric amplifier," *Opt. Express* **15**, 15035 (2007).

[113] C. Heese, C. R. Phillips, L. Gallmann, M. M. Fejer, and U. Keller, "Ultrabroadband, highly flexible amplifier for ultrashort midinfrared laser pulses based on aperiodically poled Mg:LiNbO3," *Opt. Lett.* **35**, 2340 (2010).

[114] O. Chalus, A. Thai, P. K. Bates, and J. Biegert, "Six-cycle mid-infrared source with 3.8 μJ at 100 kHz," *Opt. Lett.* **35**, 3204 (2010).

[115] G. Cerullo and S. De Silvestri, "Ultrafast optical parametric amplifiers," *Rev. Sci. Instrum.* **74**, 1 (2003).

[116] K. Okamura and T. Kobayashi, "Octave-spanning carrier-envelope phase stabilized visible pulse with sub-3-fs pulse duration," *Opt. Lett.* **36**, 226 (2011).

[117] O. Isaienko and E. Borguet, "Pulse-front matching of ultrabroadband near-infrared noncollinear optical parametric amplified pulses," *J. Opt. Soc. Am. B* **26**, 965 (2009).

[118] J. Moses, S.-W. Huang, K.-H. Hong, O. D. Mücke, E. L. Falcão-Filho, A. Benedick, F. Ö. Ilday, A. Dergachev, J. A. Bolger, B. J. Eggleton, and F. X. Kärtner, "Highly stable ultrabroadband mid-IR optical parametric chirped-pulse amplifier optimized for superfluorescence suppression," *Opt. Lett.* **34**, 1639 (2009).

[119] G. Arisholm, J. Biegert, P. Schlup, C. Hauri, and U. Keller, "Ultra-broadband chirped-pulse optical parametric amplifier with angularly dispersed beams," *Opt. Express* **12**, 518 (2004).

[120] K. Yamane, T. Tanigawa, T. Sekikawa, and M. Yamashita, "Angularly-dispersed optical parametric amplification of optical pulses with one-octave bandwidth toward monocycle regime," *Opt. Express* **16**, 18345 (2008).

[121] T. Fuji, N. Ishii, C. Y. Teisset, X. Gu, T. Metzger, A. Baltuska, N. Forget, D. Kaplan, A. Galvanauskas, and F. Krausz, "Parametric amplification of few-cycle carrier-envelope phase-stable pulses at 2.1 μm," *Opt. Lett.* **31**, 1103 (2006).

[122] J. Moses, H. Suchowski, and F. X. Kärtner, "Fully efficient adiabatic downconversion of broadband Ti:sapphire oscillator pulses," *Opt. Lett.* **37**, 1589 (2012).

[123] C. Manzoni, J. Moses, F. X. Kärtner, and G. Cerullo, "Excess quantum noise in optical parametric chirped-pulse amplification," *Opt. Express* **19**, 8357 (2011).

[124] I. N. Ross, P. Matousek, G. H. C. New, and K. Osvay, "Analysis and optimization of optical parametric chirped pulse amplification," *J. Opt. Soc. Am. B* **19**, 2945 (2002).

[125] J. Moses and S.-W. Huang, "Conformal profile theory for performance scaling of ultrabroadband optical parametric chirped pulse amplification," *J. Opt. Soc. Am. B* **28**, 812 (2011).

[126] T. Schreiber, J. Limpert, H. Zellmer, A. Tünnermann, and K. P. Hansen, "High average power supercontinuum generation in photonic crystal fibers," *Opt. Commun.* **228**, 71 (2003).

[127] D. Malacara, *Optical Shop Testing*. John Wiley & Sons, 2007.

[128] C. Dorrer, E. M. Kosik, and I. A. Walmsley, "Spatio-temporal characterization of the electric field of ultrashort optical pulses using two-dimensional shearing interferometry," *Appl. Phys. B* **74**, s209 (2002).

[129] T. Wittmann, B. Horvath, W. Helml, M. G. Schatzel, X. Gu, A. L. Cavalieri, G. G. Paulus, and R. Kienberger, "Single-shot carrier-envelope phase measurement of few-cycle laser pulses," *Nat. Phys.* **5**, 357 (2009).

[130] O. Mücke, R. Ell, A. Winter, J.-W. Kim, J. Birge, L. Matos, and F. Kärtner, "Self-Referenced 200 MHz Octave-Spanning Ti:Sapphire Laser with 50 Attosecond Carrier-Envelope Phase Jitter," *Opt. Express* **13**, 5163 (2005).

[131] D. Zhang, Y. Kong, and J. Zhang, "Optical parametric properties of 532-nm-pumped beta-barium-borate near the infrared absorption edge," *Opt. Commun.* **184**, 485 (2000).

157

THIS PAGE IS INTENTIONALLY LEFT BLANK

Appendix

Assume the signal and noise fluctuations are not correlated (<u>not true if noise is significant</u>)

$$\text{Energy fluctuation}: \quad M_1 = \frac{\sigma_E}{\mu} = \frac{\sqrt{\sigma_S^2 + \sigma_N^2}}{\mu} = 1.5\%$$

$$\text{Intensity fluctuation}: \quad M_2 = \frac{\sigma_I}{\mu_S} = \frac{\sigma_S}{\mu_S} = 0.8\%$$

Assume the duration and the beam size is not changed too much during the measurement, fluctuation in intensity can be transformed to fluctuation in signal energy.

$$M_1^2 = \left(\frac{\sigma_N}{\mu}\right)^2 + M_2^2 \left(\frac{\mu_S}{\mu}\right)^2$$

$$M_1^2 - M_2^2 = \left(\frac{\sigma_N}{\mu}\right)^2 + M_2^2 \left[\left(\frac{\mu_S}{\mu}\right)^2 - 1\right]$$

Noise (super-fluorescence) has a distribution such that $\sigma_N \approx 0.15\mu_N$ (measured with an OMA).

$$M_1^2 - M_2^2 = \left(\frac{\sigma_N}{\mu}\right)^2 + M_2^2 \left[\left(\frac{\mu_S}{\mu}\right)^2 - 1\right] = \left(0.15\frac{\mu_N}{\mu}\right)^2 + M_2^2 \left[\left(\frac{\mu_S}{\mu}\right)^2 - 1\right]$$

$$\Rightarrow 1.61E^{-4} = 0.0225\left(\frac{\mu_N}{\mu}\right)^2 + 6.4E^{-5}\left[\left(\frac{\mu_N}{\mu}\right)^2 - 2\frac{\mu_N}{\mu}\right]$$

$$\Rightarrow \frac{\mu_N}{\mu} \approx 8\%$$